Aus dem Bereich Medizinische Physiologie
Theoretische Medizin und Biowissenschaften der Medizinischen Fakultät
der Universität des Saarlandes, Homburg/Saar

The journey of murine CD8-positive T lymphocytes-derived exosomes from the cells via the organelles to the target

Dissertation Zur Erlangung des Grades eines Doktors der Naturwissenschaften der Medizinischen Fakultät

der UNIVERSITÄT DES SAARLANDES

2024

vorgelegt von: Nadia Alawar

geb in Bzbdine, Libanon

Tag der Promotion: 25.08.2025

Dekan: Univ.-Prof. Dr. med. dent. M. Hannig

Berichterstatter: PD Dr. Ute Becherer
 Berichterstatter: Prof. Dr. Veit Flockerzi
 Berichterstatter: Prof. Dr. Eva-Maria Albers

Eidesstattliche Erklärung

Erklärung gemäß § 7 Abs. 1 Nr. 2

Ich erkläre hiermit an Eides statt, dass ich die vorliegende Arbeit ohne unzulässige Hilfe Dritter und ohne Benutzung anderer als der angegebenen Hilfsmittel angefertigt habe. Die aus anderen Quellen direkt oder indirekt übernommenen Daten und Konzepte sind unter Angabe der Quelle gekennzeichnet.

Bei der Auswahl und Auswertung folgenden Materials haben mir die nachstehend aufgeführten Personen in der jeweils beschriebenen Weise unentgeltlich geholfen:

- 1. Die Klonierung der pMAX-CD81-SEP und pMAX-CD63 pHuji erfolgte durch Margarete Klose.
- 2. Die elektronenmikroskopische Bildgebung wurde von Dr. Claudia Schirra durchgeführt.
- 3. Die Massenspektrometrie-Experimente wurden von Dr. Claudia Fecher-Trost im Labor von Prof. Dr. Veit Flockerzi (Experimentelle und Klinische Pharmakologie und Toxikologie, Präklinisches Zentrum für Molekulare Signalverarbeitung (PZMS), Universität des Saarlandes) durchgeführt.
- 4. Die TEM-Größenanalyse von Exosomen wurde von mir im Rahmen meiner Masterarbeit durchgeführt.

Weitere Personen waren an der inhaltlich-materiellen Erstellung der vorliegenden Arbeit nicht beteiligt. Insbesondere habe ich nicht die entgeltliche Hilfe von Vermittlungs- bzw. Beratungsdiensten (Promotionsberater/innen oder anderer Personen) in Anspruch genommen.

Außer den Angegebenen hat niemand von mir unmittelbar oder mittelbar geldwerte Leistungen für Arbeiten erhalten, die im Zusammenhang mit dem Inhalt der vorgelegten Dissertation stehen.

Die Arbeit wurde bisher weder im Inland noch im Ausland in gleicher oder ähnlicher Form in einem anderen Verfahren zur Erlangung des Doktorgrades einer anderen Prüfungsbehörde vorgelegt.

Ich versichere an Eides statt, dass ich nach bestem Wissen die Wahrheit gesagt und nichts verschwiegen habe.

Die Bedeutung der eidesstattlichen Versicherung und die strafrechtlichen Folgen einer unrichtigen oder unvollständigen eidesstattlichen Erklärung sind mir bekannt.

Homburg, 02.12.2024

(Unterschrift der/des Promovierenden)
(Unterschrift der die Versicherung an Eides statt aufnehmenden Beamtin bzw. des aufnehmenden
Beamten)

To my family and brother Alaa, I hope you are watching from heaven.

Table of Contents

١.	Introdu	ction	1
	I.1 The	immune system	1
	1.1.1	Innate vs. adaptive immune systems	1
	1.1.2	Cytotoxic T lymphocytes	2
	1.1.3	The immune synapse	3
	1.1.4	Lytic granules	4
	I.2 Killir	ng pathways	9
	1.2.1	Fast killing mechanisms	9
	1.2.2	Slower killing mechanisms	10
	I.3 Extra	acellular vesicles	11
	1.3.1	The history of exosomes	11
	1.3.2	Biogenesis of exosomes	12
	1.3.3	Markers of exosomes	13
	1.3.4	Immune cell derived exosomes	14
	I.4 Ratio	onale and aims of the project	16
II.	Materia	als and methods	17
	II.1 N	1aterials	17
	II.1.1	Chemicals	17
	II.1.2	Commercial kits	19
	II.1.3	Commercial Antibodies	19
	II.1.4	Media and Solutions	21
	II.1.5	Consumables	24
	II.1.6	Devices	25
	II.1.7	Software	27
	II.1.8	Companies	27
	II.1.9	Plasmids	28
	II.1.10	Mounting medium	30
	II.1.11	Cell Lines	30
	II.1.12	Mouse strains	30
	II.2 N	1ethods	30
	II.2.1	Animal housing	30
	11.2.2	Positive isolation of CD8 ⁺ T lymphocytes	30
	II.2.3	Activation of naive CD8 ⁺ T lymphocytes	31

	11.2.4	Subset analysis of CD8 ⁺ T lymphocytes using flow cytometry	31
	11.2.5	P815 cell culture	32
	II.2.6	Electroporation of CTL	32
	II.2.7	Anti-CD3 coated coverslips	33
	II.2.8	Supported lipid bilayer	34
	11.2.9	Total Internal Reflection Fluorescence Microscopy (TIRFM)	34
	II.2.10	TIRF Analysis	35
	II.2.11	Immunostaining CD8 ⁺ T lymphocytes	35
	II.2.12	Gelatin coated coverslips	35
	II.2.13	Organelle isolation	35
	II.2.14	Exosome isolation	38
	II.2.15	Structured illumination microscopy (SIM)	41
	II.2.16	Colocalization analysis of organelles and exosomes	42
	II.2.17	Electron Microscopy.	42
	II.2.18	Expansion Microscopy	44
	II.2.19	Confocal microscopy for expansion microscopy acquisition	45
	II.2.20	Killing assay	46
	II.2.21	Flow cytometry analysis of exosome cytotoxicity	46
	11.2.22	Gel Electrophoresis of Proteins and Sample Preparation for Mass Spectrometry	46
	II.2.23	Nano ESI-LC-MS ² Measurements	47
	11.2.24	Raw LC-MS ² Data Analysis	47
III.	Res	ults	48
I	II.1 E	expression and localization of CD63 and CD81 in cytotoxic T lymphocytes (CTLs)	48
I	II.2 I	nvestigation of fusion kinetics in different cytotoxic organelles of CTLs	50
I	II.3 (CD63-positive exosomes and GzmB-positive SMAPs are released from MCGs	52
		Exosomes released at the immune synapse are derived from MCGs and have a	
	_	neous tetraspanin expression	
		MVBs and MCGs show a heterogeneous expression of v-SNARE proteins	
		CD81 is a more specific exosome marker in murine CTLs	
		Exosomes derived from murine CTLs could be divided into two subpopulations based	
		LOX expansion of exosomes derived from murine CTLs showed that the tetraspanins	
		1 locate to different exosomal subpopulations	
ı	1 9.11	Murine CTL derived exosomes contained in MVBs are secreted in a MUNC13-4	
i	ndepend	dent manner	64

	III.10	Exosomes derived from WT and MUNC13-4 KO CTLs possess cytotoxic activity	66
IV	' .	Discussion	68
	IV.1	Exosomes are contained in two distinct organelles in murine CTLs	68
	IV.2	CD81 is the specific tetraspanin for exosome characterization in murine CTLs	69
	IV.3	Exosome-containing organelles have distinct fusion characteristics compared to SC	Gs 70
	IV.4	Role of MUNC13-4 in exosome secretion	71
	IV.5	Role of SNARE proteins	72
	IV.6	Heterogeneity of tetraspanins expression on exosome-containing organelles	72
	IV.7	Exosomes derived from murine CTLs are divided into two subpopulations based on	their
	surfa	ce marker	73
	IV.8	Polarized exosomes are more cytotoxic than non-polarized exosomes	74
٧.	. Ou	ıtlook	76
VI	l .	Index	78
VI	II.	References	XI
VI	III.	Publications and Conferences.	XXI
ΙX		Acknowledgment	XXIII

List of Figures

Figure 1: The three lines of defense against infection	2
Figure 2: The immune synapse.	4
Figure 3: Molecular processes involved in cytotoxic granule journey from docking to recycling	9
Figure 4: Extracellular vesicle biogenesis	13
Figure 5: Exosome markers.	14
Figure 6: Vector maps of the different constructs used for electroporating primary murine CTLs	29
Figure 7: Flow cytometry analysis of CTL subsets in Munc13-4 KO and WT cells	32
Figure 8: Effect of recovery media on cell viability, transfection efficiency, and secretion in mu	ırine
CTLs.	33
Figure 9: Schematic representation of the organelle isolation procedure from murine CTLs mod	ified
from Schirra et al. (2023).	37
Figure 10: Schematic representation of exosome cell culture and isolation procedure from prin	nary
murine CTLs	39
Figure 11: Schematic representation of exosome staining and expansion procedure	45
Figure 12: Colocalization analysis of exosome markers in murine CTLs	48
Figure 13: CD81 is a more specific exosome marker in murine CTLs than CD63	50
Figure 14: CD63 marks cytotoxic organelles with different fusion kinetics	52
Figure 15: Visualization of exosomes and SMAPs release from MCGs at the immune synapse	54
Figure 16: Exosomes containing organelles show heterogeneity in the expression of tetraspanins.	56
Figure 17: Subcellular fractionation of MVBs, MCGs, and SCGs from murine CTLs	57
Figure 18: The SNARE protein VAMP7 specifically labels MVBs and MCGs containing exosomes	58
Figure 19: The tetraspanin CD81 is a more specific exosome marker in murine CTLs than CD63	60
Figure 20: Characterization of exosomes isolated from murine CTLs.	61
Figure 21: Proteomic analysis of exosomes isolated from WT murine CTLs.	62
Figure 22: Immunostaining of isolated exosomes revelaed a heterogeneous tetraspanin express	sion.
	63
Figure 23: Exosomes derived from murine CTLs are divided based on their tetraspanins surface ma	ırker
into two subpopulations, CD63-positive and CD81-positive exosomes	64
Figure 24: MUNC13-4 KO CTLs secrete exosomes with a similar morphology to the WT exosomes.	65
Figure 25: Cytotoxicity and molecular mechanisms involved in the killing of P815 tumor cell line	s by
CTL-derived exosomes.	67
Figure 26: Characterization of exosomes derived from murine CTLs	77

Abbreviations

% Percent

 β me Beta-mercaptoethanol

°C Degree Celsius

μl Microliter
μm Micrometer
μs Microsecond

ALIX Apoptosis-linked gene 2-interacting protein X

APC Antigen-presenting cell

AU Arbitrary unit

BSA Bovine serum albumin

Ca²⁺ Calcium

CaCl₂ Calcium chloride
CG Cytotoxic granule

CLEM Correlative light electron microscopy

CO₂ Carbon dioxide

CTL Cytotoxic T lymphocyte

DC Dendritic cell

ddH2O Double distilled water

DED Death effector domain

DGK α Diacylglycerol kinase α

DISC Death-inducing signaling complex

N, N-methylene bisacrylamide

DMSO Dimethyl sulfoxide

DNA Deoxyribonucleic acid

D-PBS Dulbecco's phosphate buffer saline

DTT Dithiothreitol

EDTA Ethylenediaminetetracetate
EEA1 Early endosome antigen 1

ER Endoplasmic reticulum

ESCRT Endosomal Sorting Complexes Required for Transport

EV Extracellular vesicle

ExM Expansion microscopy

Fab Fragment antigen binding

FADD FAS-associated death domain

FCS Fecal calf serum

FDR False discovery rate

FHL3 Familial hemophagocytic lymphohistiocytosis type 3

g Gram

GM-CSF Granulocyte-macrophage colony-stimulating factor

GS2 Griscelli syndrome type 2

GSDM Gasdermin
GzmB Granzyme B

HCC Hepatocellular carcinoma

HCl Hydrochloric acid

HEPES 4-(2-hydroxyethyl)-1-piperazineethanesulfonic acid

HRP Horseradish peroxidase
HSP Housekeeping protein

Hz Herz

ICAM-1 Intercellular adhesion molecule-1

IgG Immunoglobulin G

IL Interleukin

ILC Innate lymphoid cells
ILV Intraluminal vesicle

IS Immunological synapse

kb kilobase

KCl Potassium chloride

kDa Kilo Dalton

KHCO₃ Potassium bicarbonate

KI Knock-in
KO Knock-out

KPS Potassium persulfate

LAMP Lysosomal associated protein

LBPA Lysobisphosphatidic acid

LFA-1 Lymphocyte function-associated antigen 1

M Molar

M6P Mannose-6-phosphate

MCG Multicore granule

MgCl₂ Magnesium chloride

MHC Major histocompatibility complex

MISEV Minimal information for studies of extracellular vesicles

ml Milliliter

mm Millimeter

MOPS 3-(N-morpholino) propane sulfonic acid

MPR M6P receptor

MTOC Microtubule organizing center

MVB Multivesicular body

MVE Multivesicular endosome

NaCl Sodium chloride

NaHCO₃ Sodium bicarbonate

NaOH Sodium hydroxide

NH₄Cl Ammonium chloride

NHS N-hydroxysuccinimide

NK Natural killer

nm nanometer

NSF N-ethylmaleimide-sensitive factor

nSMase2 Sphingomyelinase 2

PFA Paraformaldehyde

pH Potential hydrogen

PI Propidium iodide

PLD2 Phospholipase D2

PNS Post-nuclear supernatant

Prf Perforin

RM Recovery media
RNA Ribonucleic acid

RPMI Roswell Park Memorial Institute

s Second

SA Sodium acrylamide SCG Single core granule

SDS Sodium dodecyl sulfate

SEP Super ecliptic pHluorin

SIM Structured illumination microscopy

SiR Silicon Rhodamine

SLP Synaptotagmin like protein

SMAC Supra-molecular activation cluster

SMAP Supramolecular attack particle

SNARE Soluble *N*-ethylmaleimide-sensitive factor attachment protein receptor

STED Stimulated emission depletion microscopy

TBS Tris-buffered saline

TCR T cell receptor

TEM Transmission electron microscopy

TEMED N, N, N', N'-tetramethylene-1,2-diamine

TGN Trans Golgi network

TIRFM Total internal reflection fluorescent microscopy

TMD Transmembrane domain

TME Tumor microenvironment

T_{regs} Regulatory T cells

TSG101 Tumor susceptibility gene 101

t-SNARE Target-SNARE

TSP-1 Thrombospondin-1

U Unit

UV Ultraviolet

VAMP Vesicle-associated membrane protein

v-SNARE Vesicular-SNARE

WB Western blot

WT Wild type

 α 1 Na+/K+ ATPase α 1 sodium potassium adenosinetriphosphatase

 $\alpha\text{-SNAP} \qquad \qquad \alpha\text{-soluble N-ethylmaleimide-sensitive factor}$

Abstract

Exosomes are small extracellular vesicles (30-150 nm) secreted by virtually all cell types. Exosomes play a pivotal role in intercellular communication through the transfer of bioactive molecules, including proteins, lipids, and RNAs. Despite their significance in immune modulation and tumor suppression, the mechanisms underlying their biogenesis and release from cytotoxic T lymphocytes (CTLs) and their function in the immune system are poorly understood. CTLs are essential for adaptive immunity, in which their cytotoxic machinery is used to target infected or malignant cells. In this study, we have characterized exosomes derived from murine CTLs and investigated their secretion dynamics and functional properties. We show that CTL-derived exosomes are packaged in two distinct types of organelles: multivesicular bodies (MVBs) and multicore granules (MCGs). Using structured illumination microscopy (SIM) and correlative light and electron microscopy (CLEM), we identified CD81 as a more specific marker for CTL exosomes than the currently used marker, CD63, which also marks single-core granules (SCGs). Total internal reflection fluorescence microscopy (TIRFM) studies revealed polarized secretion of MCG-derived exosomes at the immune synapse, while MVB-derived exosomes were released in a non-polarized manner. Notably, MCG secretion was MUNC13-4dependent, contrasting with the MUNC13-4-independent secretion of MVBs. Furthermore, SNARE profiling revealed VAMP7 specificity to MVBs, distinguishing them from MCGs and SCGs. Isolated CTLderived exosomes displayed heterogeneity in size and surface markers, as shown by sucrose density gradient centrifugation, transmission electron microscopy (TEM), and immune labeling. Using a 10X expansion method, we identified two exosome subpopulations based on tetraspanin expression: smaller CD81-positive exosomes and larger CD63-positive ones. Functional assays demonstrated that wild-type CTL-derived exosomes efficiently induced caspase-3-mediated apoptosis in target cells, while MUNC13-4 knockout CTLs, deficient in MCG-mediated exosome secretion, showed reduced cytotoxic efficacy.

These findings elucidate the regulated biogenesis and secretion of CTL-derived exosomes and their distinct roles in cytotoxicity, providing new insights into immune regulation. By highlighting exosome heterogeneity and their potential in cancer immunotherapy, this work lays the foundation for leveraging CTL-derived exosomes as novel therapeutic agents.

Zusammenfassung

Exosomen sind kleine extrazelluläre Vesikel (30-150 nm), die von nahezu allen Zelltypen sezerniert werden. Exosomen spielen eine entscheidende Rolle in der interzellulären Kommunikation durch den Transfer von bioaktiven Molekülen, einschließlich Proteinen, Lipiden und RNAs. Trotz ihrer Bedeutung in der Immunmodulation und Tumorsuppression sind die Mechanismen, die ihrer Biogenese und Freisetzung aus zytotoxischen T-Lymphozyten (CTLs) zugrunde liegen, sowie ihre Funktion im Immunsystem noch wenig verstanden. CTLs sind für die adaptive Immunität essenziell, wobei ihre zytotoxische Maschinerie eingesetzt wird, um infizierte oder maligne Zellen anzugreifen. In dieser Studie haben wir Exosomen aus murinen CTLs charakterisiert und ihre Sekretionsdynamik sowie funktionelle Eigenschaften untersucht. Wir zeigen, dass CTL-abgeleitete Exosomen in zwei verschiedene Arten von Organellen verpackt sind: multivesikuläre Körper (MVBs) und Multikerngranula (MCGs). Mithilfe der strukturierten Beleuchtungmikroskopie (SIM) und korrelativer Licht- und Elektronenmikroskopie (CLEM) identifizierten wir CD81 als spezifischeren Marker für CTL-Exosomen im Vergleich zum derzeit verwendeten Marker CD63, der auch Einzelkerngranula (SCGs) markiert. Studien mit totaler interner Reflexionsfluoreszenzmikroskopie (TIRFM) zeigten eine polarisierte Sekretion von MCG-abgeleiteten Exosomen an der Immunsynapse, während MVBabgeleitete Exosomen auf nicht-polarisierte Weise freigesetzt wurden. Bemerkenswerterweise war die MCG-Fusion MUNC13-4-abhängig, im Gegensatz zur MUNC13-4-unabhängigen Fusion von MVBs. Darüber hinaus ergab das SNARE-Profiling eine VAMP7-Spezifität für MVBs, die diese von MCGs und SCGs unterscheidet. Isolierte CTL-abgeleitete Exosome zeigten eine Heterogenität in Größe und Oberflächenmarkern, wie durch Sucrose-Dichtegradientenzentrifugation, Elektronenmikroskopie (TEM) und Immunfärbung gezeigt wurde. Mit einer 10X-Expansionsmethode identifizierten wir zwei Exosomen-Subpopulationen basierend auf der Tetraspanin-Expression: kleinere CD81-positive Exosomen und größere CD63-positive Exosomen. Funktionelle Assays zeigten, dass Wildtyp-CTL-abgeleitete Exosomen effizient die Caspase-3-vermittelte Apoptose in Zielzellen induzierten, während MUNC13-4-Knockout-CTLs, die in der MCG-vermittelten Exosomen-Sekretion defizient waren, eine reduzierte zytotoxische Effizienz aufwiesen. Diese Ergebnisse erhellen die regulierte Biogenese und Sekretion von CTL-abgeleiteten Exosomen und ihre unterschiedlichen Rollen in der Zytotoxizität, was neue Einblicke in die Immunregulation bietet. Durch die Hervorhebung der Heterogenität von Exosomen und ihrem Potenzial in der Krebsimmuntherapie legt diese Arbeit die Grundlage für die Nutzung von CTL-abgeleiteten Exosomen als neuartige therapeutische Agenzien.

I. Introduction

I.1 The immune system

I.1.1 Innate vs. adaptive immune systems

We live in a world full of pathogens, yet we rarely get sick. This can be attributed to the remarkable efficacy of our immune system. The immune system consists of various cells, tissues, and organs that work together to protect our body from harmful invaders including bacteria, parasites, fungi, toxins, and viruses. The initial line of defense, comprising chemical and mechanical barriers, effectively excludes most pathogens. This is made up of the skin, which acts as a physical barrier that prevents the passage of any foreign substance (Figure 1). For instance, the openings of the skin, such as the eyes and mouth, are protected by tears and saliva respectively. These have enzymes that destroy bacterial cell walls (Chia and McClure 2020). If an intruding pathogen succeeds in breaching the initial barrier, the second line of defense, consisting of cells of the innate immune system, comes into action. The innate immune system consists of phagocytes, neutrophils, natural killer (NK) cells, and innate lymphoid cells (ILC) (Figure 1) (Favaro et al. 2022). It is responsible for initiating a non-specific but rapid response to eliminate intruders. This is achieved through a variety of mechanisms (Turvey and Broide 2010). Phagocytes, for example, can recognize common molecular patterns on the surface of bacteria or microbes. This leads to the generation of an inflammatory response in which the innate immune cells phagocytose the invading pathogens and eliminate them immediately on site (Takeuchi and Akira 2010; Riera Romo, Pérez-Martínez, and Castillo Ferrer 2016). In case these cells are unable to destroy the pathogen on their own, then the third and last line of defense, consisting of the adaptive immune system's cells, takes over. The establishment of the adaptive immune response takes a longer time than that of the innate response, but it is antigen-specific and enables long-lasting immunity through the formation of immunological memory to renewed antigen contact. The adaptive immune response consists of the humoral immune response generated by B lymphocytes and the cellmediated response controlled by Tlymphocytes (Figure 1) (Bonilla and Oettgen 2010). Upon activation, after corresponding antigen contact, B lymphocytes differentiate into plasma cells and produce antibodies against the invasive pathogen. These antibodies specifically neutralize pathogens and prevent them from entering host cells. Another subset of lymphocytes, the T lymphocytes, are the major players in the cell-mediated immune response. T lymphocytes can be further divided into CD4⁺ and CD8⁺ T cells and are initially generated as naive cells. These cells are not yet functional, but they express specific receptor for a particular antigen. T lymphocytes are unable to recognize unbound antigens. They can only recognize processed antigens presented by Major Histocompatibility Complex molecules (MHC) I or II on the surface of antigen-presenting cells (APCs), such as dendritic cells (DCs) and macrophages. CD8⁺ T cells recognize antigens bound to MHC I and CD4⁺ T cells bind to antigens presented by MHC II (Babbitt et al. 1985; Gulati 2009). Although CD4⁺ and CD8⁺ T cells share a similar activation procedure, they carry divergent functions. CD4⁺ T cells are also known as helper T cells due to their essential role in coordinating the immune response. Once activated, these helper cells secrete an array of cytokines that further activate other immune cells including B cells, CD8⁺ T cells, and macrophages. CD8⁺ T cells, also known as cytotoxic T lymphocytes (CTLs), are antigen-specific killer cells of the immune system which recognize and kill virally infected or cancerous cells (Bonilla and Oettgen 2010; Gulati 2009).

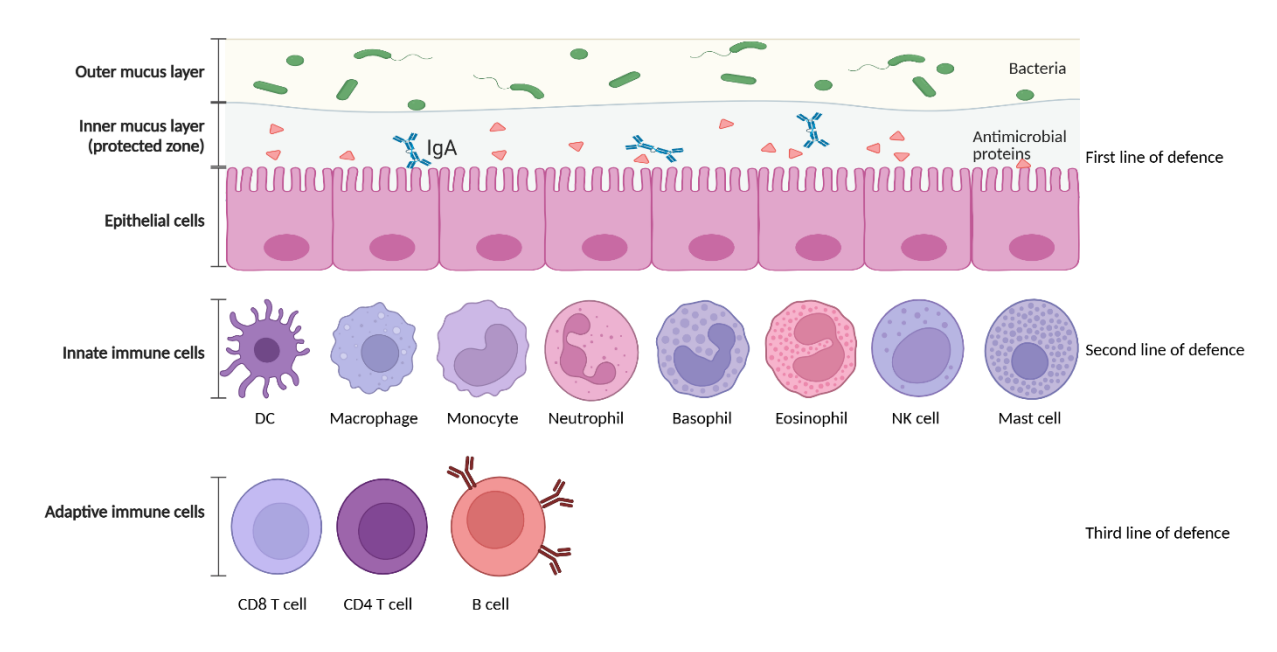


Figure 1: The three lines of defense against infection.

A schematic diagram depicting the body's three lines of defense against pathogens. The first line of defense consists of physical and chemical barriers, including the skin and mucous membranes, which prevent pathogen entry. The second line of defense involves innate immune cells, featuring phagocytic cells (such as macrophages and neutrophils) and natural killer (NK) cells, which target and destroy invaders. The third line of defense represents adaptive immune responses, characterized by the activity of T and B lymphocytes. T cells destroy infected cells and assist other immune cells, while B cells produce antibodies and form memory cells for long-term immunity. Figure inspired by (Richman et al., 2017).

I.1.2 Cytotoxic T lymphocytes

Naive CD8⁺ T cells are derived from the lymphoid progenitor cells in the bone marrow. Following their production, they migrate directly to the thymus, where they mature. Mature naive CD8⁺ T cells are then ready to patrol our body searching for cells that have been altered through infection or transformation (Koh et al. 2023). Each CD8⁺ T cell has a unique T cell receptor (TCR), capable of recognizing a specific peptide in complex with MHC I. This confers CD8⁺ T cells a high level of specificity. Once in contact with a potential target, naive CD8⁺ T cells engage adhesion molecules such as lymphocyte function-associated antigen 1 (LFA-1) on their surface and intercellular adhesion molecule 1 (ICAM-1) on target cells to form transient conjugates (Raskov et al. 2021). At this stage,

naive CD8⁺ T cells engage in an actin cytoskeleton-dependent scanning of the target cell surface. If no antigen is detected, the naive CD8⁺ T cells rapidly disengage from their targets and resume migration. Conversely, upon locating a target cell with antigenic peptide-MHC I, a naive CD8⁺ T cell exhibits extensive actin cytoskeletal remodeling and LFA-1 conformational changes which increase their affinity to ICAM-1 on the target cell surface (Yannelli et al. 1986). Remarkably, the initial activation of naive CD8⁺ T cells requires the recognition of less than 10 antigenic peptides on the surface of APCs (Sancho et al. 2002; Iezzi, Karjalainen, and Lanzavecchia 1998; Irvine et al. 2002; Mempel, Henrickson, and Von Andrian 2004). This results in the suppression of naive T cells' locomotion and the establishment of a strong contact between the naive CD8⁺ T cell and the APC. This interaction persists for 6-18 hours through which a cascade of signaling events develops and leads to the differentiation of naive CD8⁺ T cells into a specific clone of effector CTLs (Kupfer and Singer 1989; Dustin et al. 1997; Mempel, Henrickson, and Von Andrian 2004).

I.1.3 The immune synapse

Upon the activation of the CTL by a DC, the CTL is now able to scan the body for infected cells. Once detected, the CTL forms close contact with the target cell that lasts 20-30 minutes. This specialized supramolecular structure is called the immunological synapse (IS) (Gunzer et al. 2000). The formation of the IS triggers the polarization of the newly synthesized cytotoxic granules (CGs) toward the IS. The CGs then fuse with the plasma membrane and release their cytotoxic content to trigger the death of the target cell (Stinchcombe et al. 2006). The formation of the IS is dispensable for the killing activity of CTLs and is triggered by the interaction between the adhesion molecule LFA-1 on the surface of CTLs and ICAM-1 on the target cell. This leads to the recruitment and accumulation of a multiplex of organelles and proteins to the supra-molecular activation cluster (SMAC) (Kuhn and Poenie 2002). SMACs are concentric domains that are divided into three regions: central, peripheral, and distal (Figure 2). At the initial state of contact, actin filaments are concentrated at the central SMAC (cSMAC) for a very short time. Thereafter, they re-localize to the distal SMAC (dSMAC), paving the way for the clustering of TCR and TCR-associated proteins at the cSMAC. Surrounding the cSMAC is a ring of adhesion molecules (LFA-1) and their adaptor, talin, collectively known as the peripheral SMAC (pSMAC). The region surrounding the pSMAC is called the distal SMAC (dSMAC), where actin accumulates (Monks et al. 1998; Dustin 2014). The assembly of the IS is coordinated by the cytoskeleton. Following TCR stimulation, the microtubule-organizing center (MTOC) is polarized towards the synapse, where it docks in an actin-depleted region adjacent to the cSMAC (Figure 2). CGs aggregate around the centrosome and move with it to the synapse, where they merge with the plasma membrane and discharge their cytotoxic content to kill the target cell (Dustin, Chakraborty, and Shaw 2010; Dustin 2014).

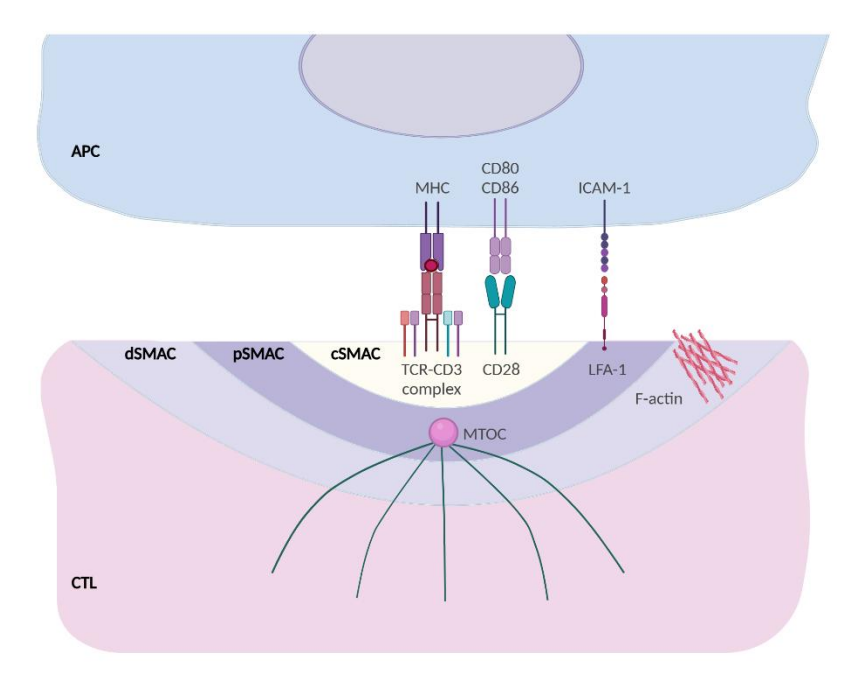


Figure 2: The immune synapse.

A schematic diagram representing the immunological synapse (IS) formed between a CD8⁺ T cell and an antigen-presenting cell (APC). Within the IS, distinct clusters organize its structure. The central supramolecular activation cluster (cSMAC) contains T cell receptors (TCRs) and the costimulatory receptor CD28. Surrounding this core, the peripheral SMAC (pSMAC) is enriched in integrin LFA-1. Further out, the distal SMAC (dSMAC) is the region of F-actin accumulation. The microtubule-organizing center (MTOC) translocates toward the IS, facilitating the trafficking of cytotoxic granules toward the contact zone. Figure inspired by (Capitani and Baldari 2022).

I.1.4 Lytic granules

I.1.4.1 Single Core Granules

A critical step of target cell killing is the delivery of cytotoxic components to the infected or malignant target cells. One of the earliest CGs to be characterized in CTLs was the single core granule (SCG). SCGs are referred to as hybrid organelles due to their unique feature of having secretory and lysosomal components sorted into them. This feature gives them the ability to store cytotoxic proteins before their secretion, as well as to perform the conventional lysosomal role of protein and molecule degradation. (Burkhardt et al. 1990; Peters et al. 1991; Blott and Griffiths 2002). Like lysosomes, SCGs contain lysosomal-associated proteins such as LAMP-1 and LAMP-2, lysosomal hydrolases (cathepsins), and lysosomal transmembrane protein CD63 (Fukuda 1991; Metzelaar et al. 1991). They possess an acidic pH of 5.9 that is maintained through the presence of the a3 subunit of the V-ATPase. This acidic pH is imperative for the optimal function of the lysosomal enzymes (Chitirala et al. 2020). Furthermore, they share a similar morphology with lysosomes. Nevertheless, the distinguishing feature of SCGs is their ability to perform regulated exocytosis (Blott and Griffiths 2002). SCGs have a diameter of 293 ± 8 nm and a distinctive electron-dense core, which is composed of the soluble lytic proteins. SCGs contain the pore-forming protein perforin (Prf), the serine proteases granzymes (Gzm)

A and B, and the chondroitin sulfate proteoglycan (serglycin), as their main cytolytic content. Cytolytic proteins are found in their inactive form in SCGs. Perforin and granzyme are held together on a scaffold of serglycin which gives the SCG its dense core (Chang et al. 2022; Peters et al. 1991).

I.1.4.2 Multi-Core Granules

For a long time, it had been thought that SCGs containing perforins and granzymes are the only cytotoxic organelles in CTLs. However, recent studies have delivered new prominent CG candidates that play an important role in CTL cytotoxicity. Bálint et al. (2020) have identified supramolecular attack particles (SMAPs) as novel cytotoxic particles in human CTLs which consist of a thrombospondin-1 (TSP-1) glycoprotein shell engulfing a core enriched in cytotoxic proteins such as perforin, granzyme, and serglycin. TSP-1 is a calcium-binding protein of the extracellular matrix that functions in cell-cell and cell-matrix interactions. Another characteristic feature of SMAPs is their lack of a surrounding phospholipid membrane (Bissinger et al. 2020). Two years later, Chang et al. (2022) demonstrated that SMAPs are contained in organelles bearing multiple dense cores that show heterogeneity in size and appearance. Hence, these organelles are referred to as multicore granules (MCGs) and have a size of 364 ± 12 nm. These organelles are present in mouse and human CTLs as well as in NK cells (Chang et al. 2022; Ambrose et al. 2020). In addition to the presence of multiple dense core particles corresponding to SMAPs, MCGs also contain particles with lower electron density. Proteomic analysis revealed the presence of exosome-related markers, suggesting that SMAPs and exosomes coexist within MCGs. Fusion of MCGs from mouse CTLs releases intact SMAPs containing GzmB and TSP-1. Moreover, the presence of vesicle-associated membrane protein 2 (VAMP2) on the surface of MCGs indicates that their fusion, similar to SCGs, is soluble N-ethylmaleimide-sensitive factor attachment protein receptor (SNARE) dependent. Whether the fusion of MCGs is restricted to the synaptic area is unknown. It is unlikely that SCGs and MCGs are generated via similar pathways, as proteomic analysis shows differences in protein contents with SCGs being enriched in lysosomal proteins and MCGs in endosomal trafficking proteins (Chang et al. 2022).

I.1.4.3 Lytic granules content

The first important cytolytic protein contained in lytic granules is perforin. It is synthesized as a 70-KDa protein precursor in the endoplasmic reticulum (ER). Perforin is then transported to the lytic granule via the Golgi apparatus. Within the ER and Golgi, the C-terminal end of perforin undergoes extensive N-glycosylation, preventing perforin oligomerization and activity within these organelles (Brennan et al. 2011). Perforin is inactive in the acidic environment of the lytic granule. Upon reaching CGs, cathepsin L cleaves 12-20 amino acids from the C-terminus of perforin, exposing a C2

phospholipid-binding domain (Konjar et al. 2010; Uellner et al. 1997). This exposure enables perforin to bind to lipids in a calcium-dependent manner, facilitating its pore-forming cytolytic activity. In CGs, perforin is maintained as a monomer in a complex with serglycin, which inhibits its activity. Furthermore, since perforin activity is dependent on calcium, the presence of acidic pH as well as the calcium-binding protein (calreticulin) in CGs inhibit the activity of perforin (Voskoboinik, Smyth, and Trapani 2006; Fraser et al. 2000).

The other important cytolytic proteins in CGs are the granzymes, which belong to the family of serine proteases. In mouse CTLs, eight granzymes have been identified (A, B, C, D, E, F, G, and H), with GzmB being the best characterized. Like perforin, granzymes are produced as inactive precursors containing an inhibitory dipeptide (Jenne and Tschopp 1988; Aubert et al. 2024). Due to a signal peptide, they are directed to the ER from where they are sorted to the trans-Golgi network (TGN), where they acquire the mannose-6-phosphate (M6P) moiety. Granzymes are subsequently transported to the late endosomes and CGs via the M6P receptor (MPR) (Griffiths and Isaaz 1993). Within the CGs, cathepsins remove the inhibitory dipeptide, leading to the maturation of granzymes into their active form (Meade et al. 2006; D'Angelo et al. 2010; Smyth, McGuire, and Thia 1995). However, the acidic environment and the sequestration of granzymes by serglycin maintain granzymes in an inactive state until they are released to exert their cytolytic function (Chowdhury and Lieberman 2008).

Upon CTL activation, the fusion of the CG with the plasma membrane results in neutralization of the pH. This increase in pH facilitates the dissociation of perforin from serglycin, allowing perforin to bind to calcium and initiate its polymerization. Perforin then forms pores in the target cell membrane allowing the direct entry of GzmB to the target cells. Alternatively, both perforin and GzmB can be internalized by the target cell, after which perforin initiates pore formation, releasing GzmB into the cytosol of the target cell (Voskoboinik, Whisstock, and Trapani 2015).

I.1.4.4 Lytic granules fusion and degranulation are mediated by SNARE proteins

CGs have specialized machinery to enable their regulated secretion, a feature that differentiates them from conventional lysosomes. CTL activation and the formation of an IS between the CTL and the target cell initiates a cascade of events that results in the docking, priming, and fusion of CGs. These events are orchestrated by the SNARE complexes. The SNARE complex, a 76 KDa assembly, is responsible for almost all fusion events, including the intracellular trafficking and fusion of Golgi transport vesicles (Block et al. 1988; Weidman et al. 1989). Eventually, it was demonstrated that SNARE proteins are the primary machinery for vesicle fusion at synaptic release sites in neurons (Söllner, Whiteheart, et al. 1993). SNAREs are classified into two categories based on their membrane localization: vesicular membrane-associated proteins (v-SNAREs) and plasma membrane-associated

proteins (t-SNAREs). All SNARE proteins share a conserved SNARE motif, a 60-amino-acid stretch arranged in heptad repeats (Sutton et al. 1998). For regulated exocytosis, the v-SNARE synaptobrevin 2 (VAMP2) in mice (Matti et al. 2013) and synaptobrevin 7 (VAMP7) in humans (Chitirala et al. 2019) contain one SNARE motif and are anchored to the plasma membrane through their helical transmembrane domain (TMD) located at their carboxyl terminus. Similarly, the t-SNARE syntaxin 11, harbors one SNARE motif but is anchored to the cytoplasmic membrane through lipid modifications, its N-terminal extension forms a three-helical bundle (Habc domain), which interacts with the Munc18-2 protein upstream of the SNARE assembly domain (Tang, Low, and Hong 1998; Prekeris, Klumperman, and Scheller 2000; Müller et al. 2014). The other t-SNARE, known as synaptosomal-associated protein 23 (SNAP 23), contains two SNARE motifs but lacks a TMD. However, SNAP 23 binds to the inner leaflet of the plasma membrane through its palmitoylated linker sequence (Ravichandran, Chawla, and Roche 1996). On their own, SNARE proteins do not perform any function but as a ternary complex (one v-SNARE, one Syntaxin 11, and one SNAP23) they mediate the CG fusion with the plasma membrane. This process is analogous to the mechanism described by Söllner, Bennett, et al. (1993) and Söllner, Whiteheart, et al. (1993) for intracellular vesicle trafficking.

CG docking. Following MTOC polymerization and the movement of the CGs toward the IS, the CGs dock at the plasma membrane of the CTL in preparation for fusion (Figure 3). This process can occur via two pathways. The first pathway was identified through studies on patients with Griscelli syndrome type 2 (GS2), characterized by reduced cytotoxicity of CTLs and NK cells. Patients with GS2 have a biallelic mutation in the gene encoding Rab27a, a member of the Rab family of small GTPases that play an important role in vesicle traffic and compartmentalization (Ménasché et al. 2000) (Figure 3). In CTLs, Rab27a knock-down results in the failure of SCG docking to the plasma membrane (Haddad et al. 2001). Rab27a interacts with synaptotagmin-like proteins (SLP1 and SLP2). SLP proteins have a phospholipid-binding domain that integrates into the plasma membrane and an N-terminal SLP homology domain that binds to the switch II region of Rab27a, facilitating the tethering of Rab27a to the plasma membrane (Holt et al. 2008; Fukuda 2013; Kurowska et al. 2012). The second docking strategy involves Munc18-2 and syntaxin 11 (Figure 3). Although the exact role of this pair is not fully understood, it is believed that they aid in initiating the assembly of the SNARE complex. This complex is essential for the fusion of CGs with the plasma membrane, leading to the release of cytolytic proteins (Becherer and Rettig 2006).

CG priming. Once the CGs are tethered to the plasma membrane they must become fusion-competent, a process known as priming. Only primed CGs can fuse with the plasma membrane,

hence this step regulates the number of fusing CGs per cell. Priming is mediated by the Munc13 family of proteins which consists of four members, Munc13-1 to 4, with Munc13-1 being the priming factor of synaptic vesicles in brain and neuroendocrine glands (Feldmann et al. 2003; Wang et al. 2019). Similar to the other Munc13 family members, Munc13-4 has two C2 domains and the Munc homology domains (MHD) however, it differs from the other family members by not having the N-terminal diacylglycerol-binding C1 domain (Neeft et al. 2005). Patients with Munc13-4 gene mutations develop familial hemophagocytic lymphohistiocytosis type 3 (FHL3) which is characterized by a severe loss in CTL and NK cell-killing efficiency. Munc13-4 appears to be required for priming CGs (Feldmann et al. 2003). Mouse CTLs express only two isoforms of the Munc13 family, Munc13-1 and Munc13-4, with Munc13-1 being able to rescue the defective phenotype observed in Munc13-4 KO CTLs. Interestingly, the knockdown of Munc13-1 further reduced CG fusion at the IS, suggesting a role of Munc13-1 in the priming of CGs in mouse CTLs (Dudenhöffer-Pfeifer et al. 2013). Priming of CGs is initiated with the formation of the trans SNARE-complex, that allows the positioning of the vesicle near the plasma membrane. This is facilitated by Munc13-4 and Munc18-2, which are responsible for the assembly of the SNARE complex in a calcium-dependent manner (Figure 3) (Wang et al. 2019; Meunier and Hu 2023). Munc13-4 interacts with syntaxin 11 but whether it is responsible for opening the conformation of syntaxin 11 is not yet known (Wang et al. 2020).

CG fusion. CGs that are rendered fusion-competent by the priming step, are ready to fuse with the plasma membrane. The fusion of CGs is initiated by the formation of a SNARE complex that consists of syntaxin 11 and SNAP 23 as the t-SNAREs and VAMP2 as the v-SNARE in murine CTLs (Halimani et al. 2014; Bryceson et al. 2007; Matti et al. 2013). This results in the formation of a coiled-coil structure that is highly stable and resistant to high temperatures. Upon an increase in the calcium concentration, the SNARE complex then drives both membranes together and results in the fusion of the CGs with the plasma membrane (Figure 3). Once exocytosis takes place, the SNARE complex is disassembled in an ATP-dependent way through the action of the α -soluble N-ethylmaleimide—sensitive factor attachment protein (α -SNAP) and the N ethylmaleimide—sensitive factor (NSF) (Huang et al. 2019). This renders the SNARE proteins available for another round of secretion which is extremely important in serial killing exerted by CTLs.

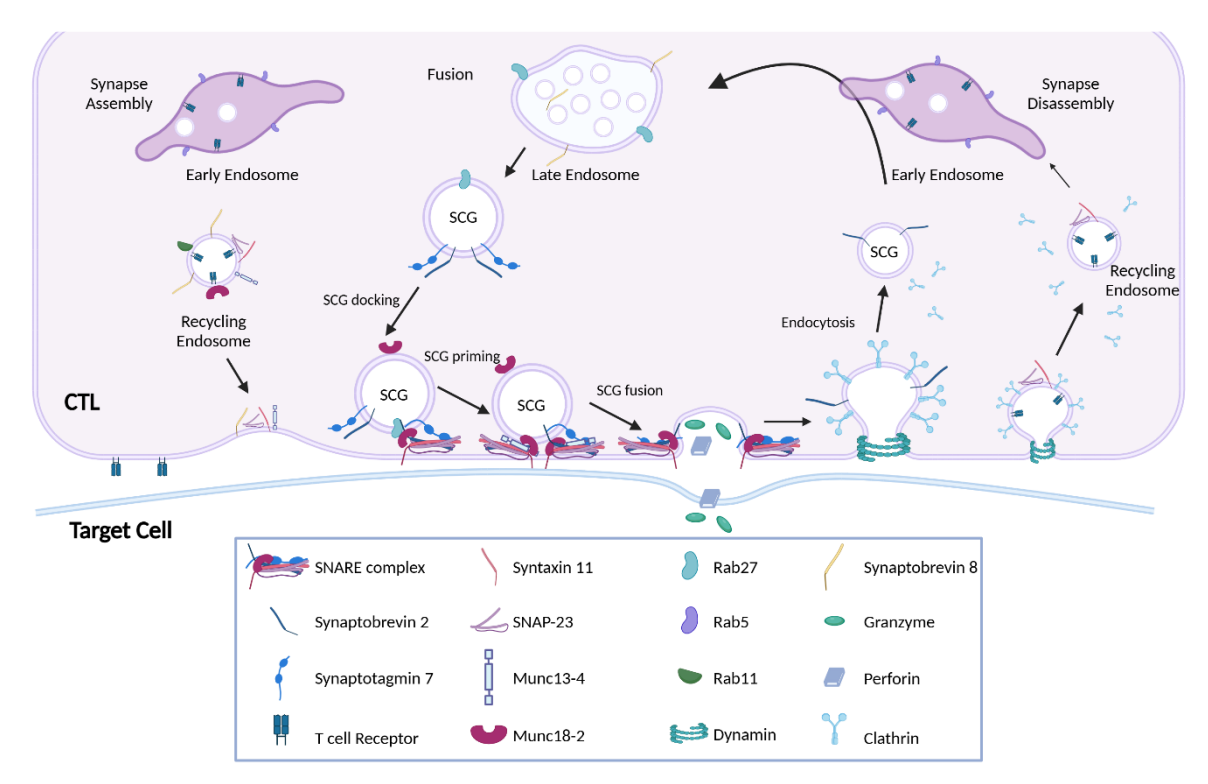


Figure 3: Molecular processes involved in cytotoxic granule journey from docking to recycling.

Synapse assembly is initiated with the fission of recycling endosomes (RE) from early endosomes (EE). The RE then transports in a VAMP8-dependent manner to the synapse, where it fuses with the plasma membrane, delivering essential SNARE proteins needed for single core granule (SCG) docking, priming, and fusion. SCGs mature through interactions with lysosomes and late endosomes before docking at the plasma membrane. They are then primed by Munc13-4, leading to the formation of the SNARE complex, which enables SCGs to fuse with the plasma membrane and release their cytotoxic proteins, granzyme B and perforin. Following this, SNARE proteins are recycled via clathrin-dependent endocytosis, and the resulting RE fuses with the EE to prepare for another round of SCG synthesis. Figure inspired by (Rettig and Stevens 2017).

I.2 Killing pathways

I.2.1 Fast killing mechanisms

Cell death is an important mechanism that keeps the homeostasis of the body. Understanding the mechanisms through which CTLs kill their target cells is fundamental. CTLs kill their target cells through the release of lytic granules containing Prf and GzmB or through the death-receptor mediated Fas/Fas ligand (FasL) pathway. Both pathways induce the apoptosis of the target cells. GzmB is a serine protease that preferentially cleaves after aspartic acid residues, initiating apoptosis by cleaving various intracellular substrates. Key targets include effector caspases like caspase-3 and caspase-7 (Darmon, Nicholson, and Bleackley 1995; Metkar et al. 2003; Andrade et al. 1998). Additionally, GzmB is capable of cleaving the BH3-only protein Bid in target cells, producing a truncated t-Bid form (Pardo et al. 2008; Thomas et al. 2001), and the Bcl-2 protein Mcl-1, which triggers the release of the pro-apoptotic protein Bim (Catalán et al. 2015; Han et al. 2004). Both pathways induce mitochondrial outer membrane permeabilization (MOMP), leading to the release of cytochrome c and other pro-apoptotic factors, such as SMAC/Diablo. This process facilitates apoptosome formation and the complete

activation of caspase-3 and caspase-7, ultimately driving apoptosis (Alimonti et al. 2001; Voskoboinik, Whisstock, and Trapani 2015; Afonina, Cullen, and Martin 2010). Besides inducing apoptosis, GzmB can also directly cleave and activate gasdermin E (GSDME) independently of caspases, triggering caspase-independent pyroptosis (Zhang et al. 2020; Liu et al. 2020). Pyroptosis is an inflammatory form of cell death that is controlled by the gasdermin (GSDM) family. Cleaved GSDMs form transmembrane pores that facilitate the release of IL-1 family of cytokines and disrupt intracellular ion balance, resulting in cell death (Broz, Pelegrín, and Shao 2020). The GSDM family has various members, all activated by caspase-mediated cleavage. Traditionally, activation of GSDMs was linked to inflammatory caspases such as caspase-1, -4, or -5. However, recent findings have revealed that other caspases, including caspase-3 and -8, can also activate various GSDMs in tumor cells that express these proteins. Moreover, it has been demonstrated that during GzmB-mediated cell death, caspase-3 is activated, which then cleaves GSDMs and triggers pyroptosis, thereby linking the GzmB pathway to pyroptotic cell death (Liu et al. 2020).

I.2.2 Slower killing mechanisms

Another well-characterized mechanism utilized by CTLs to kill their target cells is through the induction of death receptor-mediated apoptosis via the Fas/FasL pathway. CTLs express FasL which induces the apoptosis of target cells expressing the Fas receptor. Fas and FasL are transmembrane proteins that belong to the tumor necrosis factor (TNF) superfamily. The expression of FasL is upregulated upon CTL activation and the degranulation of FasL-positive organelles is calcium-independent. The activation of the FAS receptor leads to the recruitment of the adaptor protein FAS-associated death domain (FADD) to the receptor's cytosolic death domain (DD) through homotypic interactions. Subsequently, the death effector domain (DED) in FADD recruits FLIP, procaspase-8, and RIP1, forming a death-inducing signaling complex (DISC) (Walczak and Sprick 2001; Yang et al. 2024). Within the DISC, procaspase-8 molecules are brought into proximity, leading to autocatalytic cleavage and stabilization of caspase-8 in its active form. This active caspase-8 then activates downstream effector caspases in the cytosol, such as caspase-3 and caspase-7. In certain cases, stimulation of death receptors by itself is inadequate to trigger apoptosis through the direct cleavage of caspase-3. In these instances, the activation of Bid by caspase-8 and subsequent engagement of the mitochondrial apoptotic pathway become essential, similar to the process described for GzmB (Scaffidi et al. 1998; Walczak and Sprick 2001).

CTLs contain intracellular pools of prestored FasL in lysosome-related organelles, however, they do not colocalize with Prf and GzmB-containing organelles (He and Ostergaard 2007). In fact, studies have shown that FasL is targeted into multivesicular bodies (MVBs). MVBs are late endosomes and have a size of 600-800 nm. They belong to the endocytic pathway and carry out numerous functions (Hanson

and Cashikar 2012). MVBs were thought to be pre-degradative compartments that carry out waste disposal functions but it is now known that they are also important in signal transduction (Trams et al. 1981). As is the case for SCGs and MCGs, regulated exocytosis controls the fusion of MVBs with the plasma membrane. This regulated exocytosis is also thought to be driven by the SNARE machinery. The SNARE proteins VAMP7, YKT6192, and SNAP23 have been identified as key mediators in the fusion of MVBs in K562, HEK293, and HeLa cells, respectively (Figure 4). However, the exact proteins that play a role in MVB fusion in CTLs are yet to be determined (Fader et al. 2009a; Gross et al. 2012; Verweij et al. 2018).

I.3 Extracellular vesicles

Extracellular vesicles (EVs) constitute a diverse population of membrane-bound vesicles released by nearly all cell types. Based on their subcellular origin, EVs can be divided into three subclasses consisting of exosomes, microvesicles, and apoptotic bodies. Exosomes are smaller EVs with a size range of 30-150 nm in diameter that are formed as intraluminal vesicles (ILVs) contained inside MVBs and are released following the fusion of MVBs with the plasma membrane (Figure 4) (Raposo and Stoorvogel 2013). Microvesicles are the larger EVs (100-1000 nm) and are generated by the outer budding of the plasma membrane (Tricarico, Clancy, and D'Souza-Schorey 2017) (Figure 4). Apoptotic bodies are the largest in size in this family (2-5 µm) and are released as blebs from cells undergoing apoptosis. Despite this classification, there is still a gray area of overlap between the different members of the EV family. To further complicate the scenario, different vesicular subpopulations within the subclasses of EVs exist (Hromada et al. 2017; Mathieu et al. 2021). The field of extracellular vesicles is expanding rapidly, and in the past two decades, it gathered a lot of recognition due to the importance of EVs in intercellular communication and many additional functions carried out by the different members of this family. It is important to note that the Minimal Information for Studies of Extracellular Vesicles (MISEV) update frequently their guidelines, and the term "EV" is preferably used until the origin of the studied vesicles is determined (Welsh et al. 2024).

For clarity, this thesis focuses on the smaller subset of EVs that are contained in MVBs and MCGs and released upon the fusion of these organelles with the plasma membrane, hence the term exosome will be used.

I.3.1 The history of exosomes

The history of exosomes dates to the 1960's where researchers observed membrane-bound particles in extracellular fluids. These particles were considered cellular debris carrying waste out of the cells. In 1981, Trams et al. were the first to convince reviewers that these particles are neither artifacts nor

sewage carriers and they referred to them as "exosomes". Their landmark paper showed for the first time that exosomes can be secreted by a wide variety of cell types (Trams et al. 1981). Two years later, two seminal papers, which were published a week apart by Harding and Stahl (1983) and Pan and Johnstone (1983), demonstrated that exosomes were involved in the selective removal of transferrin receptors from maturing reticulocytes. In their pioneering study, Harding and Stahl (1983) further characterized exosomes, showing these vesicles were in MVBs and hence they named these organelles multivesicular endosomes (MVE). This was in fact the first study that demonstrated the mechanism through which exosomes are released from the cells. In the 1990s, research uncovered the broader biological significance of exosomes, with Raposo et al. (1996) discovering that B lymphocytes secrete exosomes bearing MHC II molecules and could activate T-cell responses. Zitvogel et al. (1998) also showed that DCs secrete exosomes that could induce antitumor immune responses, highlighting their potential in cancer immunotherapy. The 2000s saw a rapid expansion in exosome research, driven by advances in molecular biology and proteomics. Valadi et al. (2007) identified that exosomes carry mRNA and miRNA molecules. Théry et al. (2006) provided a comprehensive overview of their molecular composition, establishing standardized methods for their isolation and characterization. Since then, numerous studies have been conducted to explore the nature of exosomes in depth, investigating the lipidomic and proteomic content of EVs. In recent years, the focus has shifted to clinical and therapeutic potential, with studies exploring exosomes as diagnostic biomarkers and evaluating exosome-based therapies. Ongoing research continues to unravel their complex biology, promising to transform our understanding of cellular communication and disease treatment.

I.3.2 Biogenesis of exosomes

Exosome biogenesis is intricately linked to the endosomal pathway. Cells use endocytosis to internalize various proteins and molecules; these internalized vesicles fuse with the early endosome. ILVs are formed by the inward invagination of the endosomal membrane upon early endosomes' maturation into late endosomes. Exosome biogenesis is a highly organized process and is controlled by the Endosomal Sorting Complexes Required for Transport (ESCRT). The ESCRT consists of four multiprotein subcomplexes (ESCRT-0, -I, -II, -III) in addition to the accessory proteins such as VPS4 and ALG-2 interacting protein X (ALIX). ESCRT-O and -I recognize and recruit ubiquitinylated proteins to the endosomal membrane, causing the clustering and clathrin-mediated coating of cargo proteins, which induces deformation of the endosomal membrane. ESCRT-II interacts with ESCRT-0 and -I and recruits ESCRT-III that together with VPS4 are responsible for membrane budding and vesicle scission. VPS4 is an ATPase responsible for dissociating and recycling the ESCRT components (Hurley 2008; Tamai et al. 2010). In fact, ESCRT proteins are not always necessary for exosome biogenesis, as ILVs

were still formed upon silencing key parts of all four ESCRT proteins (Stuffers et al. 2009). Other elements, like tetraspanins (e.g. CD9, CD82, Tspan8, CD63), and the lysosome-related protein SIMPLE, are involved in ESCRT-independent exosome release (Nazarenko et al. 2010; Chairoungdua et al. 2010; Zhu et al. 2013; Hurwitz et al. 2016). Lipids also play a vital role in vesicle formation and transport, influencing membrane curvature, invagination, fission, and fusion (McMahon and Boucrot 2015). For example, inhibiting the enzyme sphingomyelinase 2 (nSMase2) reduces exosome release, likely due to reduced number of ceramide microdomains, which are crucial for membrane budding (Trajkovic et al. 2008). Other lipid-modifying enzymes, such as phospholipase D2 (PLD2) and diacylglycerol kinase α (DGK α), also help regulate ILV formation in exosome biogenesis (Ghossoub et al. 2014; Alonso et al. 2011). The transformation of endosomes into MVBs depends on these various components, which may work alone or together, based on the cell type and its environment (Maas, Breakefield, and Weaver 2017).

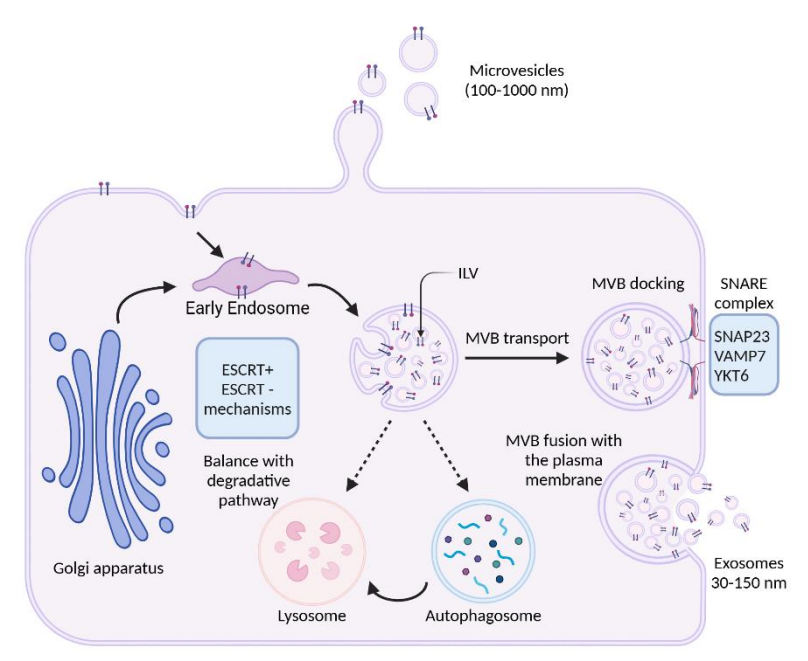


Figure 4: Extracellular vesicle biogenesis.

Microvesicles are the larger extracellular vesicles that bud from the plasma membrane. However, the biogenesis of the smaller extracellular vesicles, known as exosomes, is more intricate and occurs through the endosomal pathway. This process occurs in an ESCRT-dependent or independent pathway and starts with the inward invagination of the endosomal membrane forming the early sorting endosome. The latter undergoes maturation into a multivesicular body containing intraluminal vesicles. The formed MVBs could either be directed to lysosomes for degradation or fuse with the plasma membrane releasing exosomes into the surrounding environment. The docking and fusion of the MVBs are controlled by SNARE proteins. MVB: multivesicular body, ILV: intraluminal vesicles. Figure inspired by (van Niel, D'Angelo, and Raposo 2018).

I.3.3 Markers of exosomes

Exosome cargoes differ from one cell type to another since they are highly affected by the pathological and physiological state of the secreting cell. However, some common cargoes have been identified that are found across all exosomes. Exosomes have a characteristic lipid bilayer with a higher

concentration of phosphatidylserine on the outer leaflet, potentially enhancing their uptake by recipient cells (Fitzner et al. 2011). Among the abundant lipids in exosomes are phospholipids, sphingomyelin, ganglioside GM3, and cholesterol (Choi et al. 2013). The lipid bilayer of exosomes encloses a variety of cargoes including proteins, small peptides, DNA, and RNA (Figure 5). Since exosome biogenesis is dependent on the ESCRT proteins, these proteins, along with the accessory proteins such as TSG101, ALIX, HSP70, and HSP90, are commonly found in all exosomes (Théry et al. 2001). Exosomes are also enriched in membrane-associated proteins known as tetraspanins. These are transmembrane proteins that span the membrane four times and are present on nearly all exosomes making them the most dependable exosome markers. The tetraspanins family includes CD63, CD81, and CD9 (Figure 5), which are often used to visualize the release of exosomes from MVBs in real-time (Verweij et al. 2018). The tetraspanins are usually more abundant in exosomes compared to the cell lysate. Exosomes are also enriched in integrins, flotillin, cytoskeletal proteins, and annexins. All mentioned proteins are used to identify the isolated vesicles as exosomes (Deng and Miller 2019).

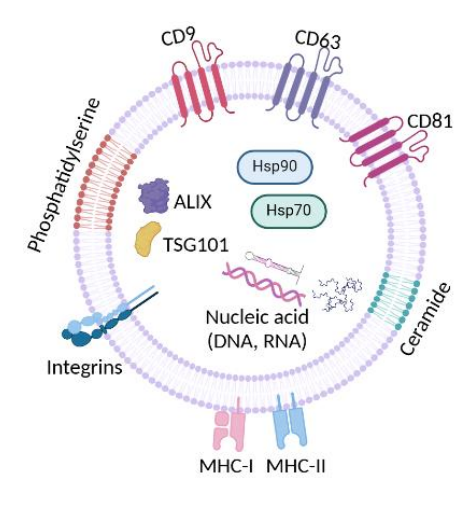


Figure 5: Exosome markers.

Exosomes are characterized by having a lipid bilayer enriched in phosphatidyl serine and ceramides. They contain several transmembrane proteins that belong to the family of tetraspanins such as CD63, CD81, and CD9, as well as integral membrane proteins. Their lipid bilayer engulfs several soluble proteins that are important for the biogenesis of exosomes such as ALIX and TSG101, and nucleic acid that could aid in the function of exosomes. Figure inspired by (Kalluri and LeBleu 2020).

I.3.4 Immune cell derived exosomes

The study of exosomes derived from immune cells began to gain significant attention in the late 1990s and early 2000s. The pioneering research in this field starts with the work of Raposo et al. (1996) which demonstrated that B lymphocytes release exosomes carrying MHC II molecules that can induce antigen-specific T-cell responses. Simultaneously, exosomes derived from DCs can activate CD8⁺ T cells and this activation is more efficient when the exosomes are derived from mature DCs in comparison to immature ones even though immature DCs secrete more exosomes than do mature DCs (Admyre

et al. 2006). This immunogenic effect was also observed in vivo where the injection of mice having tumors with DC-derived exosomes bearing tumor peptide in complex with MHC class I resulted in tumor rejection (Zitvogel et al. 1998). Consistent with earlier findings, exosomes containing dsDNA or viral RNA can initiate immune responses. Even though exosomes can travel between cells over long distances, the IS formed between CD8⁺ cytotoxic T cells and infected or tumor cells (Peters et al. 1989), as well as between T cells and APCs (Mittelbrunn and Sánchez-Madrid 2012), offers a specialized platform for the effective transfer of exosomes. As these synapses form, intercellular compartments containing vesicles are directed toward the target cells, ensuring that exosome release is confined to the synaptic cleft. This targeted transfer mechanism enhances the efficiency and specificity of EVmediated communication. For instance, when T cells interact with DCs, they release exosomes that carry genomic and mitochondrial DNA back to the DCs. This interaction enhances antiviral responses resulting in the amplification of the activity of APCs, preparing them to respond more effectively upon re-exposure to identical or closely related pathogens (Torralba et al. 2018). Contrary to their role in activating other immune cells, exosomes derived from regulatory T cells (Tregs) express CD73 that further contributes to the immunosuppressive activity of Tregs (Smyth et al. 2013). Additionally, Tregsderived exosomes carry miRNA that induces increased secretion of IL-10 by DCs which may have a role in preventing autoimmunity. Very interestingly, several studies have focused on the role of exosomes in graft rejection. Studies have demonstrated that transplanted grafts carry exosomes containing the donor's foreign antigens that migrate to the recipient's secondary lymphoid organs and trigger an immune rejection (Prunevieille et al. 2021; Liu et al. 2016; Morelli, Bracamonte-Baran, and Burlingham 2017). In addition to their importance in modulating the immune response, several clinical studies have investigated the role of exosomes in antitumoral therapy. Notably, a study involving non-small cell lung cancer patients revealed a systemic immune response rather than antigen-specific immunity when using DC-derived exosomes pulsed with various tumor peptides, resulting in increased natural killer (NK) cell lytic activity (Morse et al. 2005). Additionally, in 2008, advanced colorectal cancer patients received treatment with ascites-derived exosomes, either alone or in combination with granulocyte-macrophage colony-stimulating factor (GM-CSF). The combination therapy elicited a tumor antigen-specific cytotoxic T-cell response in two patients, with both DC-derived exosome therapies considered safe and well-tolerated. Similarly, NK cells-derived exosomes contain cytotoxic proteins such as Prf and GzmB and have antitumor effects against hepatocellular carcinoma (HCC), neuroblastoma, and pancreatic cancer (Kim et al. 2022; Neviani et al. 2019).

I.4 Rationale and aims of the project

Exosomes are diverse, heterogeneous nanoparticles involved in a variety of biological processes, with their function and cargo depending on the status and type of the cell of origin. Exosomes are released by virtually all cell types under both physiological conditions and stress. They are contained within multivesicular bodies (MVBs) and are secreted upon MVB fusion with the plasma membrane. In CD8⁺ cytotoxic T lymphocytes (CTLs), two distinct organelles—MVBs and multicore granules (MCGs) have been found to contain exosomes, prompting interest in characterizing these CTL-derived exosomes. Therefore, this study aims to investigate the differences between exosomes derived from MVBs and MCGs. Specifically, this study seeks to determine whether exosome release occurs in a coordinated, organelle-specific manner at the immune synapse or whether their release is more general throughout the cell. We aim to characterize the fusion dynamics of MVBs and MCGs and determine if they differ from that of SCG (single core granules). This will involve examining the role of SNARE proteins and tetraspanins in MVB and MCG exosome populations, as well as testing if their fusion is dependent on MUNC13-4, a key priming factor for lytic granule fusion in CTLs. Furthermore, we aim to classify exosomes into subpopulations based on surface markers (CD81, CD63) and assess their cytotoxic potential, evaluating whether CTLs utilize exosomes as an additional mechanism to induce target cell apoptosis. Ultimately, this research aims to shed light on the functional heterogeneity of CTL-derived exosomes and their potential role in immune responses.

II. Materials and methods

II.1 Materials

II.1.1 Chemicals

Product	Company	Catalogue
		number
Acryloyl-X	Thermo Fisher Scientific	A-20770
Agarose	Carl Roth	5210.3
AIM V [™] Medium, liquid	Gibco	12055-091
Ammonium chloride (NH ₄ Cl)	Merck Millipore	12125-02-9
Bovine serum albumin (BSA)	Sigma-Aldrich	A4503
Calcium chloride (CaCl ₂)	Merck Millipore	10043-52-4
cOmplete Mini, EDTA- free Protease Inhibitor Cockta	Merck Millipore	11836170001
il Tablets		
Coomassie Brilliant Blue G250	Serva	17524.01
Deoxycholate	Merck Millipore	83-44-3
Dimethyl sulfoxide (DMSO)	Sigma-Aldrich	D8418
Dithiothreitol (DTT)	Merck Millipore	3483-12-3
Dulbecco's Phosphate Buffered Saline (DPBS)	Thermo Fisher Scientific	14190014
E64 Protease Inhibitor	Merck Millipore	E3132
Ethanol (99%)	Carl Roth	5054.1
Ethidium bromide (EtBr)	Carl Roth	2218.2
Ethylenediamine tetra acetic acid disodium salt	Sigma-Aldrich	E6635
(EDTA)		
GeneRuler 1kb DNA Ladder	Thermo Fisher Scientific	SM0311
$Gibco^TM$ $Opti\text{-}MEM^TM$ I Reduced Serum Medium,	Gibco	12559099
GlutaMAX [™] Supplement		
Glucose	Merck Millipore	1.08342.1000
Glutamax	Thermo Fisher Scientific	35050061
Glycine	Carl Roth	56406
HEPES	Thermo Fisher Scientific	15630080
HPLC water	Thermo Fisher Scientific	11307090
Hydrochloric acid (HCl)	Merck Millipore	H9892
Isopropanol	Roth	AE73.1
Kanamycin	Sigma-Aldrich	K-1377

L-Glutamine 200 mM	Gibco	25030-024	
Magnesium chloride (MgCl ₂)	Merck Millipore	M1028	
Methanol	Roth	HN41.1	
MilliporeSigma TM Calbiochem TM Mowiol TM 4-88	Thermo Fisher Scientific	475904	
Reagent			
Mouse recombinant interleukin-2 (II-2)	Thermo Fisher Scientific	10662264	
N,N,N',N'-tetramethylene-1,2-diamine (TEMED)	Merck Millipore	T9281	
N,N-methylene bisacrylamide (DMAA)	Merck Millipore	274135	
NHS-ester fluorescein	Thermo Fisher Scientific 46410		
NuPAGE LDS Sample Buffer 4x	Thermo Fisher Scientific	NP0007	
NuPAGE MOPS SDS Running Buffer 20x	Thermo Fisher Scientific	NP0001	
NuPAGE Transfer Buffer 20x	Thermo Fisher Scientific	NP00061	
Oxoid™ Skimmed Milk Powder	Thermo Fisher Scientific	LP0033B	
PAGE ruler Prestained Protein Ladder	Thermo Fisher Scientific	26616	
Paraformaldehyde (PFA)	Merck Millipore	158127	
Pefabloc SC	Merck Millipore	76307	
Penicillin/Streptomycin (10000 U/mL, 10 mg/mL)	Gibco	15140122	
Pepstatin A	Merck Millipore	10253286001	
pfu-Polymerase	Fermentas	EP0501	
Phusion High-Fidelity DNA polymerase	Thermo Fisher Scientific	F530L	
Pierce 660 nm protein assay	Thermo Fisher Scientific	22660	
Poly-L-Ornithine	Merck Millipore	P4957	
Ponceau S Solution 0.1%	Sigma-Aldrich	P7170	
Potassium bicarbonate (KHCO₃)	Merck Millipore	298-14-6	
Potassium chloride	Merck Millipore	1049360500	
Potassium persulfate (KPS)	Merck Millipore	216224	
Quick Start Bradford Protein Assay	Bio-Rad	5000202	
Restore Western Blot Stripping Buffer	Thermo Fisher Scientific	21059	
RPMI 1640 medium	Gibco	21875-034	
Sigma H ₂ O	Sigma-Aldrich	W4502-1l	
Sodium acrylate	Merck Millipore	408220	
Sodium bicarbonate (NaHCO ₃)	Merck Millipore	144-55-8	
Sodium chloride (NaCl)	Merck Millipore	1064040500	
Sodium dodecyl sulfate	Carl Roth	2326.2	

- 1 1 1 1 1 1 1 1 1 1 1 1 1 1 1 1 1 1 1		
Sodium hydroxide (NaOH)	Merck Millipore	1310-73-2
Sodium Pyruvate	Thermo Fisher Scientific	11530396
Spectra Multicolor Broad Range Protein Ladder	Thermo Fisher Scientific	26634
Sucrose	Merck Millipore	573113
Super Signal West Dura Extended Duration Substrate	Thermo Fisher Scientific	34075
Thermo Fisher Scientific	Thermo Fisher Scientific	A4736401
Tris	Carl Roth	5429.1
Tris-hydrochloride	Carl Roth	9090.3
Triton X-100	Sigma-Aldrich	T8787
Trypan blue solution	Sigma-Aldrich	93595
Tryptone/Peptone	Carl Roth	8952.3
Tween 20	Carl Roth	2727.1
β -Mercaptoethanol	Carl Roth	4227.3

II.1.2 Commercial kits

Kit	Company	Catalogue
		number
Dynabeads [™] FlowComp [™] Mouse CD8 Kit	Thermo Fisher Scientific	11462D
Dynabeads [™] Mouse T-Activator CD3/CD28	Thermo Fisher Scientific	11453D
Nucleofector kit for mouse T cells	Lonza	VPA-1006
NuPAGE™ 10% Bis-Tris Protein Gels, 1.0 mm, 10-well	Thermo Fisher Scientific	NP0301BOX
NuPAGE™ 4- 12% Bis- Tris Protein Gels, 1.0 mm, 10-	Thermo Fisher Scientific	NP0321BOX
well		
NuPAGE [™] 4- 12% Bis- Tris Protein Gels, 1.0 mm, 15-	Thermo Fisher Scientific	NP0323BOX
well		
Vybrant FAM caspase 3 and 7 assay kit	Thermo Fisher Scientific	V35118

II.1.3 Commercial Antibodies

Primary	Manufacturer	Immunogen/	Host	Dilution	Applica
Antibody anti-	(Catalogue no.)	clone			tion
α1 Na+/K+	Abcam	464.4	Mouse	1:1000	WB
ATPase	(ab7671)				
ALIX	Biolegend	3A9	Mouse	1:500	WB
	(634502)				

ARF6	Abcam	polyclonal	Rabbit	1:1000	WB
	(ab226389)				
CD3e	BD Pharmingen	145-2C11	Hamster	1:25	Glass
	(553058)				coating
CD63	Abcam	EPR21151	Rabbit	1:1000	WB
	(ab217345)			1:200	ICC
CD63	Abcam	TS63	Mouse	1:200	ICC
	(ab59479)				
CD81	Novus biologicals (NB100-	1D6	Mouse	1:200	ICC
	65805)				
CD81	Cell signaling technology	D502Q	Rabbit	1:1000	WB
	(10037)				
CD82	Proteintech	polyclonal	Rabbit	1:200	ICC
	(10248- 1- AP)				
RPS10	Abcam	EPR8545	Rabbit	1:10000	WB
	(ab151550)				
TSG101	Sigma-Aldrich	4A10	mouse	1:500	WB
	(SAB2702167)				
Actin	Santa cruz	C-4	Mouse	1:5000	WB
	(sc47778)				
α-Tubulin	Abcam	polyclonal	Rabbit	1:5000	WB
	(ab125267)				
Granzyme B-	Biolegend	GB11	Rabbit	1:200	ICC
Alexa Fluor 647	(515406)				
Granzyme B	Cell signaling technology	Total Granzyme B	Rabbit	1:5000	WB
	(4275S)				
Granzyme B	Thermo Fisher Scientific	GB11	Rabbit	1:100	ICC
	(MA1-80734)				
LBPA	Merck Millipore	6C4	Mouse	1:200	ICC
	(MABT837)				
VAMP 2	Synaptic systems	69.1	Mouse	1:200	ICC
	(104211C3)				
VAMP 7	Synaptic systems	158.2	Mouse	1:200	ICC
	(232011)				
	•				

Novus Biologicals	polyclonal	Rabbit	1:8000	WB
(2- 32232)				
Manufacturer	Immunogen	Host	Dilution	Applica
(Catalogue no.)				tion
Rockland	Mouse	Goat	1:50	ICC
(810-1102)				
Abberior	Mouse	Goat	1:500	ICC
(ST635P-1001)				
Thermo Fisher Scientific	Rabbit	Goat	1:500	ICC
(10534804)				
Thermo Fisher Scientific	Rabbit IgG (H+L)	Goat	1:1000	ICC
(A11034)				
Thermo Fisher Scientific	Mouse IgG (H+L)	Goat	1:1000	ICC
(A-11029)				
Thermo Fisher Scientific	Mouse IgG (H+L)	Goat	1:1000	ICC
(A21235)				
Thermo Fisher Scientific	Rabbit IgG (H+L)	Goat	1:1000	ICC
(A21245)				
Thermo Fisher Scientific	Rabbit IgG (H+L)	Goat	1:1000	ICC
(A11011)				
Sigma Aldrich	Rabbit IgG (H+L)	Goat	1:1000	WB
(AP307P)				
Thermo Fisher Scientific	Mouse IgG (H+L)	Goat	1:1000	WB
(32430)				
	2- 32232) Manufacturer Catalogue no.) Rockland 810-1102) Abberior ST635P-1001) Thermo Fisher Scientific 10534804) Thermo Fisher Scientific A11034) Thermo Fisher Scientific A-11029) Thermo Fisher Scientific A21235) Thermo Fisher Scientific A21245) Thermo Fisher Scientific A11011) Sigma Aldrich AP307P) Thermo Fisher Scientific	Manufacturer Catalogue no.) Rockland Robberior Abberior Mouse ST635P-1001) Thermo Fisher Scientific Rabbit 10534804) Thermo Fisher Scientific Rabbit IgG (H+L) A11034) Thermo Fisher Scientific Mouse IgG (H+L) A-11029) Thermo Fisher Scientific Rabbit IgG (H+L) A21235) Thermo Fisher Scientific Rabbit IgG (H+L) A21245) Thermo Fisher Scientific Rabbit IgG (H+L) A11011) Sigma Aldrich AP307P) Thermo Fisher Scientific Mouse IgG (H+L) AP307P) Thermo Fisher Scientific Rabbit IgG (H+L) AP307P) Thermo Fisher Scientific Mouse IgG (H+L) AP307P) Thermo Fisher Scientific Mouse IgG (H+L) AP307P) Thermo Fisher Scientific Mouse IgG (H+L)	Manufacturer Immunogen Host Catalogue no.) Rockland Mouse Goat 810-1102) Abberior Mouse Goat ST635P-1001) Thermo Fisher Scientific Rabbit IgG (H+L) Goat A11034) Thermo Fisher Scientific Mouse IgG (H+L) Goat A-11029) Thermo Fisher Scientific Rabbit IgG (H+L) Goat A-21235) Thermo Fisher Scientific Rabbit IgG (H+L) Goat A21245) Thermo Fisher Scientific Rabbit IgG (H+L) Goat A21011) Sigma Aldrich Rabbit IgG (H+L) Goat AP307P) Thermo Fisher Scientific Mouse IgG (H+L) Goat	Manufacturer Immunogen Host Dilution Catalogue no.) Rockland Mouse Goat 1:50 810-1102) Abberior Mouse Goat 1:500 ST635P-1001) Thermo Fisher Scientific Rabbit Goat 1:500 10534804) Thermo Fisher Scientific Rabbit IgG (H+L) Goat 1:1000 A11034) Thermo Fisher Scientific Mouse IgG (H+L) Goat 1:1000 A-11029) Thermo Fisher Scientific Rabbit IgG (H+L) Goat 1:1000 A21235) Thermo Fisher Scientific Rabbit IgG (H+L) Goat 1:1000 A21245) Thermo Fisher Scientific Rabbit IgG (H+L) Goat 1:1000 A21245) Thermo Fisher Scientific Rabbit IgG (H+L) Goat 1:1000 A21011) Sigma Aldrich Rabbit IgG (H+L) Goat 1:1000 AP307P) Thermo Fisher Scientific Mouse IgG (H+L) Goat 1:1000

II.1.4 Media and Solutions

Media	Components
Erythrocyte lysis buffer (pH=7.3)	155 mM NH₄Cl
	10 mM KHCO₃
	0.13 mM EDTA
	100 ml H₂O
	pH 7.4
AIM-V	10% FCS
	50 μM β-Mercaptoethanol

Isolation buffer	0.1% BSA
	2 mM EDTA
	500 ml D-PBS
RPMI	10 mM HEPES
	50 μM β -Mercaptoethanol
	0.5% Pen/Strep
	10% FCS
Electroporation recovery medium	10% FCS
	10 mM HEPES
	1% DMSO
	1 mM sodium pyruvate
	9 ml OptiMEM-GlutaMAX
Nominal calcium extracellular buffer	3 mM MgCl ₂
	5 mM HEPES
	4.5 mM KCl
	155 mM NaCl
	osmolarity = 300-310 mOsm/l
	pH 7.4
High calcium extracellular buffer	10 mM CaCl ₂
	2 mM MgCl ₂
	140 mM NaCl
	4.5 mM KCl
	5 mM HEPES
	osmolarity = 300-310 mOsm/l
	pH 7.4
HSA/HBS buffer	137 mM NaCl
	20 mM HEPES
	6 mM D-Glucose
	5 mM KCl
	2 mM MgCl ₂
	1 mM CaCl ₂
	0.7 mM Na ₂ HPO ₄
	25x HAS
Quenching Solution	50 mM Glycine in 50 ml PBS + MgCl ₂ + CaCl ₂

Permeabilization solution	0.1% Triton-X-100 in D-PBS for cells
	0.005% Triton-X-100 in D-PBS for organelles
	0.001% Triton-X-100 in D-PBS for exosomes
Blocking solution	2% BSA-0.1%-Triton-X-100 in D-PBS for cells
	2% BSA-0.005%-Triton-X-100 in D-PBS for organelles
	2% BSA-0.001%-Triton-X-100 in D-PBS for exosomes
Lysis buffer (10 ml)	150 mM NaCl
	50 mM Tris-Cl (pH=7.5)
	1 mM Deoxycholate
	1 mM DTT
	1 mM EDTA
	250 μM PMSF
	1% Triton-X-100
	1 protease inhibitor tablet
	H_2O up to 10 ml
RIPA buffer (10 ml)	150 mM NaCl
	50 mM Tris-HCl (pH=7.5)
	1 mM EDTA
	1% Triton-X-100
	0.5% sodium deoxycholate
	0.1% SDS
	1 complete mini EDTA free protease inhibitor tablet
	H ₂ O
10X TBS	150 mM NaCl
	50 mM Tris-Cl (pH=7.5)
	1 I H₂O
1X TBS	100 ml (10X TBS)
	950 ml H₂0
0.1%-1X TBST	100 ml (10X TBS)
	1 ml Tween 20
	899 ml H₂0
5%-1X TBSTM	5 g non-fat dried milk
	100 ml 0.1% TBST

1X MOPS running buffer	50 ml (20X MOPS)
	950 ml H₂O
1X Transfer buffer	50 ml (20X Transfer buffer)
	950 ml H₂O
Disruption buffer	100 mM TRIS
	5% Triton-X-100
	1% SDS
	1 H ₂ O
	pH 8
Sodium Bicarbonate (100 mM)	8.4007 g NaCHO₃
	1 H ₂ O
	рН 8
10% PFA	1 g PFA
	10 ml sigma H₂O
	pH 7.4

II.1.5 Consumables

Product	Company
6, 12, 24, and 96-well plates	Greiner Bio-One
Syringes	Hencke Sass Wolf
BD Roundfilter 70 μm	Becton Dickinson
Amicon Ultra-15 Centrifugal Filter (100,000 NMWL)	Merck
Cell Culture Flask (150 cm²)	Faust
Cell Culture Flask (75 cm²)	Sarstedt
Cell Culture Flask (25 cm²)	Sarstedt
Cell Filter Millex-HV 0.45 μm	Merck Millipore
Coverslip (12, 13, and 25 mm)	Paul Marienfeld
Gel Blotting Papers Thickness 0.4 mm	Carl Roth
Glass Pasteur Pipette	Carl Roth
Magnetic stirrer	IKA
Microscope Slide	Carl Roth
Microscope Slide Superfrost Plus	Thermo Fisher Scientific
Sterican [®] Gr. 1, G 20 x 1 1/2"" / ø 0,90 x 40 mm	B. Braun
Sterican® Deep-Intramuscular G 20 x 2 3/4"" / ø 0,90 x 70 mm	B. Braun

Neubauer chamber	Brand GmbH
Petri Dish (35 mm, 92 mm, 150 mm)	Sarstedt
Serological Pipette (10 ml, 25 ml)	Sarstedt
Parafilm M laboratory sealing film	Merck Millipore
Pasteur Pipette (2 ml)	Brand GmbH
pH indicator paper	Carl Roth
Polypropylene Centrifuge Tube 15 and 50 ml	Greiner Bio-One
Pipette Tip (20, 200, 1000 μl)	Sarstedt
Pipette Filter Tip (10 μl, 20 μl, 200 μl, 1000 μl)	Sarstedt
Reaction Tube (0.5 ml, 1.5 ml, 2 ml)	Sarstedt
Syringe Filter 25 mm, 0.2 μm	Whatman plc
Syringe Filter Acrodisc 13 mm, 0.2 μm	Whatman plc
Syringe Filter Acrodisc 32 mm, 0.2 μm	Whatman plc
Polypropylene Centrifuge Tube (25 × 89 mm)	Beckman Coulter
Ultraclear Centrifuge Tube (14 × 95 mm)	Beckman Coulter

II.1.6 Devices

Device	Company
Axiovert 200 Microscope	Carl Zeiss
Balance BP 1215	Sartorius
Balance BP 4100S	Sartorius
Bath Incubator	Memmert
BD FACSAria™ III	BD biosciences
Centrifuge 5415 C	Eppendorf
Centrifuge 5415 D	Eppendorf
Centrifuge 5415 R Fast Cool	Eppendorf
Centrifuge 5424	Eppendorf
Centrifuge 5702 R	Eppendorf
Centrifuge 5804 R	Eppendorf
Centrifuge Heraeus Labofuge 400 R	Thermo Fisher Scientific
Centrifuge Mini 3-1810	NeoLab
Centrifuge Mini Spin Plus	Eppendorf
Centrifuge small	Eppendorf
DS-11 FX+ spectrophotometer/Fluorometer	DeNovix Inc

FluorChem M System ProteinSimple

Fridge/Freezer Liebherr
Glass Potter B. Braun

Hera Freeze Heraeus -80°C Freezer

Thermo Fisher Scientific

Heracell 150i CO₂ Incubator

Thermo Fisher Scientific

Herafreeze HFU B -80°C Freezer

Thermo Fisher Scientific

KL 1500 Light Source Schott

Master Cycler GradientEppendorfMaster Cycler PersonalEppendorf

Microforge World Precision Instruments Inc

Microwave Severin

MS2 Minishaker IKA

MSC-Advantage Hood Thermo Fisher Scientific

Nucleofector™ 2b machineLonzapeqPower300 Power SupplyPeqlabpH MeterSchott

Pipettes (2.5 μL, 10 μL, 20 μL, 200 μL, 1000 μL) Eppendorf
PowerPac300 Basic Power Supply Bio-Rad

Protran BA 83 Nitrocellulose Membrane Thermo Fisher Scientific

P-touch 2420 PC Brother Industries

RCT Basic IKA

Rotator NeoLab

Stimulated Emission Depletion Microscope (four-color STED Abberior Instruments

QuadScan)

Structured Illumination Microscope SIM Carl Zeiss

SW 32 Ti Swinging-Bucket Rotor Beckman Coulter
SW 40 Ti Swinging-Bucket Rotor Beckman Coulter

Thermocycler peqSTAR Peqlab

Ultracentrifuge Optima XPN-80 Beckman Coulter

UV-Chamber Custom-built

UV-Transilluminator Thermo Fisher Scientific

Vortex Mixer 7-2020 NeoLab

Wescor Osmometer	Kreienbaum
XCell II Blot Module	Thermo Fisher Scientific
XCell SureLock Mini-Cell Electrophoresis System	Thermo Fisher Scientific

II.1.7 Software

Software	Company
Cellpose	Cellpose
CorelDRAW X6	Alludo
FlowJo	FlowJo, LLC
Igor Pro, version 6.37	Wavemetrics
ImageJ, version 1.51u	National Institutes of Health
Imspector, version 16.3.11815-w2224	Abberior Instruments
Office 2016	Microsoft
Python Based Relational Animal Tracking (PyRAT), version 4.2	Scionics Computer Innovation
	GmbH
Scaffold Viewer, version 4.8.8	Proteome Software
SigmaPlot, version 14.5	Systat Software
SnapGene Viewer, version 4.0.4	GSL Biotech
VisiView, version 4.4.0.11	Visitron Systems
Zeiss Efficient Navigator (ZEN) 2012	Carl Zeiss

II.1.8 Companies

Abberior Instruments: Göttingen, DE. Abcam: Cambridge, UK. Alludo: Ottowa, CA. B. Braun: Melsungen, DE. Beckman Coulter: Krefeld, DE. Becton Dickinson: Heidelberg, DE. BD Biosciences: Heidelberg, DE. Biolegend: California, US. Bio-Rad: München, DE. Biozym: Hessisch Oldendorf, DE. Brand GmbH: Wertheim, DE. Brother Industries: Aichi, JP. Calbiochem: Mannheim, DE. Carl Roth: Karlsruhe, DE. Carl Zeiss: Jena, DE. Cell Signaling Technologies: Danvers, US. DeNovix Inc: Wilmington, DE. Eppendorf: Hamburg, DE. Eurofins Genomics: Ebersberg, DE. Faust: Schaffhausen, CH. Fermentas: St. Leon-Rot, DE. FlowJo: Ashland, US. Greiner Bio-One: Frickenhausen, DE. GSL Biotech: Chicago, US. Hencke Sass Wolf: Tuttlingen, DE. IKA: Staufen, DE. Kreienbaum: Langenfeld, DE. Liebherr: Kirchdorf, DE. Lonza: Basel, CH. Memmert: Schwabach, DE. Merck Millipore: Darmstadt, DE. MicroProbes for Life Science: Gaithersburg, US. Microsoft: Berlin, DE. Molecular Devices: San Jose, US. National Institutes of Health: Bethesda, US. NeoLab: Heidelberg, DE. New England Biolabs: Frankfurt/M, DE. Nikon Instruments: Amsterdam, NL. Novus Biologicals: Cambridge, UK. Panbiotech: Aidenbach, DE.

PanReac AppliChem: Darmstadt, DE. Paul Marienfeld: Lauda Königshofen, DE. Peqlab: Erlangen, DE. Photometrics: Tucson, US. ProteinSimple: San Jose, US. Proteintech: Rosemont, US. Proteome Software: Portland, US. QIAGEN: Hilden, DE. Roche: Grenzach-Wyhlen, DE. Rockland: Pennsylvania, US. Santa cruz: Heidelberg, DE. Sarstedt: Nümbrecht, DE. Sartorius: Göttingen, DE. Schott: Mainz, DE. Scionics Computer Innovation: Dresden, DE. Serva: Hedelberg, DE. Severin: Sundern, DE. Sigma Aldrich: Steinheim, DE. Synaptic Systems: Göttingen, DE. Systat Software: San Jose, US. The Jackson Laboratory: Bar Harbor, US. Thermo Fisher Scientific: Schwerte, DE. Visitron Systems: Puchheim, DE. Wavemetrics: Lake Oswego, US. Whatman plc: Buckinghamshire, UK. World Precision Instruments: Berlin, DE.

II.1.9 Plasmids

GzmB-pHuji was cloned by replacing mCherry at the C-terminus of GzmB (Chang et al. 2022) with forward primer 5'- ATG TAT ATC CAC CGG TCG CCA CCA TGG TGA GCA AGG GCG AGG AG-3' and reverse primer 5'- ATG TAT ACT AGC TAG CTT ACT TGT ACA GCT CGT CCA TGC CGC CG-3'. Its size was 4.315 kb (Figure 6A). The pmax-CD81-super ecliptic pHluorin (SEP) was generated by subcloning from pCMV-CD81-SEP into pMax with the restriction sites EcoRI and Xbal. Its size was 4.312 kb (Figure 6B). The pmax-CD63-pHuji was generated by subcloning from pCMV-CD63-pHuji into pMax with the restriction sites EcoRI and Xbal. Its size was 4.282 kb (Figure 6C). The pmax-CD63 SEP was generated by subcloning from pCMV-CD63-SEP into pMax with the restriction sites EcoRI and Xbal. Its size was 4.318 kb (Figure 6D). pCMV-CD81-SEP, pCMV-CD63-pHuji, and pCMV-CD63-SEP were a generous gift from Frederik Verweij (Centre de Psychiatrie et neurosciences, Amsterdam/Paris). The pMax-CD81-Halo was cloned by replacing the SEP in the CD81-SEP with forward primer 5'- ATA TAC CGG AAT TCC ATG GGA GTG GAG G-3' and reverse primer 5'- GAT TCG AGC TCC ACC GGT GCC GGA AAT CTC GAG CG-3'. Its size was 4.486 kb (Figure 6E). The pMax-CD63-pHuji-Halo was generated by subcloning from pCMV-CD63-SEP into pMax with forward primer 5'- ATA TAC CGG AAT TCC ATG GCG GTG GAA GGA-3' and reverse primer 5'- ATA TAG CTC TAG ACA TCA CCT CGT AGC CAC TTC TGA TAC-3', then the Halo Tag was added to the generated construct with forward primer 5'- ATA TAG CTC TAG AGG TGG GAG CGG AAG CGG C-3' and reverse primer 5'- ATA TAC GCG GAT CCT TAG CCG GAA ATC TCG AGC GTC GAC AGC CA-3'. Its size was 5.197 kb (Figure 6F). All plasmids were confirmed by sequencing with respective forward and reverse primers by Microsynth Seglab.

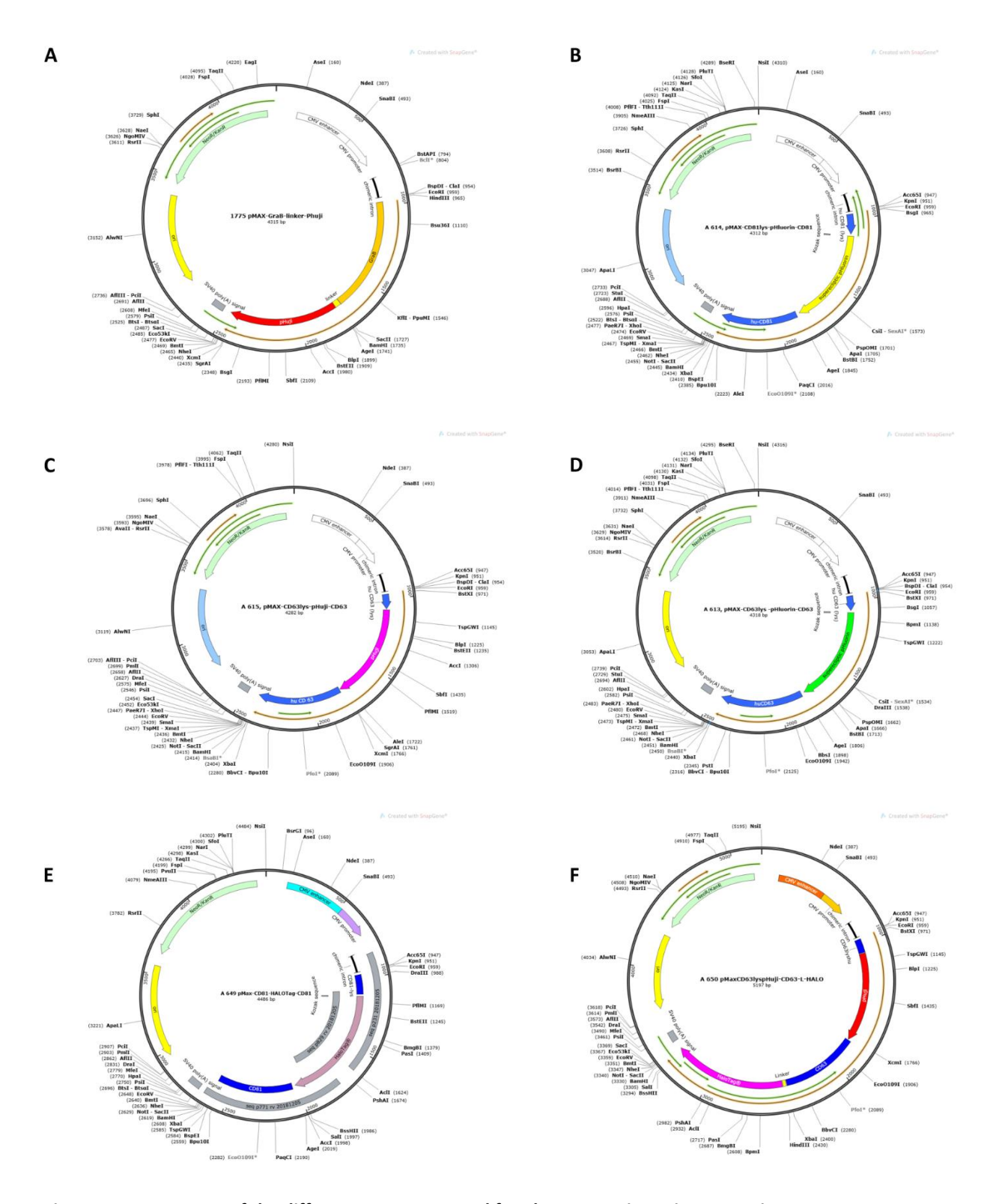


Figure 6: Vector maps of the different constructs used for electroporating primary murine CTLs.

A. pMax-Granzyme B-pHuji. B. pMax-CD81-Superecliptic pHluorin (SEP). C. pMax-CD63-pHuji. D. pMax-CD63-SEP. E. pMax-CD81-Halo. F. pMax-CD63-pHuji-Halo.

II.1.10 Mounting medium

The preparation of the mounting medium involved dissolving 6 g of glycerol and 2.4 g of Mowiol 4-88 in 6 ml of distilled water. The mixture was stirred at room temperature for 2 hours before adding 12 ml of 0.2 M Tris-HCl buffer (pH 8.5). This solution was incubated overnight at 53° C, followed by centrifugation at $1700 \times g$ for 20 minutes at room temperature. The resulting clear supernatant was aliquoted and stored at -20°C.

II.1.11 Cell Lines

P815 mastocytoma cell line (Mus musculus; Mast cells) from DSMZ no. ACC 1.

II.1.12 Mouse strains

- 1. C57BL6/N (Black 6), Stock No: 005304, The Jackson Laboratory
- 2. Munc13-4 KO mice: Mouse background C57BI/6N
- 3. GzmB-mTFP KI mice (EM:13092): Mouse background C57BL6/J

II.2 Methods

II.2.1 Animal housing

All experimental procedures were approved and conducted in compliance with the regulations set by the state of Saarland (Landesamt für Verbraucherschutz, AZ.: 2.4.1.1). Mice of both sexes were maintained at 22°C with 50-60% humidity, under a standard 12-hour light/dark cycle. They were housed under specific pathogen-free (SPF) conditions and given unrestricted access to food and water. Mice were anesthetized using CO₂ (AVMA Guidelines 2007) before being euthanized by cervical dislocation.

II.2.2 Positive isolation of CD8⁺ T lymphocytes

The spleen of 18–22-week-old C56BL6/N wild type (WT), GzmB-mTFP KI, or Munc13-4 KO mice was extracted and then smashed through a 70 μ m strainer. The filtrate was collected in fresh and warm AIM-V media containing 10% depleted FCS (dFCS). The resulting splenocyte suspension was centrifuged for 8 minutes at 300 × g. Erythrocytes were removed by treating the cells with 1 ml of erythrocyte lysis buffer. The reaction was stopped after 30 seconds by the addition of AIM-V media, followed by centrifugation at 300 × g for 8 minutes. The pellet was washed with isolation buffer and centrifuged as previously described. CD8+T lymphocytes were positively isolated from splenocytes using DynabeadsTM FlowCompTM Mouse CD8+ kit according to the manufacturer's instructions. Briefly, 5×10^7 splenocytes were resuspended in 500 μ l isolation buffer with 25 μ l anti-CD8 antibody. The cells

were kept for 10 minutes on ice. They were then washed with isolation buffer and centrifugation was performed to remove the unbound antibody. Following the washing step, CD8 $^+$ T cells were selected by the addition of 75 μ l CD8-coated beads (provided in the kit) together with 1 ml of isolation buffer and rotated for 15 minutes on a rotator at 4 $^\circ$ C. Subsequently, the suspension was placed in a magnet for 2 minutes to collect the bead-bound cells. Cells were detached from Dynabeads by adding 1 ml release buffer while keeping the falcon tube on the rotator for 10 minutes at RT. Beads were removed by exposing the suspension for 2 minutes to a magnet. Cells were washed by the addition of isolation buffer and collected after a centrifugation step of 300 x g for 8 minutes. After which cells were counted and activated.

II.2.3 Activation of naive CD8⁺ T lymphocytes

CD8⁺ T cells were cultured for 5 days in 24 well plates or T75 flasks at a density of 1×10^6 cells/ml in AIM- V medium and incubated at 37°C with 5% CO₂. For exosome isolation culture, 8 to 10×10^6 cells from each mouse were resuspended in AIM-V medium supplemented with 10% dFCS and 50 μ M beta-mercaptoethanol (β me). Cells were activated with 100 U/ml of recombinant IL-2 and anti-CD3/anti-CD28 mouse T cell activator Dynabeads at a ratio of 1:0.8. Cells were split when needed with the addition of fresh media supplemented with 10% dFCS. Cells were supplemented with 100 U/ml recombinant IL-2 every second day.

For microscopic observation of cultured cells, cells were resuspended in AIM-V medium with 10% FCS and cultured in 24 well plates in a concentration of 1×10^6 cells/ml. Cells were activated as described earlier. Cell splitting was done whenever the cells were dense. Fresh AIM-V medium with 100 U/ml recombinant IL-2 and 10% FCS was added after each splitting and day 5 cells were used for further experiments.

The depleted FCS was generated by overnight ultracentrifugation at $100,000 \times g$ at $4^{\circ}C$, the resulting supernatant was aliquoted and stored at $-20^{\circ}C$ for future usage.

II.2.4 Subset analysis of CD8⁺ T lymphocytes using flow cytometry

Flow cytometry assay was used to check the quality, activity state, and population of day 5 CD8 $^{+}$ T lymphocytes. $0.2-0.5 \times 10^{6}$ CD8 $^{+}$ T cells were resuspended in D-PBS and incubated on ice for 30 minutes in the dark with FITC-, APC-, or PE-conjugated antibodies targeting the cell surface markers CD44, CD62L, and CD25, which are markers of cell differentiation. The viable CD8 $^{+}$ T lymphocytes were gated based on their size and granularity. The gating was done in comparison to the unstained CTLs. All flow cytometry data were acquired using a BD FACSAria III analyzer (BD Biosciences) with BD FACSDiva software 6.0 and subsequently analyzed using FlowJo v10.0.7 software. (Figure 7).

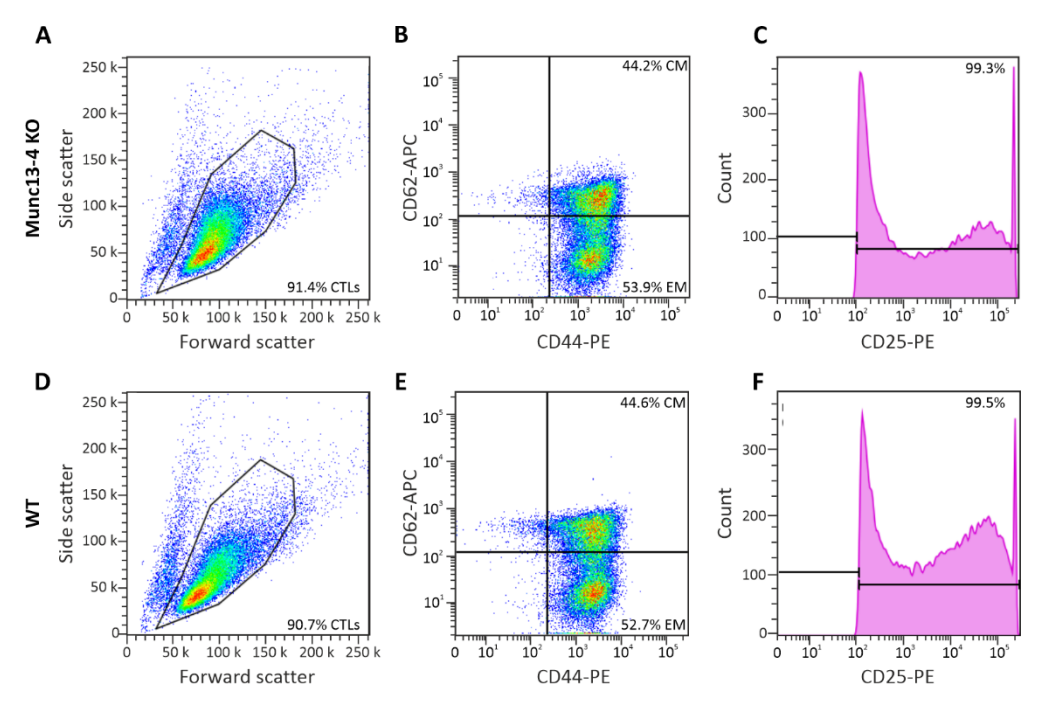


Figure 7: Flow cytometry analysis of CTL subsets in Munc13-4 KO and WT cells.

Naive CD8⁺ T cells were activated for 5 days and then stained with CD62L and CD44 to characterize the subtypes of CTLs into central memory (CM) and effector memory (EM) cells. Viable cells were gated based on forward and side scatter. Numbers in plots represent the percentage of healthy viable cells derived from Munc13-4 KO (A) or WT cells (D) in the gate. Those viable cells were plotted according to the surface markers to characterize CTL subtypes. (B) Representative flow cytometry analysis of Munc13-4 KO CTL subtypes showing that 53.9% of the detected cells are EM and 44.2% are CM. (F) WT CTLs are divided into 52.7% EM and 44.6% CM cells. The activity of the cells was determined by staining against CD25 surface marker. The results show that 99.3% (C) and 99.5% (G) of the Munc13-4 KO and WT CTLs respectively are activated. N=3, CM: central memory, EM: effector memory, CTL: cytotoxic T lymphocytes.

II.2.5 P815 cell culture

P815 cells were cultured in RPMI medium with 10% FCS and 1% Penicillin/Streptomycin. Cells were split every other day in a ratio of 1:33. Cells were used between passages 16 and 20.

II.2.6 Electroporation of CTL

During my PhD, I optimized the electroporation procedure we have been using over the years. This work consisted of developing a new recovery medium (RM) used to culture the electroporated cells directly after transfection. The reason behind this work was to become less dependent on proprietary substances from companies. After the corona crisis, Lonza stopped providing their recovery media that comes with their transfection kit (Mouse T Cell Nucleofector Kit, VPA-1006; Lonza) and they suggested RPMI medium as an alternative. However, this medium did not adequately replace their proprietary medium. Therefore, I compared the effect of different media on cell viability, transfection efficiency, and function and came up with a solution for a highly efficient transfection of primary T cells (Figure 8). Using this new recovery medium not only resulted in a significantly higher cell viability and transfection efficiency as compared to the other basic media, but more importantly, the

electroporated T cells kept their function and we could proceed with our experiments (Alawar et al. 2024).

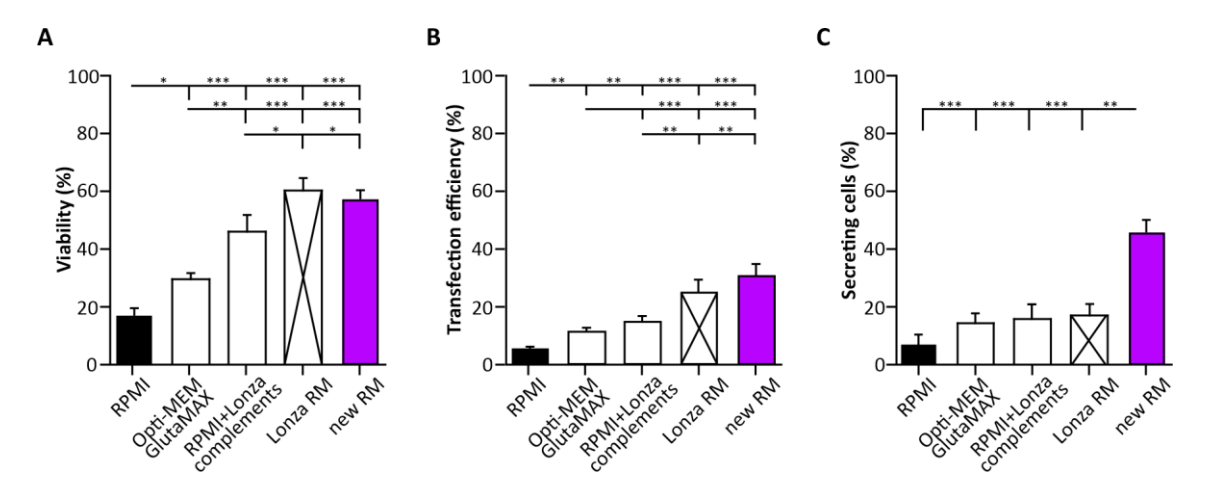


Figure 8: Effect of recovery media on cell viability, transfection efficiency, and secretion in murine CTLs. (A) Quantitative analysis of cell viability 14 hours after electroporation was performed using the specified recovery media. Viability was assessed by calculating the proportion of live cells out of the total cell population. (B) Quantitative analysis of transfection efficiency was determined as the percentage of fluorescently labeled cells among the total viable cell population. (C) Quantitative analysis of the proportion of secreting CTLs indicated the percentage of cells secreting relative to the total number of transfected cells. Data are presented as mean \pm standard error of the mean (SEM). N = 4 independent experiments, *p < 0.05, **p < 0.01, *** p < 0.001. Figure modified from (Alawar et al. 2024).

Activated day 5 murine CTLs were electroporated using the Nucleofector™ 2b Device (Lonza). Approximately 6 × 10⁶ cells were suspended in 100 μl of electroporation buffer (Mouse T Cell Nucleofector Kit, VPA-1006; Lonza) and 1.5~ 2 μg plasmid DNA of either of the following constructs: CD63-pHuji, CD63-super ecliptic pHluorin (SEP), CD81-SEP, CD81-Halo, CD63-pHuji-Halo, and granzyme B-pHuji. The mixture was transferred to electroporation cuvettes, and electroporation was performed immediately using the specialized X-001 pulse program for mouse CTLs. Transfected cells were promptly transferred to 3 ml of prewarmed recovery media and incubated in 12-well plates at 32°C with 5% CO₂. After 12 hours, the cells were washed and cultured in AIM-V supplemented with 10% FCS at 37°C. They were utilized for experiments 14-18 hours post-electroporation.

II.2.7 Anti-CD3 coated coverslips

25 mm glass coverslips (pre-cleaned with 70% ethanol) were used for antibody coating. The coverslips were coated with 30 μ l of 0.1 mg/ml poly-ornithine for 30 minutes at RT. After sucking off poly-ornithine, 30 μ l of anti-CD3 antibody (30 μ g/ml) was added to poly-ornithine coated coverslips and kept for 2 hours at 37 °C. The solution was aspirated, and the coated coverslips were ready to use.

II.2.8 Supported lipid bilayer

Glass slides were treated in Piranha solution (a mixture of 50 ml sulfuric acid and 25 ml hydrogen peroxide) for 20 minutes, followed by rinsing with freshly prepared MilliQ water for 5 minutes to prevent contamination. The slides were then air-dried at room temperature, and any residual organic contaminants were removed by plasma cleaning for 10 minutes. A microscopy chamber (Ibidi stickyslide® VI) was adhered to the cleaned glass slide.

To prepare the lipid bilayers, 33 μ l DGS-NTA (0.4 mM stock), 10 μ l Cap PE capbio (0.4 mM stock), 6.5 μ l DOPC (0.4 mM stock), and 2 μ l (for 20 μ g/ml lipid bilayers) of biotinylated anti-CD3° antibody (clone 145-2C11, 0.5 mg/ml) were added to the chamber. Next, 1000 μ l of 5% casein with 10 μ l of 100 μ M NiSO4 were added to each well and incubated for 20 minutes. Subsequently, 3 μ l of ICAM His-tag solution (1:2000 dilution from a 0.55 mg/ml stock) were introduced into each chamber. Between each preparation step, the chambers were gently washed three times with 150 μ l HBS/HSA buffer.

Before imaging, the buffer was removed from the wells, and 0.3×10^6 CTLs were resuspended in 50 μ l extracellular buffer containing nominal calcium concentration and added into each well.

II.2.9 Total Internal Reflection Fluorescence Microscopy (TIRFM)

Total Internal Reflection Fluorescence Microscopy (TIRFM) is a high-resolution technique that allows the imaging of events that occur 200 nm from the plasma membrane. Instead of the direct illumination that is found in most other microscopes, TIRFM excites fluorophores using evanescent waves. This is created when an incident laser undergoes total internal reflection at the interface between glass and water. The TIRFM setup from Visitron Systems GmbH (Puchheim, Germany) was used to capture fusion events. This setup is based on an IX83 (Olympus) equipped with the Olympus autofocus module, a UAPON100XOTIRF NA 1.49 objective (Olympus), a 488 nm 100 mW laser and a solid-state 100 mW laser emitting at 561 nm, the iLAS2 illumination control system (Roper Scientific SAS, France), the evolve- Prime95B camera (Teledyne Photometrics) and a filter cube containing Semrock (Rochester, NY, USA) FF444/520/590/Di01 dichroic and FF01-465/537/623 emission filter. The setup was controlled by Visiview software (Version: 4.0.0.11, Visitron GmbH). Day 4 WT CTLs were co-transfected with either of the following combinations: CD63-pHuji and CD81-SEP, CD63-SEP and GzmB-pHuji. GzmB-mTFP CTLs were transfected with CD63-pHuji. 14-18 hours, post electroporation, about 0.3×10^6 CTLs were resuspended in 30 μ l extracellular buffer containing nominal calcium concentration and allowed to settle on anti-CD3ɛ coated coverslips for 1 minute. Cells were perfused with an extracellular buffer containing 10 mM calcium to promote fusion. Imaging was performed at room temperature for 10 minutes using 561 nm and 488 nm lasers. The images were acquired with a 10 Hz acquisition frequency with a 100 ms exposure time.

II.2.10 TIRF Analysis

The use of pH-sensitive fluorophores such as pHuji and SEP enables us to study the single exocytosis events. Their fluorescence is quenched in acidic pH (5.5). Upon the fusion of the organelle with the plasma membrane, a neutralization of the pH to 7.4 results in the unquenching of the pH-sensitive fluorophore which leads to a sudden increase in the fluorescence. This increase in fluorescence is considered an indicator of the fusion event. Fusion events were analyzed using ImageJ software with the Time Series Analyzer plugin. Fusion was defined as a fluorescence change occurring within 200 ms.

II.2.11 Immunostaining CD8⁺ T lymphocytes

Cells were allowed to settle on anti-CD3ɛ coated coverslips for 10 minutes at room temperature and fixed with 4% paraformaldehyde (PFA) for 20 minutes under a chemical hood. The fixed cells were then washed three times with D-PBS for 5 minutes each and then permeabilized with 2% BSA-0.1% Triton-X-100 solution for 30 minutes. The permeabilizing solution was removed and the cells were blocked for 30 minutes with 2% BSA in D-PBS. After blocking, primary antibodies were added for 1 hour and then washed away with the permeabilizing solution. The secondary antibodies were added for 45 minutes and cells were kept in the dark. Excess antibody was washed away three times with D-PBS. The coverslips were then dipped in distilled water and immediately mounted. All steps were performed at room temperature.

II.2.12 Gelatin coated coverslips

12 mm glass coverslips (pre-cleaned with 70% ethanol) were used for gelatin coating. 2% gelatin was prepared by dissolving gelatin powder in warm distilled water. After sterile filtration of the solution, $10 \,\mu l$ of the 2% gelatin was added to each coverslip. The coverslips were completely covered with a thin layer of gelatin. The coverslips were dried under a sterile hood and further sterilized for 30 minutes under direct UV exposure. Then they were stored at 4°C for later usage.

II.2.13 Organelle isolation

II.2.13.1 Cell homogenization

 $0.8-1.5 \times 10^8$ day 5 CD8⁺ T cells were collected and washed once in an ice-cold isolation buffer. The cells were then centrifuged at $300 \times g$ for 6 minutes and the resulting pellet was resuspended in a 2 ml homogenization buffer (see materials). The cell suspension was transferred into a clean and prechilled cavitation bomb (4°C) and a micromagnetic stir bar was added. The Parr Bomb was closed and placed on a magnetic stirrer and connected to the nitrogen tank. The pressure was slowly pressurized to 800 psi with nitrogen gas and the mixture was stirred at 4°C for 25 minutes. The pressure was slowly

released, and the homogenate was collected in a pre-chilled 15 ml tube. The cell lysate was then centrifuged for 10 minutes at $1000 \times g$ at $4^{\circ}C$ to pellet unbroken cells, partially lysed cells, and nuclei. The post nuclear supernatant (PNS, S1) was collected, avoiding any foam (Figure 9). The pellet/foam was washed once with 0.5 ml of homogenization buffer and centrifuged again at $1000 \times g$ for 10 minutes at $4^{\circ}C$. The resulting 0.5 ml supernatant was added to the PNS from the previous step (~2 ml total volume) and the pooled supernatant was used for subcellular fractionation (Schirra et al. 2023).

II.2.13.2 Subcellular fractionation

Sucrose solutions of the following concentrations (0.3, 0.5, 0.8, 1.0, 1.2, 1.4, and 1.6 M) were prepared from a 2 M sucrose stock solution in a sucrose solubilization buffer supplemented with fresh proteinase inhibitors. The density of sucrose was confirmed by measuring the refractive index for each solution using a refractometer. A discontinuous sucrose gradient column was built in a pre-chilled 14 ml ultra-clear centrifuge tube by gently layering 1−2 ml of each sucrose solution from bottom to top. At the end, around 2 ml of the pooled PNS (0.3 M sucrose) was layered onto the performed gradient. The gradient was then ultracentrifuged at 100,000 × g for 90 minutes at 4°C using the SW40Ti rotor with acceleration/deceleration of 8. The gradient was divided into 12 fractions of 1 ml volume each (Figure 9). Starting from the top layer, each 1 ml was gently collected from the top of the gradient and transferred into 1.5 ml protein low-binding tubes, ensuring the layers remained unmixed during the process. The aliquots were kept on ice and fresh proteinase inhibitors were added again to avoid protein degradation. Protein concentrations in each fraction were measured using the Pierce™ 660 nm Protein Assay reagent.

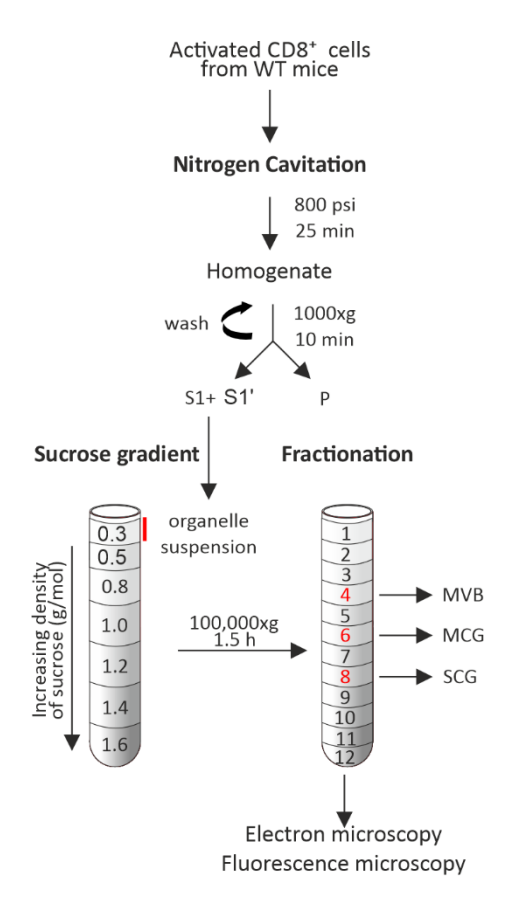


Figure 9: Schematic representation of the organelle isolation procedure from murine CTLs modified from Schirra et al. (2023).

II.2.13.3 Immunostaining of isolated organelles

Isolated organelles in the sucrose fractions were fixed with 0.2% PFA on ice for 10 minutes. They were then diluted with 320 mM KCl and added on 2% gelatin-coated coverslips fixed on an adaptor in the ultracentrifuge tubes. The fixed organelles were ultracentrifuged on the coverslips for 30 minutes at 10,000 × g following an additional fixation with 2% PFA for 5 minutes. The samples were washed 3 times with D-PBS for 4 minutes each and quenched with 50 mM glycine for 2 minutes. They were permeabilized with 0.005% Triton-X-100 solution for 5 minutes and blocked twice for 4 minutes each with 2% BSA in D-PBS. After blocking, the primary antibody, which was diluted in the blocking solution to its working concentration (see II.1.3), was added for 30 minutes at room temperature. Samples were washed twice with the blocking solution for 4 minutes each and the secondary antibody was added for 30 minutes. The samples were washed twice with a permeabilizing solution for 4 minutes each, followed by additional two washing steps for 4 minutes each with D-PBS. The coverslips were then dipped in distilled water and directly mounted on cover slides. The samples were then stored at 4°C for imaging using SIM.

In co-staining experiments using antibodies raised in the same species, the staining was performed consecutively with the use of Fab fragments in between.

II.2.13.4 Western blot of the isolated organelles

Sucrose fractions were separated by SDS-PAGE using precast 10% Bis-Tris gels with MES running buffer or 4–12% gradient Bis-Tris gels with MOPS running buffer. Proteins were transferred to 0.2 μ m pore-size nitrocellulose membranes and blocked for 2 hours at 20 ± 2°C with 5% non-fat dry milk powder in TBS buffer containing 0.05% Tween 20, pH (7.4). For quantitative western blotting, protein concentrations in the sucrose fractions were determined using PierceTM 660 nm Protein Assay reagent. The immunoblots were probed with anti-alpha tubulin, anti-synaptobrevin 2, anti-synaptobrevin 7, anti-granzyme B, anti-EEA1, anti-TSG101, followed by horseradish peroxidase (HRP)-conjugated goat anti-mouse (H + L) or anti-rabbit secondary antibodies (heavy and light chain). Finally, the blots were developed using SuperSignal West Dura Chemiluminescent Substrate and visualized using the FluorChem M system (ProteinSimple).

II.2.14 Exosome isolation

Exosome isolation was performed on day 5 effector CD8+ T lymphocytes following a differential ultracentrifugation protocol. Briefly, the supernatant of 600–800 × 10⁶ CD8⁺ T lymphocytes generated from one mouse was collected as explained previously. Anti-CD3/anti-CD28 activator beads were removed from ~240 ml supernatant and a mini-EDTA-free tablet was added (in a ratio of 1 tablet for 50 ml supernatant). The supernatant was centrifuged for 10 minutes at 1000 x g to pellet the CTL (pellet 1, P1). Cell-free supernatant was then transferred to 50 ml falcon tubes and centrifuged for 20 minutes at 2000 × g to remove further cell debris (P2). To collect the larger extracellular vesicles such as microvesicles (P3), the remaining supernatant was added into clean (UV treated for 20 minutes) 38 ml ultra clear thick wall tubes and ultracentrifuged using SW32 rotor for 40 minutes at 10,000 × g. The resulting supernatant was collected again in 38 ml tubes and ultracentrifuged for 75 minutes at 100,000 × g to collect the smaller extracellular vesicles such as exosomes (P4). A final washing step was done by dissolving all P4 pellets from the different tubes in D-PBS and collecting them into one clean 14 ml UltraClear tube. A cocktail of protease inhibitors (Pefabloc, E64, Pepstatin A) was added and ultracentrifugation was done using SW40 rotor for 75 minutes. All centrifugation steps were performed at 4°C. The exosome pellet was resuspended in 50 µl D-PBS for further purification with sucrose density gradient (Figure 10).

II.2.14.1 Sucrose density centrifugation

To further purify the isolated exosomes, the P4 sample from day 5 CTLs was added on a sucrose density gradient. A 2 M sucrose stock was prepared by dissolving sucrose in HEPES buffer (pH 7.3), and the following dilutions were done (0.3, 0.6, 0.95, 1.1, 1.2, 1.3, and 1.6 M). A protease inhibitor mixture consisting of 3 mM Pefabloc, 10 μ M E64, and 10 μ g Pepstatin A was added to these solutions (these inhibitors were not added if the exosomes were to be used for killing assays). The discontinuous sucrose density gradient column was carefully constructed from bottom to top in a 14 ml Ultraclear tube by sequentially layering 1 or 2 ml of each sucrose solution. This step was done by adding the higher-concentration sucrose solution first and then carefully dropping the sucrose solution of lower concentration using a syringe with a small needle on top of it. The exosome pellet obtained after differential ultracentrifugation was mixed with the 0.3 M sucrose and carefully added to the gradient. Ultracentrifugation was done using SW40 rotor at $100,000 \times g/4$ °C overnight (Figure 10). Sucrose fractions were then collected and diluted in D-PBS and ultracentrifuged for further 75 minutes at $100,000 \times g$. All centrifugation steps were performed at 4°C. The exosome pellet was then resuspended in \sim 50-80 μ L D-PBS and used directly or stored at 4°C for a maximum of 24 hours for further analysis.

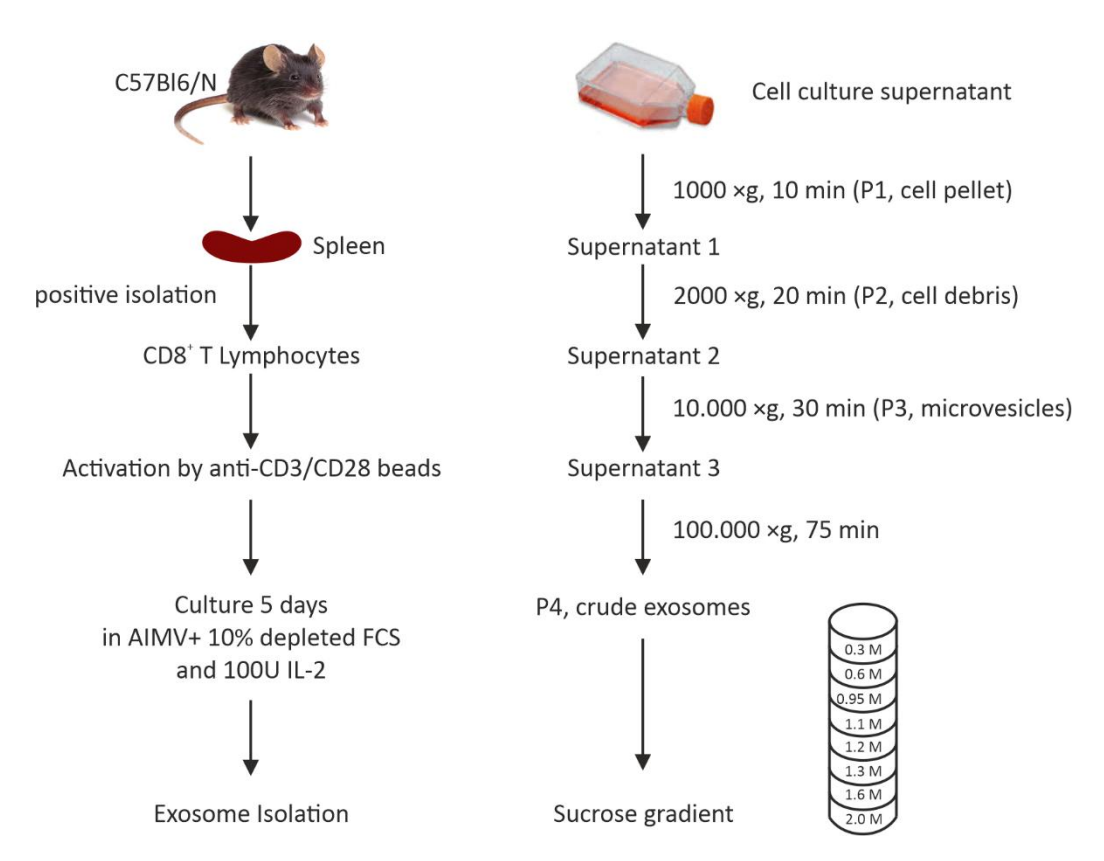


Figure 10: Schematic representation of exosome cell culture and isolation procedure from primary murine CTLs.

II.2.14.2 Preparing protein lysates of different samples

The whole brain was isolated from 10 weeks old mouse and homogenized in protein lysis buffer. The homogenate was rotated in the cold room (4°C) for 30 minutes and then centrifuged for 10 minutes at $1000 \times g$. About 10×10^6 CTLs were lysed in RIPA buffer ($100 \mu l$ to 10^7 cells), the homogenate was kept on ice for 30 minutes then centrifuged for 10 minutes at $1000 \times g$. The supernatant was collected, aliquoted, and stored at -80° C after measuring the protein concentration using PierceTM 660 nm Protein Assay reagent. To prepare protein lysates of different fractions of the sucrose gradient or the exosome pellet, $10 \mu l$ from each of the samples were lysed with an equal amount of RIPA buffer and directly used for western blot.

II.2.14.3 Western Blot for cells and exosomes

Western Blot analysis was performed to check the expression of different proteins. For that, 10 μg of the isolated protein lysates were mixed with 4X LDS buffer for a final concentration of 1X. For reducing conditions, \(\beta me \) was added to the LDS buffer in a 10% ratio and it was excluded from non-reducing conditions. Water was added for a final sample volume of 35 µl when using a 10-well polyacrylamide gel or 25 µl for 15-well gels. Prior to loading, the samples were boiled for 5 minutes at 95°C. Samples were loaded into the slots of a 4-12 % Bis-Tris polyacrylamide gel and the gels were run for 90 minutes at 165 V. After running, the gels were blotted onto 0.45 µm nitrocellulose membrane overnight at 30 mA at 4°C. To check the quality of the transfer, the membrane was incubated for 1 minute with Ponceau S stain and then washed 3 times for 5 minutes each with TBST to remove the remaining Ponceau stain. The membrane was then blocked for 1 hour (three times washing, 20 minutes each) with 5% milk in TBST at room temperature. Afterwards, the membranes were incubated with the primary antibodies for 2 hours at room temperature and washed three times for 20 minutes each with 5% TBST-M before adding the species-specific secondary antibodies coupled to HRP for 1 hour at room temperature. The blot was then washed three times with TBST for 15 minutes each and two times with TBS for 10 minutes each. For chemiluminescent detection of proteins, the blots were developed using SuperSignal West Dura Chemiluminescent Substrate and visualized using the FluorChem M system (ProteinSimple).

II.2.14.4 Coverslip ultracentrifugation

To be able to directly stain and characterize the isolated exosomes, a new approach was developed. This method consists of pelleting the exosomes on gelatin coated coverslips by ultracentrifugation. To do so, the 2% gelatin coated coverslip was glued using silicon on an adaptor (Figure 11), which can be inserted into a 14 ml ultra clear ultracentrifuge tube. The exosomes were diluted in ~14 ml D-PBS and

added on top of the coverslip. The tube was then ultracentrifuged using SW40 rotor for 4 hours at $20,000 \times g$ at 4°C. The exosomes were then directly fixed and prepared for immunostaining.

II.2.14.5 Immunostaining of isolated exosomes

Exosomes were fixed in 2% PFA for 5 minutes at room temperature. The fixing solution was then removed, and exosomes were washed once with D-PBS. The sample was quenched with 2 mM glycine solution for 5 minutes at room temperature. After three washing steps of 5 minutes each, exosomes were permeabilized using 0.001% Triton-X-100 solution in D-PBS for only 5 minutes. The permeabilization solution was removed and the sample was then blocked for 10 minutes using 2% BSA in D-PBS. After that, the primary antibody was diluted to its working concentration (II.1.3) in blocking solution and added on top of the coverslip for 30 minutes at room temperature. The sample was then washed with the blocking solution twice for 5 minutes each and the secondary antibody was added for 30 minutes at room temperature. After removing the secondary antibody, the sample was washed three times with D-PBS and the coverslip was dipped into distilled water and mounted using mounting medium on top of a cover slide. The samples were stored at 4°C for imaging using SIM or Expansion Microscopy (Figure 11).

II.2.15 Structured illumination microscopy (SIM)

Structured Illumination Microscopy (SIM) is an advanced super-resolution imaging method that leverages patterned light to improve spatial resolution. By illuminating samples with striped light patterns, the technique captures fluorescence emissions at various rotational orientations. The interaction between the striped excitation light and the sample's diffraction generates Moiré patterns, which encode high-frequency spatial details. These patterns are subsequently analyzed using dedicated algorithms, enabling the reconstruction of multiple captured images into a final composite with lateral resolutions ranging from 100 to 130 nm. The SIM setup used was a Zeiss Elyra PS1 (Zeiss, Oberkochen), equipped with solid-state lasers emitting at wavelengths of 405 nm, 488 nm, 561 nm, and 642 nm. After immunostaining, images were captured using a 63× Plan-Apochromat (NA 1.4) objective with laser excitations at 488, 561, and 642 nm to excite the samples. Z-stacks were acquired with a typical step size of 150 nm. The raw images were processed to enhance resolution using Zen software (Zen 2012; Carl Zeiss), and additional analysis was performed using ImageJ v1.46 software.

For correlative light and electron microscopy (CLEM), images of ultrathin sections of post-embedded GzmB-mTFP KI mouse CTLs expressing CD81-Halo or CD63-pHuji-Halo and stained with SiR were acquired using excitation light at wavelengths of 405, 488, and 642 nm. Using a 63× Plan-Apochromat

objective (NA 1.4) in SIM mode, nearly the entire field of view of a 200-mesh grid (approximately 90 μ m²) was captured, allowing for precise orientation relative to the grid bars. DAPI images with a wavelength of 405 nm were recorded to identify the nuclei of the CTLs and the exact image plane. Following the adjustment of the highest and lowest focal planes for z-stack analysis, 3 to 10 images were captured with 405, 488, and 642 nm wavelengths with a 100 nm step size to scan the cells of interest. The images were further processed to obtain higher resolutions by Zen 2011 (Zeiss).

II.2.16 Colocalization analysis of organelles and exosomes

Single-plane images acquired using SIM microscopy for isolated organelles or exosomes were segmented using Cellpose 2.0 (Pachitariu and Stringer, 2022). Prior to segmentation, an ImageJ macro was used to subtract the background, change image color into a 'fire' look up, and save the images as RGB. The resulting images were loaded to Cellpose 2.0 where the "cyto" model was used to segment the images. Later, each image was manually checked for suitable adjustments and corrections. The segmented images were saved and subsequently used in an in-house written Matlab (MathWorks, written by A.Chouaib) program classifying the overlapping objects according to their staining.

II.2.17 Electron Microscopy.

To localize the different proteins to the CTL organelles, correlative light-electron microscopy (CLEM) analysis of cryo-fixed mouse CTLs was done as described previously (Matti et al. 2013). Day 4 CTLs isolated from GzmB-KI mice were transfected with CD63-pHuji-Halo or CD81-Halo constructs. 12 hours post electroporation, cells were stained with silicon rhodamine for 1 hour at 37°C. Cells were then washed three times with AIM-V medium after which 4×10^3 CTLs were seeded on 0.1 mg/ml poly-Lornithine and 30 µg/ml anti-CD3ɛ coated 1.4 mm sapphire discs in flat specimen carriers (Leica) for 10 minutes at 37°C with 5% CO₂ to allow the formation of an immunological synapse. Cells were then vitrified using a high-pressure freezing system (EM PACT2, Leica) in AIM-V medium containing 30% FCS and 10 mM HEPES. The carriers containing frozen cells were then cryo-transferred into the precooled (-130°C) freeze-substitution chamber of the AFS2 (Leica). The temperature was increased gradually, over 2 hours, from -130 to -90°C. Cryo-substitution occurred at -90 to -70°C for 20 hours in anhydrous acetone, followed by substitution at -70 to -60°C for 24 hours with 0.3% (w/v) uranyl acetate in anhydrous acetone. At -60°C, the samples were infiltrated with increasing concentrations of Lowicryl (3:1 K11M/HM20 mixture) for 1 hour each at 30%, 60%, and 100%. After 5 hours of infiltration with 100% Lowicryl, samples were UV polymerized for 24 hours at -60°C, followed by an additional 15 hours with a gradual temperature increase to 5°C. The samples were kept at 4°C in the dark until further processing. The membrane carriers were removed, and ultrathin 100 nm sections

were cut using an EM UC7 (Leica) and collected on carbon-coated 200 mesh copper grids (Plano). Fluorescence analysis of the EM grids was performed within 24 hours post-sectioning to prevent the loss of fluorescence signals. The grids were stained with DAPI (1:1000) for 3 minutes, washed, and sealed between two coverslips with silicone (Picodent Twinsil®) for high-resolution SIM imaging. After fluorescence imaging, the grids were stained with uranyl acetate and lead citrate and recorded using the Tecnai12 Biotwin electron microscope. Only CTLs with well-preserved membranes, organelles, and nuclei were analyzed for correlation. For the correlation, the DAPI 405 nm image showing the labeled nucleus was used to align with the electron microscope image. The final alignment defined the position of the fluorescent signals within the cell of interest. Images were overlaid using Corel DRAW X6.

To compare Munc13-4 KO and WT CTLs, cells were vitrified after 30 minutes, 1 hour, and 4 hours of incubation at 37°C with 5% CO₂ on 1.4 mm sapphire discs coated with 0.1 mg/ml poly-L-ornithine and 30 μg/ml anti-CD3ε in flat specimen carriers. Freeze substitution and Epon embedding were carried out as previously described (Liu et al., 2010). Briefly, all samples were transferred into a pre-cooled (-130°C) freeze-substitution chamber (AFS2; Leica), where the temperature was gradually increased from -130°C to -90°C over 2 hours. Freeze substitution was performed with 2% osmium tetroxide in anhydrous acetone and 2% water. The temperature was then raised linearly from -90°C to -70°C over 20 hours, from -70°C to -50°C over another 20 hours, and from -50°C to -10°C over 5 hours. After washing with anhydrous acetone, the samples were embedded in Epon-812 using a series of steps: 30% Epon/acetone for 15 minutes at -10°C, 70% Epon/acetone for 1 hour at -10°C, and pure Epon for 1 hour at 20°C (Electron Microscopy Sciences). The temperature was then gradually increased from 20°C to 60°C over 4 hours, and Epon polymerization was carried out at 60°C for 24 hours. After polymerization, the membrane carriers were removed from the Epon block. Ultrathin sections (70 nm) were cut using an ultramicrotome (EM UC7; Leica), collected on Pioloform®-coated copper grids, stained with uranyl acetate and lead citrate, and analyzed using a Tecnai 12 Biotwin electron microscope (Thermo Fisher Scientific). Only cells with intact membranes and well-preserved organelles were further analyzed.

To analyze the content of the different fractions, sucrose fractions 1.1, 1.2, and 1.3 M were diluted to 0.8 M in D-PBS, fixed with 2% PFA, dropped on 200 mesh copper grids (Plano) coated with pioloform (Plano) and incubated for 30 minutes. After fixation with 1% glutaraldehyde, samples were contrasted with uranyl acetate (Théry et al. 2006). Electron micrographs were obtained using the Tecnai 12 Biotwin electron microscope (Thermo Fisher Scientific).

II.2.18 Expansion Microscopy

In 2015, Boyden and his team introduced a new technique called expansion microscopy (ExM) that has revolutionized the way we observe biological samples through a microscope (Chen, Tillberg, and Boyden 2015). ExM uses physical enlargement to surpass the diffraction limit, allowing us to visualize intricate details at an unprecedented level. This technique is based on a skillful combination of chemistry and physics. Fluorescently labeled molecules are crosslinked to a hydrogel, which acts as a support structure. The hydrogel is then isotropically expanded with water, resulting in a threedimensional enlargement of the sample. This isotropic expansion successfully separates the signals, enabling higher-resolution imaging. The following procedure consists of adapting the 10X expansion protocol from (Shaib et al. 2024), that has been developed to image proteins at one nanometer resolution, to expand exosomes for further characterization. To do so, exosomes immunostained and deposited on gelatin coated coverslips, were anchored by the addition of Acryloyl-X that embeds proteins into the gels. Acryloyl-X reacts with amine groups found on lysines and at the N-terminus of the proteins in the sample. The anchoring solution was kept for 16 hours at 4°C. After removing the anchoring solution, the coverslips were washed three times with D-PBS. In the meantime, the gel was prepared by dissolving sodium acrylamide (SA) monomers and N,N-dimethylacrylamide acid (DMAA) at a molar ratio of 1:4 (SA:DMAA) in ddH₂O. To illustrate, for 5 ml of solution this would mean 2.85 g ddH₂O, 1.335 g DMAA, and 0.32 g SA. The purity of SA was always checked by mixing a small aliquot with water. When the solution was clear and without yellow tint it was used for expansion. The solution was then purged with nitrogen gas (N₂) for 40 minutes at room temperature. Immediately after, the initiator of the polymerization procedure, potassium persulfate (KPS), was added at 0.4 molar% relative to the monomer concentration (0.036 g in case of 10 ml of solution) and the purging continues for 15 minutes on ice water. KPS solution was always freshly prepared. Subsequently, to accelerate the polymerization reaction, 4 µl of TEMED was added to 1 ml of the gel/KPS gelation solution. 74 µl of the resulting gel was added on parafilm and the coverslips containing stained exosomes were flipped on top of the gel within less than 80 seconds from the addition of TEMED. The coverslips were then incubated in a humidified chamber, covered, and kept for 16 hours at room temperature.

The samples were transferred into small petri dishes and washed 5 times with disruption buffer for 30 minutes each. After which the samples were autoclaved for 30 minutes at 110°C and kept in the autoclave for two additional hours to cool. The gels were then carefully washed with sodium bicarbonate buffer (pH:8) till no more bubbles from disruption buffer appeared. The gels were transferred to 12 cm petri dishes and stained with NHS-ester fluorescein for at least 1 hour at room temperature, in the dark. They were washed repeatedly till the color of the gel became transparent

and then transferred to 18 cm dishes where the 10X expansion using repetitive washing with ddH_2O takes place. After full expansion, a piece of the gel was cut, excess water was removed, and the specimen was stabilized in a specific chamber after which the sample was imaged using STED microscope in confocal mode (Figure 11).

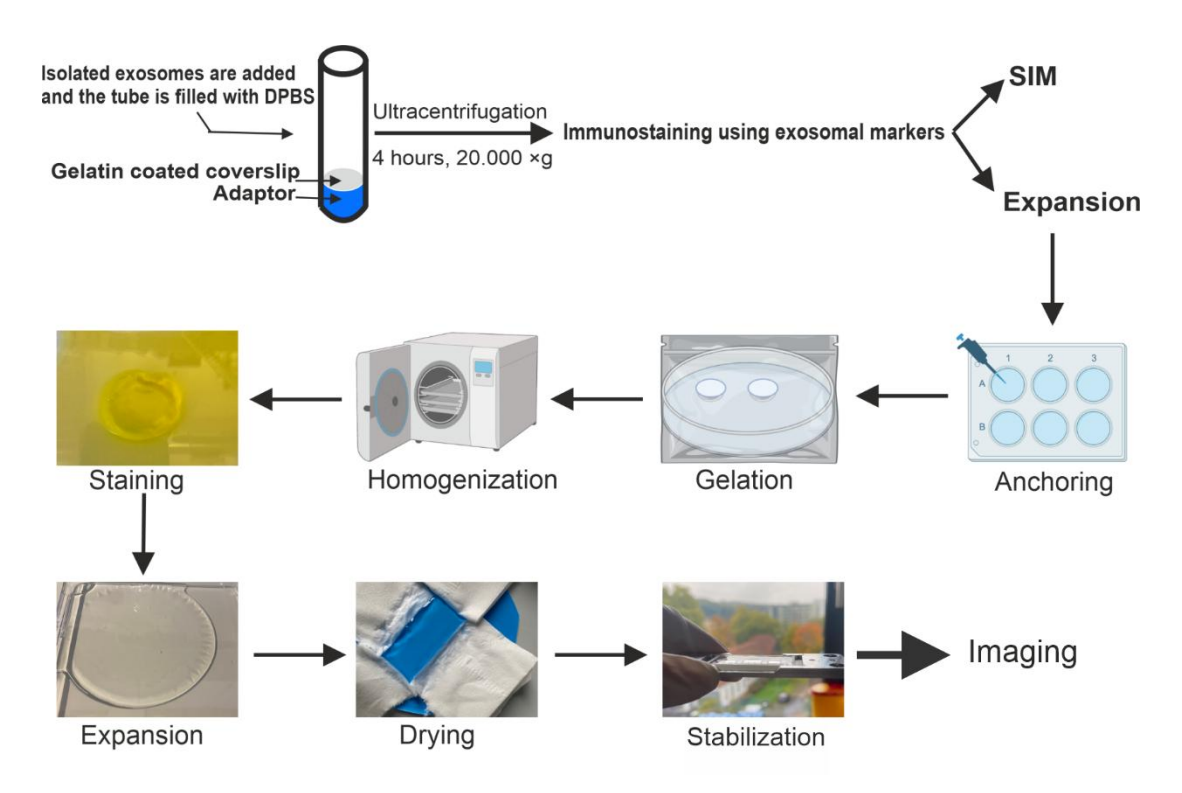


Figure 11: Schematic representation of exosome staining and expansion procedure.

II.2.19 Confocal microscopy for expansion microscopy acquisition

A four-color STED Quadscan (Abberior, Göttingen, Germany) was used in confocal mode to image expanded exosomes. The images were acquired using a 485 nm (0.85 mW), 561 nm (2 mW), and 640 nm (12 mW) pulsed lasers and a 100X/1.4NA objective (UPLSAPO 100XO, Olympus, Hamburg, Germany). Pinhole size was set to 80 μ m (1 AU). Acquisitions were carried out using a GFP detector with a spectral range of 498-520 nm with a laser power of 30%, cy3 detector with a laser power of 40%, and a cy5 detector with a laser power of 70%. The final acquisition settings included a scan range of 10 μ m × 10 μ m (X×Y), a dwell time of 3.5 μ s, and a pixel size of 98 nm. The maximum duty cycle was set to 82%, line accumulation 1, unidirectional and fast scan settings were selected. 1100 frames were acquired in 2 minutes and 19 seconds under these settings.

II.2.20 Killing assay

To check whether the exosomes isolated from CD8 $^+$ T lymphocytes are cytotoxic, the following killing assay was performed. 5×10^4 P815 cells were plated in flat bottom 96 well plates and allowed to settle for 1 hour. The cells were kept in RPMI supplemented with 10% dFCS. 10 µg of exosomes were added to each well for 12 and 24 hours and kept at 37° C/5% CO₂. As a positive control, P815 cells were lysed with either H₂O₂ or DMSO. Cells were then collected in 1.5 ml tubes and stained with caspase-3 for 1 hour at 37° C. During this time, the samples were mixed twice by tilting the 1.5 ml tubes to prevent their settling. Then, the samples were transferred to 15 ml falcon tubes and 2 ml of washing buffer was added. They were centrifuged for 6 minutes at $300 \times g$. The supernatant was discarded, and the samples were washed again. Then $400 \, \mu$ l of the washing buffer was added to each sample. For propidium iodide (PI) staining, 2 μ l of the PI solution (provided in the kit) was added to each 1.5 ml tube for a maximum of 5 minutes prior to flow cytometry analysis.

II.2.21 Flow cytometry analysis of exosome cytotoxicity

To check the percentage of killing exerted by exosomes, flow cytometry analysis was performed 12 and 24 hours after exosome addition to P815 cells immediately after the staining procedure described above. Untreated, unstained P815 cells were used to set the gates of the healthy-live population and for the negative staining. To include all the dead cells in the analysis, the gating was stretched to encompass higher and lower granularity. All flow cytometry data were acquired using a BD FACSAria III analyzer (BD Biosciences) with BD FACSDiva software 6.0. Data were analyzed with FlowJo v10.0.7 software.

II.2.22 Gel Electrophoresis of Proteins and Sample Preparation for Mass Spectrometry

Protein eluates were separated using NuPAGE 4–12% Bis-Tris gradient gels, fixed in a solution of 40% ethanol and 10% acetic acid, and incubated three times for 10 minutes with water. The gels were then stained with Coomassie solution [0.12% (w/v) Coomassie G-250 in 20% (v/v) methanol, 10% (v/v) phosphoric acid, and 10% (w/v) ammonium sulfate]. The stained gel sections were excised into three pieces, washed twice by alternating between buffer A (50 mM NH₄HCO₃) and buffer B [50 mM NH₄HCO₃/50% (v/v) acetonitrile]. Disulfide bonds were reduced by incubating the gel pieces at 56°C for 30 minutes in 10 mM dithiothreitol in buffer A, followed by carbamidomethylation at 21°C in the dark for 30 minutes in 5 mM iodoacetamide in buffer A. The gel pieces were then washed twice, alternating between buffer A and B, and dried in a vacuum centrifuge. For in-gel digestion, the gel pieces were incubated with 20 μ l of porcine trypsin (10 ng/ μ l, Promega) at 37°C overnight. Tryptic peptides were extracted twice with 50 μ l of extraction buffer (2.5% formic acid/50% acetonitrile) using

an ultrasonic bath. The extracted peptides were combined, concentrated in a vacuum centrifuge, and resuspended in 21 μ l of 0.1% formic acid.

II.2.23 Nano ESI-LC-MS² Measurements

Tryptic peptide extracts (6 μ l) were analyzed using nanoflow LC-HR-MS/MS, employing an Ultimate 3000 RSLC nano UHPLC system coupled to an LTQ Orbitrap Velos Pro mass spectrometer (Thermo Fisher Scientific, Waltham, MA, USA). Peptides were initially trapped on a 100 μ m × 2 cm Acclaim PepMap100C18 trap column (5 μ m, Thermo Fisher Scientific) and then separated on a reversed-phase C18 capillary column (75 μ m × 25 cm, 2 μ m, Acclaim PepMap, Thermo Fisher Scientific) at a flow rate of 200 nL/min over a 120-minute gradient with buffer A (water and 0.1% formic acid) and buffer B (90% acetonitrile and 0.1% formic acid). Eluted peptides were directly sprayed into the mass spectrometer using a coated silica electrospray emitter (PicoTipEmitter, 30 μ m, New Objective, Littleton, MA, USA) and ionized at 2.2 kV. MS spectra were acquired in data-dependent mode, with automatic switching between full scan MS and MS2. Full scan MS spectra (m/z 300–1,700) were obtained in the Orbitrap analyzer with a target value of 10^6. The 10 most intense peptide ions with charge states > +2 were fragmented in the high-pressure linear ion trap via low-energy collision-induced dissociation (35% normalized collision energy).

II.2.24 Raw LC-MS² Data Analysis

Tryptic peptides were identified using the MASCOT algorithm (Matrix Science, Boston, MA, USA) and TF Proteome Discoverer 1.4 (Thermo Fisher Scientific, Waltham, MA, USA). Peptides were matched to tandem mass spectra using MASCOT version 2.4.0 by searching the SwissProt database (version 2018_05, comprising 557,992 protein sequences, including 16,992 Mus musculus sequences) for mouse proteins. MS2 spectra were matched with a mass tolerance of 7 ppm for precursor ions and 0.5 Da for peptide fragment ions. Tryptic digestion was assumed, with allowance for up to two missed cleavage sites. Cysteine carbamidomethylation was set as a fixed modification, while deamidation of asparagine and glutamine, acetylation of lysine, and oxidation of methionine were considered as variable modifications. MASCOT output files (.dat) were imported into Scaffold (Version 4.8.8, Proteome Software Inc., Portland, OR, USA). The minimum criteria for protein identification required the presence of two unique peptides per protein. Protein probabilities were assigned using the Protein Prophet algorithm (Nesvizhskii et al. 2003).

III. Results

III.1 Expression and localization of CD63 and CD81 in cytotoxic T lymphocytes (CTLs)

Traditionally, several tetraspanins, especially CD63 and CD81, have been extensively used as markers of exosomes due to their abundance on exosomes and multivesicular bodies (MVBs) in various cell types (van Niel, D'Angelo, and Raposo 2018; Welsh et al. 2024). However, in cytotoxic T lymphocytes (CTLs), earlier studies revealed that tetraspanins are also present on cytotoxic granules (CGs), making them less useful as exosome markers in CTLs (Metzelaar et al. 1991; Peters et al. 1991). Recently, the discovery of new organelles in CTLs, known as multicore granules (MCGs), that also contain exosomes has further emphasized the heterogeneity of CTL organelles (Chang et al. 2022).

A series of experiments were conducted to determine the localization and specificity of CD63 and CD81 in CTLs. Day 4 activated CTLs were co-transfected with CD63-pHuji and CD81-SEP and placed on anti-CD3 ϵ coated coverslips to facilitate the formation of an immunological synapse (IS). Since GzmB is an excellent marker of CGs in CTLs (Lieberman 2003; Chang et al. 2022), the co-transfected cells were then stained with anti-GzmB antibody, and images were acquired using super-resolution structured illumination microscopy (SIM) (Figure 12A). The SIM analysis revealed a high colocalization between CD63 and the SCG and MCG marker GzmB (Manders' overlap coefficients for CD63 in GzmB: 0.47 \pm 0.05, and GzmB in CD63: 0.63 \pm 0.02, Pearson's coefficient of correlation: 0.47 \pm 0.03) (Figure 12B). In contrast, CD81 showed a much lower colocalization with GzmB (Manders' overlap coefficients for CD81 in GzmB: 0.33 \pm 0.04, and GzmB in CD81: 0.22 \pm 0.04, Pearson's coefficient of correlation: 0.24 \pm 0.03).

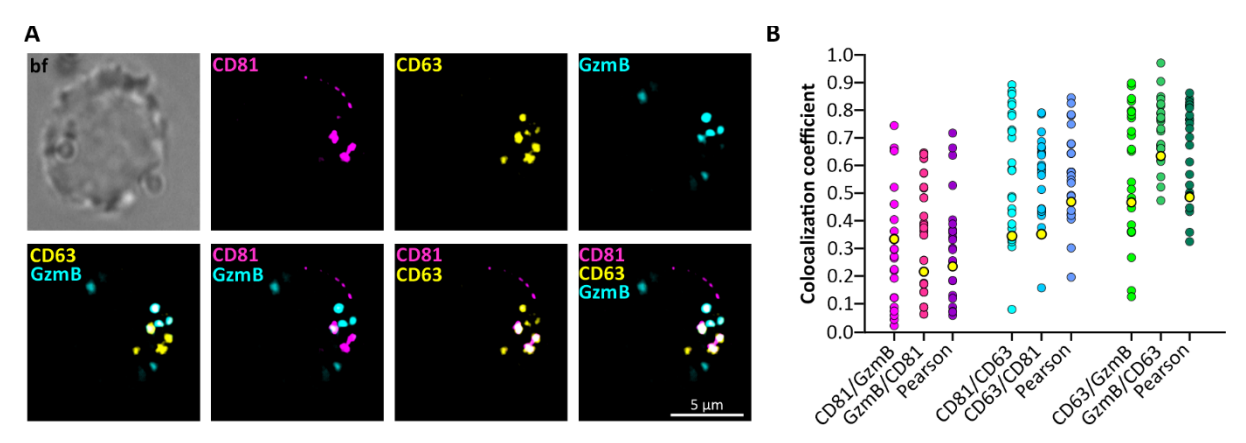


Figure 12: Colocalization analysis of exosome markers in murine CTLs.

A. Representative single plane structured illumination microscopy (SIM) images of primary murine CTLs electroporated with CD81-superecliptic pHluorin (magenta) and CD63-pHuji (yellow) and immunostained with an anti-granzyme B (GzmB) antibody coupled to Alexa 647 (cyan). Scale bar= $2 \mu m$. **B.** Mander's and Pearson's colocalization coefficients between CD81 and GzmB, CD81 and CD63, and GzmB and CD63. $N_{\text{mice}} = 3$ independent experiments, $n_{\text{cells}} = 20$.

These findings indicate different localizations of CD63 and CD81, with CD81 showing a more specific association with organelles distinct from CGs. Surprisingly, a low overlap between CD81 and CD63 was observed (Manders' overlap coefficients for CD81 in CD63: 0.37 ± 0.04 , and CD63 in CD81: 0.26 ± 0.03 , Pearson's coefficient of correlation: 0.35 ± 0.03) (Figure 12B), further supporting the notion that these tetraspanins occupy distinct compartments.

To further validate the observed localization and to investigate the specificity of CD81 for exosome-containing organelles, a correlative light electron microscopy (CLEM) experiment was conducted. Day 4 GzmB-mTFP KI CTLs were electroporated with either CD63-pHuji-Halo or CD81-Halo constructs for 12 hours and subsequently stained with SiR-647. The cells were then placed on anti-CD3ɛ coated sapphire disks and prepared for the CLEM procedure. Consistent with the high colocalization between CD63 and GzmB observed in fluorescence SIM imaging (Figure 12B), the CLEM data displayed a non-specific localization of CD63 to exosomes in CTLs. Electron micrographs showed CD63 marking exosome-containing organelles (MVBs and MCGs) as well as SCGs, which lack exosomes (Figure 13A-B). This is illustrated in Figure 13 B (top row) showing a typical SCG containing GzmB cargo but no exosomes that are nevertheless marked with CD63 on their membrane. Similarly, CD63 was detected in MCGs and MVBs containing exosomes (Figure 13B, middle and bottom row). In contrast, CD81 was exclusively detected in exosome-containing MVBs and MCGs, with no signal observed in SCGs (Figure 13C-D). Figure 13 D (upper row) reinforces the specificity of CD81 for exosome-containing organelles in murine CTLs.

Taken together, these results strengthen our earlier findings that CD63 marks a broad range of CTL organelles, including SCGs, MCGs, and MVBs, while CD81 is a more specific marker for exosome-containing organelles.

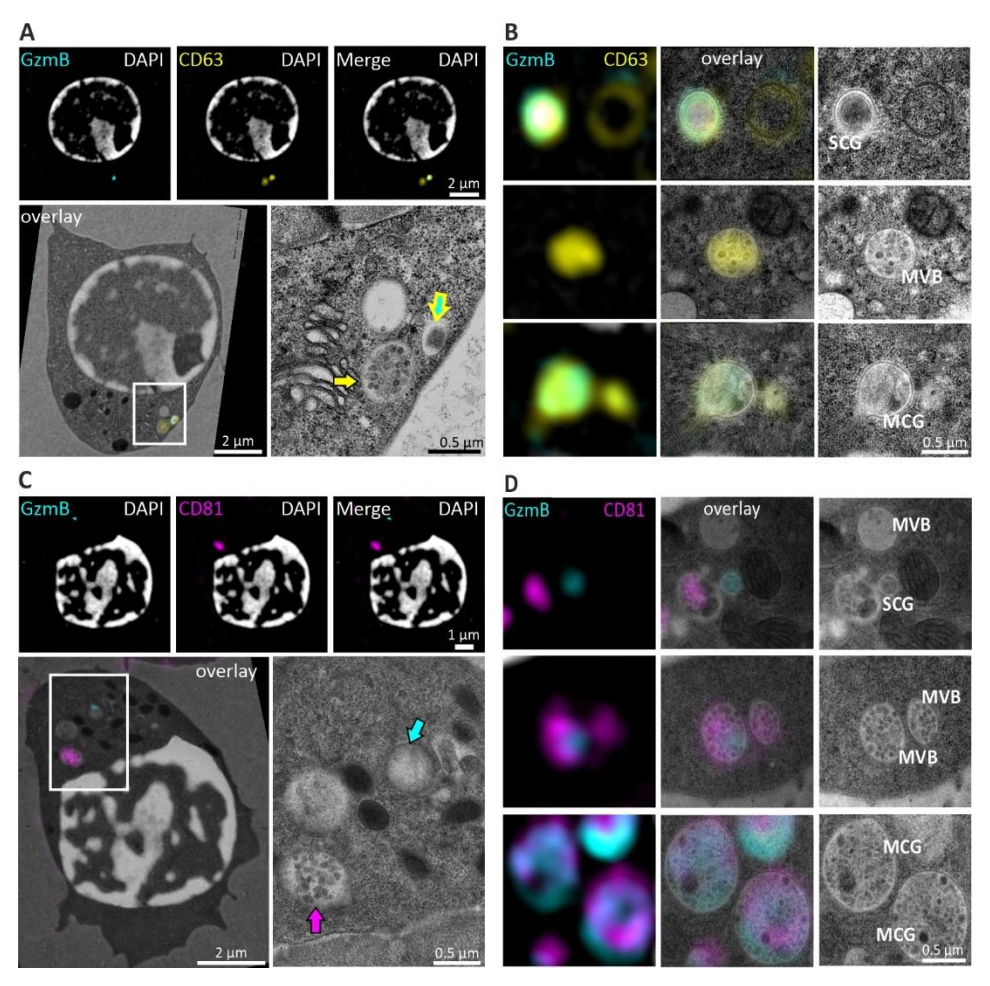


Figure 13: CD81 is a more specific exosome marker in murine CTLs than CD63.

A. Representative correlative light electron microscopy (CLEM) images of GzmB-mTFP KI CTLs electroporated with CD63-pHuji-Halo, stained with SiR 647 and DAPI (lower panel, left). Images represent an overlay between SIM images (upper panel) and their corresponding TEM images (lower panel, right). B. Enlarged CLEM images showing a typical SCG marked with CD63 and containing GzmB (top panel). The middle panel shows a representative MVB marked with CD63 and lacking GzmB. In the lower panel, shown is a representative MCG marked with CD63 and containing GzmB-positive SMAPs. Shown from left to right are the SIM, CLEM, and TEM images. C. Representative CLEM images of GzmB-mTFP KI mouse CTL electroporated with CD81-Halo and stained with SiR 647 and DAPI. D. Enlarged EM images showing a typical GzmB positive SCG lacking CD81 (top panel), representative MVBs marked with CD81 (middle panel), and representative MCGs marked with both CD81 and GzmB (lower panel). Shown from left to right are the SIM, CLEM, and TEM images. N = 3 independent experiments. SCG: single core granule, MCG: multicore granule, MVB: multivesicular body, SMAPs: supramolecular attack particles.

III.2 Investigation of fusion kinetics in different cytotoxic organelles of CTLs

The presence of diverse cytotoxic organelles in CTLs, in conjunction with the occurrence of distinct fusion modes in CTLs and NK cells (Estl et al. 2020; Liu et al. 2011), motivated us to examine whether these different fusion modes correlate with particular organelles. Given that, using SIM and CLEM analysis, we identified CD63 as a global marker of CTL cytotoxic organelles, SCGs and MCGs, as well as MVBs (Figures 12 and 13), CD63 was employed to determine whether differences in fusion kinetics exist among these organelles. The electroporation protocol was optimized as part of my work to enhance cell viability, transfection efficiency, and function of murine CTLs (Figure 8) (Alawar et al.

2024). Organelle fusion was recorded with Total Internal Reflection Fluorescence microscopy (TIRFM). Day 4 activated GzmB-mTFP KI CTLs were electroporated with CD63-pHuji for 12 hours. Following electroporation, the cells were washed with a calcium-free extracellular solution and added to a supported lipid bilayer to induce the formation of an IS (Figure 14). Since calcium influx is required for the fusion of CGs with the plasma membrane, a 10 mM extracellular calcium solution was added after the cells had settled (about one minute after recording). TIRFM images were acquired at a high temporal resolution (10 Hz), allowing for the detection of fusion events in real time. For pH-sensitive fluorophores like pHuji, fluorescence remains quenched in the acidic environment of CGs but increases sharply upon the fusion with the plasma membrane due to pH neutralization (Figure 14F) (Shen et al. 2014). Conversely, the pH-insensitive fluorophore mTFP marks fusion events by a rapid drop in fluorescence. In this study, individual fusion events were analyzed by a simultaneous drop in GzmB-mTFP fluorescence and a sudden increase in CD63-pHuji fluorescence. The analysis of fusion events revealed two distinct fusion profiles. In the first, GzmB-mTFP fluorescence disappeared rapidly, accompanied by a sudden, sharp increase in CD63-pHuji fluorescence (Figure 14A-B). In the second profile, GzmB-mTFP fluorescence also decreased rapidly, but the accompanying increase in CD63pHuji fluorescence was followed by a slower dissipation (Figure 14C-D).

To quantify these differences, the decay time—the time required for the signal to reduce to 63% of its peak value— was measured for each event. The results showed that over 60% of fusion events had a decay time longer than 2 seconds, while fewer than 40% had decay times below this threshold (Figure 14E). This 2 seconds benchmark corresponds to the decay time typically observed for SCGs marked with VAMP2-pHluorin (Verweij et al. 2018; Estl et al. 2020), suggesting that fusion events with shorter decay times are likely associated with SCGs, while those with longer decay times represent MCGs. These findings indicate that cytotoxic granules in CTLs might be categorized by their CD63-pHuji fluorescence intensity decay time, with SCGs exhibiting shorter decay times, while MCGs display slower, more sustained fusion events.

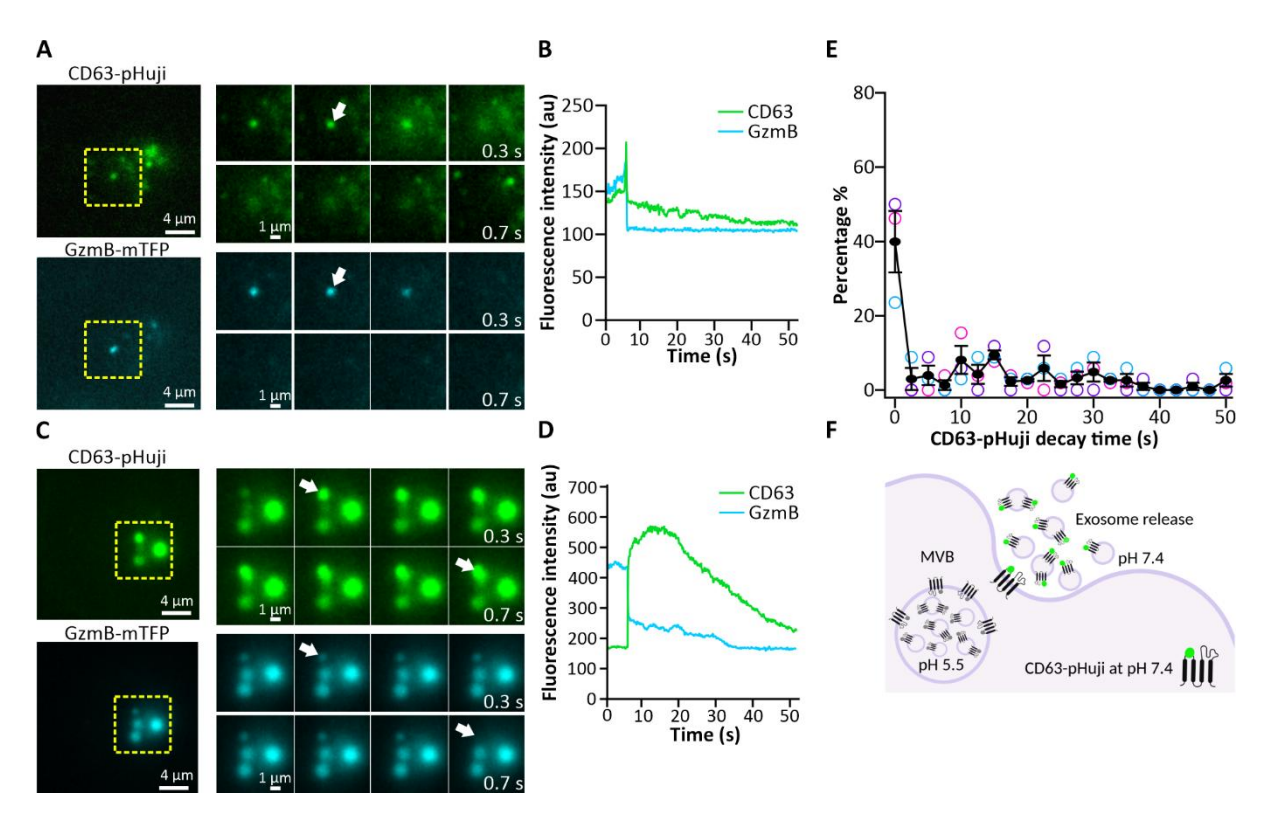


Figure 14: CD63 marks cytotoxic organelles with different fusion kinetics.

Total internal reflection fluorescent microscopy (TIRFM) snapshot images of GzmB-mTFP CTLs (cyan) expressing CD63-pHuji (green) on the supported lipid bilayer. **A**. Representative TIRFM snapshots of SCG fusion event marked with CD63-pHuji and GzmB-mTFP. **B**. Corresponding fusion profile showing fast kinetics of the SCG fusion event shown in **A**. **C**. Representative TIRFM snapshots of an MCG fusion event. **D**. Corresponding decay time of the MCG event shown in **C**. **E**. Decay time of all the analyzed CD63-pHuji fusion events. **F**. Graphic showing the unquenching of the pH-sensitive fluorophore pHuji upon the fusion of the MVB with the plasma membrane and the neutralization of the pH. Images were recorded at 10 Hz, N_{mice}= 4, n_{cells}= 50, n_{events}= 126. SCG: single core granule, MCG: multicore granule, GzmB: Granzyme B.

III.3 CD63-positive exosomes and GzmB-positive SMAPs are released from MCGs

To further investigate the observed differences in decay times and to visualize the release of exosomes and SMAPs from MCGs, day 4 WT CTLs were co-transfected with GzmB-pHuji and CD63-SEP for 12 hours. The cells were then washed with a nominal calcium-free extracellular solution and applied to anti-CD3ɛ coated glass coverslips to induce the formation of an IS. After settling, cells were induced to secrete by the addition of a 10 mM extracellular calcium solution (Figure 15). Individual fusion events were analyzed based on the sudden increase in fluorescence from both GzmB-pHuji and CD63-SEP channels. The pH-sensitive fluorophores coupled to GzmB and CD63 allowed for real-time visualization of MCG fusion events. These events involved the co-release of CD63-positive exosomes and GzmB-positive particles corresponding to SMAPs, accompanied by a prolonged decay time of both fluorophores (Figure 15C-D). In contrast, fast fusion events, corresponding to SCGs, with a decay time less than 2 seconds did not show the release of exosomes or SMAPs. These SCGs were likely marked by CD63 on their membrane and contained GzmB as cargo (Figure 15A-B). Furthermore, the decay time of GzmB fluorescence was much faster than that of CD63, which is consistent with the expected

behavior of soluble cargo (GzmB) dispersing more rapidly into the extracellular medium compared to the membrane-bound marker (CD63) (Figure 15E-F).

Overall, using CD63 as a marker for visualizing lytic granule fusion provided a clear categorization of cytotoxic granules based on their fusion kinetics: SCGs exhibited short decay times, while MCGs showed prolonged decay times. TIRFM analysis showed that 28.73 ± 2.8% cells exhibited fusion events (Figure 15G). A particularly intriguing finding from this analysis is that only 3.96% of the events at the IS were attributed to MVBs (Figure 15H). These events lacked a GzmB signal, since MVBs do not contain GzmB (Figure 13B and D, middle panel). This suggests that MCGs are the major contributors to exosome release at the IS, whereas MVBs may be responsible for exosome secretion elsewhere in the cell, independent of the IS. Taken together, these findings indicate that exosomes in CTLs can be divided into two distinct subpopulations: **polarized exosomes** contained within MCGs, which are secreted specifically at the IS, and **non-polarized exosomes** contained within MVBs, which are secreted throughout the cell. However, the question remains as to whether the formation of the IS or a specific stimulus is required to trigger the release of non-polarized exosomes from MVBs.

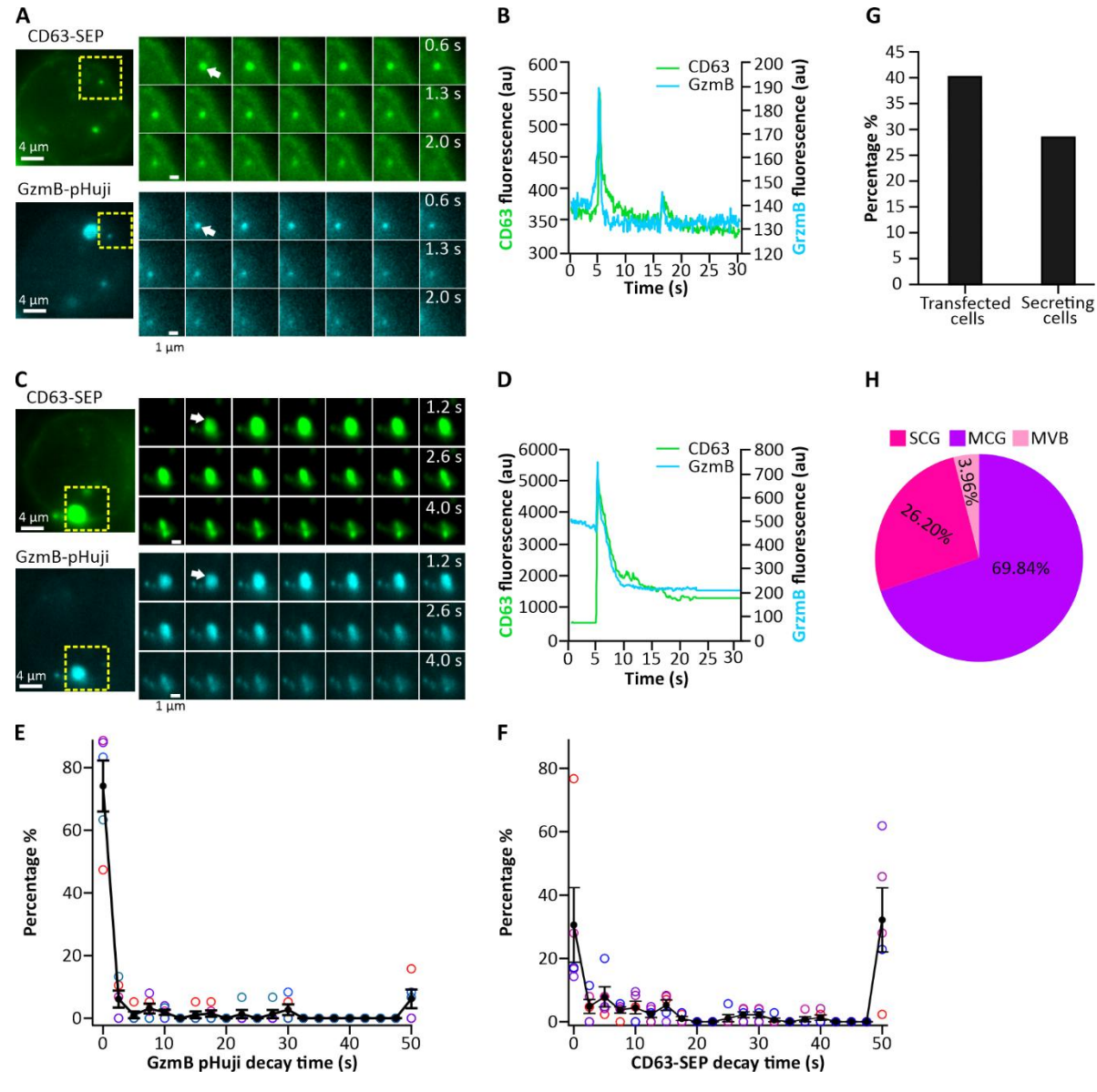


Figure 15: Visualization of exosomes and SMAPs release from MCGs at the immune synapse.

Total internal fluorescent microscopy (TIRFM) snapshots of WT CTLs electroporated with CD63-SEP (green) and GzmB-pHuji (Cyan) on anti-CD3ɛ coated coverslips. **A.** Representative WT CTL showing a fast fusion event corresponding to a typical SCG fusion. **B.** Corresponding fusion profile of the event detected in **A**, showing a sharp increase in the fluorescence intensity of CD63 and GzmB accompanied by a rapid decrease in fluorescence intensity. **C.** Representative MCG fusion event showing a very long signal duration with visible exosomes and SMAPs after secretion labeled with CD63 and GzmB respectively. **D.** Corresponding fusion profile of the MCG fusion event shown in **C**, showing a long signal duration of CD63 and GzmB fluorescence. The decay time of GzmB pHuji (**E**) and CD63-SEP (**F**) of all analyzed events. **G.** The percentage of CD81-SEP and CD63-pHuji transfected cells and the percentage of electroporated cells showing secretions. **H.** The percentage of SCG, MCG, and MVB analyzed from the total experiments N_{mice}= 5, n_{cells} = 59, n_{events}= 149. SCG: single core granule, MCG: multicore granule, SMAPs: supramolecular attack particles, GzmB: Granzyme B, SEP: super-ecliptic pHluorin.

III.4 Exosomes released at the immune synapse are derived from MCGs and have a heterogeneous tetraspanin expression

The heterogeneity of extracellular vesicles (EVs), particularly exosomes, has been widely discussed in the field, with variations often attributed to the originating cell type. Different cell types secrete exosomes with distinct markers and contents, supporting various functions (Welsh et al. 2024). In addition to the intercellular variability, there might be an intracellular variability of exosomes. Our group showed that in CTLs, exosomes are not exclusively contained within MVBs, as previously believed, but are also present in a newly described organelle, the MCG (Chang et al. 2022), indicating a new source of heterogeneity depending on the subcellular origin of the exosome. Given the lower colocalization between CD81 and CD63 observed in SIM analysis (Figure 12B), we investigated whether there is a heterogeneity in fusion dynamics of CD81- and CD63-positive organelles. To address this, TIRFM was performed on CTLs co-transfected with CD63-pHuji and CD81-SEP (Figure 16). Transfected cells were placed on anti-CD3ε coated coverslips and triggered for secretion, as previously described. The analysis of the fusion events revealed a highly heterogeneous profile that could be categorized into three distinct patterns: similar decay times for CD81 and CD63: Both tetraspanins showed comparable decay times (Figure 16A-B), suggesting a uniform distribution of these markers on both the MVB/MCG membranes and the exosomes they contain. Longer decay time for CD81: This profile exhibited a prolonged CD81 decay time, with visible CD81-positive exosomes being released (Figure 16C-D). This pattern indicates that CD81 is not only present on the organelle membrane but also on the exosome membrane, leading to a sustained fluorescence signal as the exosomes adhere to the glass coverslip. Longer decay time for CD63: In this profile, CD63 showed a longer decay time, with CD63-positive exosomes released, while CD81 had a faster decay time (Figure 16E-F). This suggests that CD63 is more enriched on the exosome membrane, prolonging its signal post-fusion. Notably, most analyzed events exhibited a longer decay time for CD63 compared to CD81 (Figure 16I), indicating that CD81 is more prominently associated with the membrane of MCGs, marking the organelle itself, while the exosomes contained within MCGs are primarily labeled with CD63.

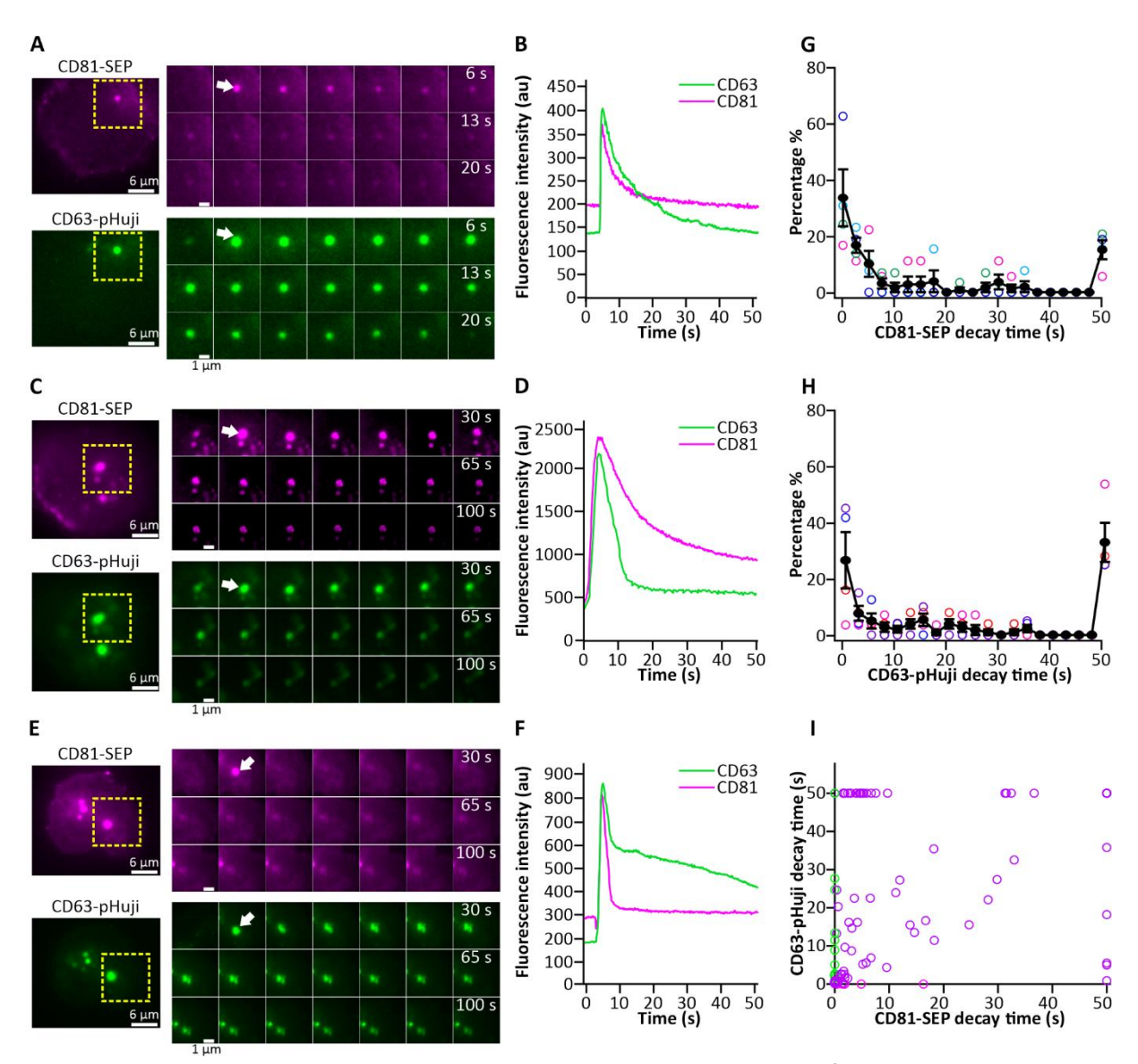


Figure 16: Exosomes containing organelles show heterogeneity in the expression of tetraspanins.

Total internal reflection fluorescence microscopy (TIRFM) snapshots of WT CTLs electroporated with CD81-SEP (magenta) and CD63-pHuji (green) on anti-CD3c coated coverslips. A. Representative CTL showing an MCG fusion event. B. Corresponding fusion profile of the event detected in A, showing a similar fusion profile for CD81-SEP and CD63-pHuji. C. Representative CD81-SEP and CD63-pHuji labeled MCG fusion event showing a long signal duration of CD81-SEP with visible CD81-positive exosomes after secretion and short CD63-pHuji signal duration with no visible CD63 labeled exosomes. D. Corresponding fusion profile of the event shown in C, showing a longer signal duration of CD81-SEP in comparison to CD63-pHuji. E. Representative CD81-SEP and CD63-pHuji labeled MCG fusion event showing a long signal duration of CD63-pHuji with visible CD63-positive exosomes after secretion and short CD81-SEP signal duration with no visible CD81 labeled exosomes post secretion. F. Corresponding fusion profile of the event shown in E, showing a longer signal duration of CD63-pHuji in comparison to CD81-SEP. The decay time of CD81-SEP (G) and CD63-pHuji (H) of all analyzed events. I. Correlation plot of the decay times of CD63-pHuji as a function of the decay time of CD81-SEP. Shown in magenta are the decay times of CD81-SEP positive fusion events without detection of CD63-pHuji. Shown in green are the decay times of CD63-pHuji positive fusion events without detection of CD81-SEP. Shown in purple are the decay times of the CD81-SEP and CD63-pHuji positive fusion events. Nmice= 5, ncells = 54, nevents= 103. SCG: single core granule, MCG: multicore granule, MVB: multivesicular body, SMAPs: supramolecular attack particles, SEP: super-ecliptic pHluorin.

III.5 MVBs and MCGs show a heterogeneous expression of v-SNARE proteins

Since our results show that the majority of exosomes released at the IS originate from MCGs rather than MVBs, we sought to test whether different vesicle-associated membrane proteins (VAMPs), i.e. v-SNAREs, mediate the fusion of these distinct organelles in murine CTLs. To achieve this, we isolated these organelles from the cells for detailed analysis. CD8⁺ T cells were isolated from WT mice, activated for 5 days, and assessed for viability and subtypes using flow cytometry (Figure 7). After activation, the cells were lysed using nitrogen cavitation, and dead cells were discarded by low-speed centrifugation. The resulting supernatant was fractionated using a discontinuous sucrose density gradient. We adapted a protocol that was used to separate MCGs from SCGs (Chang et al. 2022; Schirra et al. 2023) and optimized it to also separate MVBs from the other cytotoxic organelles (Figure 9). The different fractions obtained from the sucrose gradient were characterized by western blotting and TEM analysis (Figure 17). The early endosome marker (EEA1) was only detected in fractions 1 and 2, indicating the presence of early endosomes in these fractions (Figure 17A). Western blot analysis showed the presence of GzmB in sucrose fractions 6 and 8, corresponding to MCGs and SCGs, respectively (Figure 17A). TEM analysis validated the presence of intact MCGs in fraction 6 and SCGs in fraction 8 (Figure 17B). With the modified isolation protocol, we separated the MVBs fraction from the other organelles in sucrose fraction 4, as evidenced by its typical morphology in TEM (Figure 17B, top). Furthermore, Western blot analysis confirmed the absence of GzmB in MVBs, distinguishing them from MCGs (Figure 17A). To investigate the involvement of v-SNAREs, we performed western blot analysis on the different organelle fractions for the expression of VAMP2 and VAMP7. This analysis showed a high expression of VAMP7 in MVBs compared to MCGs, suggesting differential v-SNARE involvement in organelle fusion (Figure 17A).

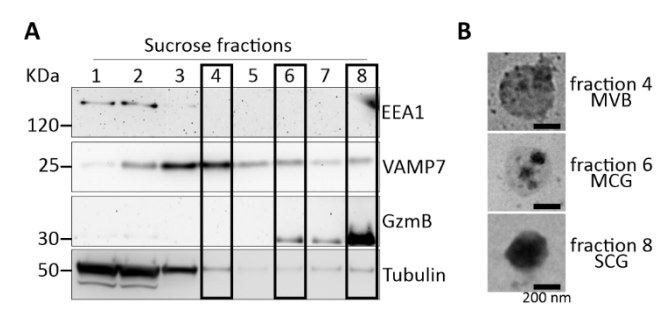


Figure 17: Subcellular fractionation of MVBs, MCGs, and SCGs from murine CTLs.

A. Representative western blot of the different sucrose fractions (1-8) probed against early endosome marker (EEA1), SNARE protein (VAMP7), cytotoxic granule marker (GzmB) and cytoskeleton marker (tubulin). **B.** Transmission electron microscopy (TEM) images of sucrose gradient fractions 4, 6, and 8 corresponding to multivesicular body (MVB), multicore granule (MCG), single core granule (SCG), N_{gradients} = 3 from 3 independent experiments.

Unfortunately, the VAMP2 antibody was not suitable for western blotting, therefore organelles isolated from WT CTLs were concentrated on 2% gelatin-coated coverslips, fixed, and stained for VAMP2 and VAMP7. The lipid marker Lysobisphosphatidic acid (LBPA) was used as an indicator of organelle integrity. The samples were then analyzed using SIM (Figure 18A). The resulting images were segmented using Cellpose 2.0. An object-based colocalization algorithm was employed to quantify the presence of the v-SNARE proteins on the different organelles. The analysis determined that MVBs exhibited significantly lower levels of VAMP2 compared to MCGs and SCGs, with only 6.82 ± 1.22% of MVBs being VAMP2-positive, compared to 21.03 ± 3.56% of MCGs and 46.23 ± 3.66% of SCGs (Figure 18B-C). In contrast, both MVBs and MCGs were enriched in VAMP7, with 52.47 ± 10.05% of MVBs and 53.10 ± 1.59% of MCGs being VAMP7-positive, while only 17.77 ± 2.10% of SCGs were positive for VAMP7 (Figure 18B-C). This suggests an abundance of VAMP7 on MVBs, an equal abundance of VAMP2 and VAMP7 on MCGs, and SCGs are predominantly marked by VAMP2 (Figure 18C). The abundance of VAMP7 on MVBs suggests that their fusion with the plasma membrane, unlike that of MCGs and SCGs, may be independent of VAMP2. Considering that our previous TIRFM analysis showed only 3.96% of secretions corresponded to MVBs (Figure 15H), we can infer that most of the exosome secretion at the IS is VAMP2-dependent. The VAMP7-positive MVBs are likely involved in exosome secretion elsewhere in the cell, independent of the IS.

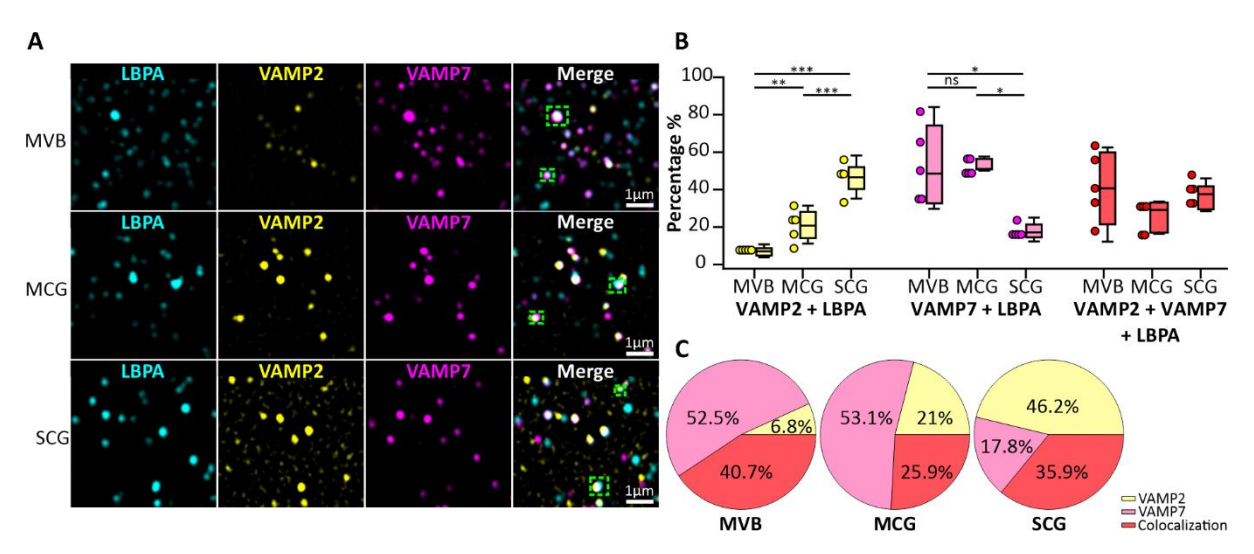


Figure 18: The SNARE protein VAMP7 specifically labels MVBs and MCGs containing exosomes.

A. Representative structured illumination microscopy (SIM) images of organelles corresponding to MVBs (Top), MCGs (middle), and SCGs (bottom). The organelles were isolated from WT CTLs, centrifuged on gelatin-coated coverslips, fixed, and stained with anti-LBPA (cyan), anti-VAMP2 (yellow), and anti-VAMP7 (magenta) antibodies. Shown are the images of the individual channels and the merged images of all three channels. **B.** Object-based colocalization analysis of all three proteins displayed as scatter dot plots with the values superimposed with a box plot comprising the median (line). **C.** Pie chart representing the percentage of VAMPs in each of the isolated organelles. $N_{gradients} = 3$, from 3 independent experiments, organelles analyzed: 7620 SCG, 15650 MCG and 13710 MVBs. SCG: single core granule, MCG: multicore granule, MVB: multivesicular body, LBPA: Lysobisphosphatidic acid, ns: not significant. Data represented as mean \pm SEM, *p < 0.05, **p < 0.01, ***p < 0.001.

III.6 CD81 is a more specific exosome marker in murine CTLs

After finding a difference in the expression of v-SNAREs on the surface of MVBs, MCGs, and SCGs (Figure 18), as well as the distinct fusion dynamics of CD81 and CD63 positive organelles in TIRFM experiments (Figure 16I), we sought to determine whether the membrane of these organelles exhibits differences in their tetraspanins content. To investigate this, we isolated organelles from WT CTLs, concentrated them on 2% gelatin-coated coverslips, and stained them without permeabilization for the surface markers CD81, CD63, and LBPA. Images were acquired using SIM; segmented using Cellpose 2.0, and subjected to object-based colocalization analysis using MATLAB (Figure 19A). To ensure the accuracy of our analysis, we only included organelles with diameters larger than 200 nm in fraction 8 and 350 nm in fractions 4 and 6 that colocalized with LBPA, thereby avoiding any individually labeled exosomes or membrane pieces that may have resulted from organelle disruption. The results from this analysis indicated significant differences in tetraspanin expression among the different organelles. MVBs and MCGs had significantly higher levels of CD81 on their membrane compared to SCGs, with $79.14 \pm 2.06\%$ of MVBs and $73.19 \pm 2.09\%$ of MCGs being CD81-positive, while only 31.92± 8.85% of SCGs were positive for CD81 (Figure 19B). Conversely, the membrane of SCGs was enriched in CD63 compared to MVBs and MCGs, with 64.53 ± 9.47% of SCGs being CD63-positive, compared to only 14.38 ± 2.11% of MVBs and 15.53 ± 1.63% of MCGs (Figure 19B). These results suggest that CD81 is a more reliable marker for distinguishing organelles containing exosomes from SCGs, as it is consistently more abundant on the membrane of MVBs and MCGs than on SCGs membrane. Another notable finding from this experiment is the very low colocalization between CD63 and CD81 on MVBs and MCGs (Figure 19B). This observation raises intriguing questions regarding the potential heterogeneity within the exosome population itself. While the heterogeneity of EVs is a wellestablished concept, most studies have focused on differences between EV subtypes, such as microvesicles and exosomes (Welsh et al. 2024). However, little is known about the heterogeneity within the exosome population itself. While some studies have documented differences in RNA content among exosomes, it has been largely assumed that tetraspanins are universally present on exosomes, making them reliable general markers.

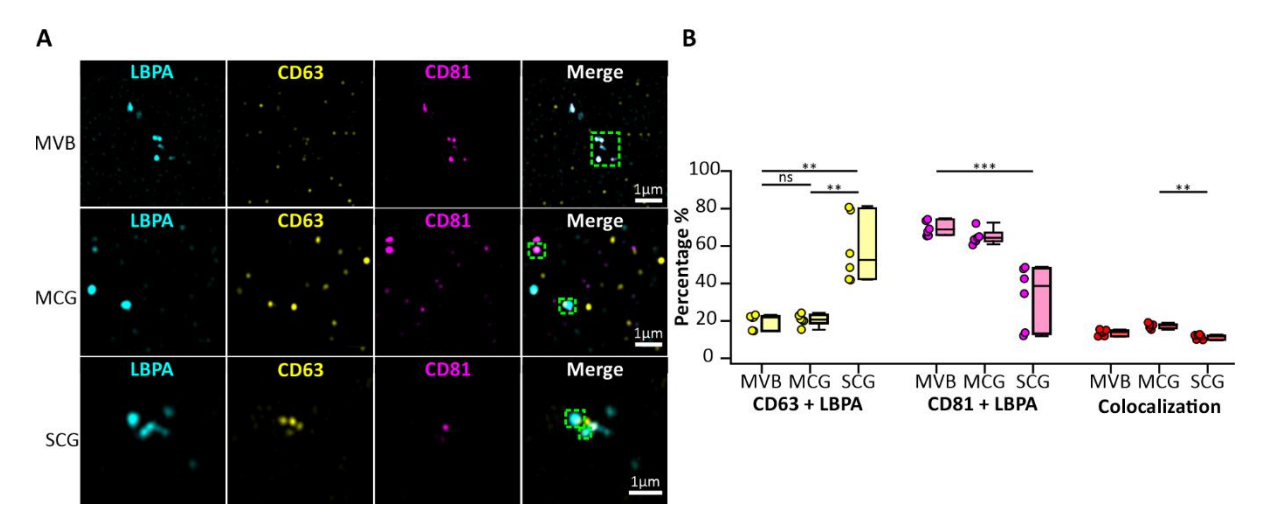


Figure 19: The tetraspanin CD81 is a more specific exosome marker in murine CTLs than CD63.

A. Representative organelles corresponding to MVBs (Top), MCGs (middle), and SCGs (bottom). The organelles were isolated from WT CTLs, centrifuged on gelatin-coated coverslips, fixed, and stained with anti-LBPA (cyan), anti-CD63 (yellow), and anti-CD81 (magenta) antibodies. Images were acquired with structured illumination microscopy (SIM). Shown are the images of the individual channels and the merge of all three channels' images. **B.** Object-based colocalization analysis of all three proteins displayed as scatter dot plot with the values superimposed with a box plot comprising the median (line). Ngradients = 3, from 3 independent experiments, organelles analyzed: 7620 SCG, 11245 MCG, and 11720 MVBs. SCG: single core granule, MCG: multicore granule, MVB: multivesicular body, LBPA: Lysobisphosphatidic acid, ns: not significant. Data represented as mean ± SEM, **p < 0.001.

III.7 Exosomes derived from murine CTLs could be divided into two subpopulations based on their size

The observed heterogeneity in SNARE proteins and tetraspanins between MVBs and MCGs (Figures 18-19) motivated further characterization of exosomes secreted by murine CTLs. To achieve this, 10×10^6 CTLs were activated for 5 days using anti-CD3/CD28 coated beads in conditioned media. Exosomes were isolated from the supernatant of $600-800 \times 10^6$ CTLs via differential ultracentrifugation. The small EVs pelleted at 100,000 x g were further purified using an optimized sucrose density gradient (Figure 10). Consistent with the literature, exosomes were expected to float within the sucrose density range of 1.15-1.19 g/cm3 (Théry et al. 2006). To confirm the presence of CTL-derived exosomes in these fractions, TEM analysis was performed. The analysis revealed the presence of highly pure exosomes in fractions 1.1, 1.2, and 1.3 M (Figure 20 A-D). Interestingly, two distinct size populations were detected in these fractions. The first size population ranged from 30-80 nm, while the second ranged from 80-150 nm (Figure 20A-C). This finding suggests the existence of a heterogeneous population of exosomes secreted by murine CTLs, suggesting functional diversity within these vesicle subtypes. The different sucrose fractions were then analyzed by western blotting for exosome markers. Western blot analysis confirmed the presence of classical exosome markers, ALIX and TSG101, in fractions 1.1, 1.2, and 1.3 M (Figure 20E), further validating that these fractions contained exosomes. To maximize the yield of exosomes for further studies, fractions 1.1, 1.2, and 1.3 M were pooled together. This pooling enabled successful detection of the tetraspanin CD81 (Figure 20F). The identification of two distinct exosome size populations, combined with differences in tetraspanin and SNARE protein content, highlights the complex nature of exosome biogenesis in CTLs.

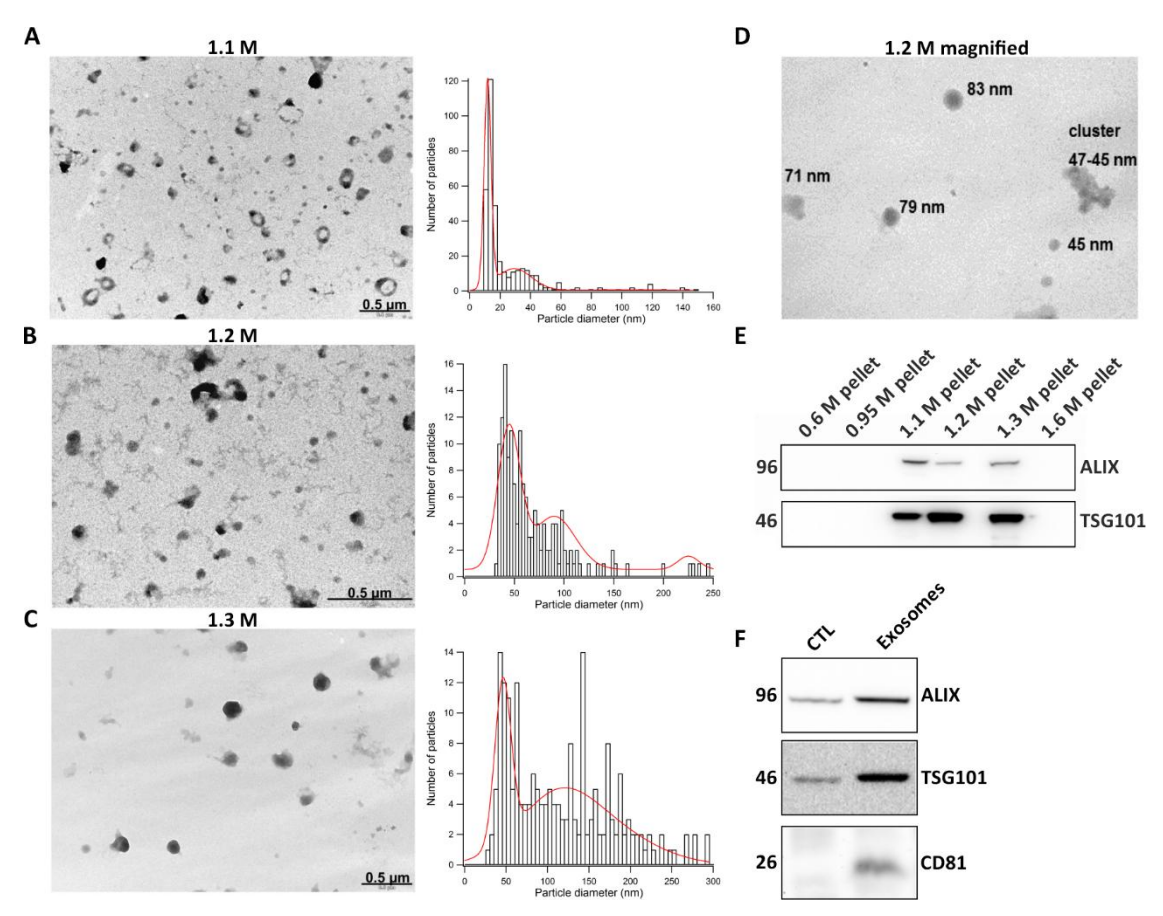


Figure 20: Characterization of exosomes isolated from murine CTLs.

Transmission electron microscopy (TEM) images of sucrose fractions 1.1 M (A), 1.2 M (B), 1.3 M (C) with the diameter analysis of each fraction. **D**. Magnified TEM image from sucrose fraction 1.2 M showing typical exosomes. **E**. Western blot for sucrose fractions 0.6-1.6 M (10 μg protein/lane) probed against exosome markers ALIX and TSG101. **F**. Western blot for cytotoxic T lymphocyte (CTL) lysate and exosomes pooled from fractions 1.1, 1.2, and 1.3 M probed against the exosome markers ALIX, TSG101, and CD81.

The presence and purity of the isolated exosomes were further validated using mass spectrometry (MS) analysis. A total of 824 proteins were identified from the WT exosome samples using MS, based on a stringent 1% false discovery rate (FDR) and a minimum of two unique peptides per protein. The list of proteins was compared to the Top 100 proteins identified in the Exocarta database and the results indicated that 79 proteins of the CTL-derived exosomes isolated in this study are found in the Top 100 list (Figure 21A). Importantly, calnexin, a common contaminant associated with the endoplasmic reticulum, was not detected, indicating that the isolation protocol was highly efficient in yielding pure exosomes with minimal contamination. Moreover, the analysis of the subcellular location of the identified proteins revealed that 63.83% of the proteins are known extracellular vesicle

markers and only 0.12% and 0.24% are Golgi and ER markers respectively, showing that with the followed isolation procedure, a high purity of exosomes is isolated (Figure 21B). The identified proteins were categorized into several functional categories. Proteins involved in vesicle formation, transport, and fusion were well represented. High levels of CD82 and TSG101, essential for exosome formation, were detected, underscoring their role in the biogenesis and function of exosomes. Proteins linked to immune signaling and modulation, such as MHC class I molecules and other immune-related proteins, were present, suggesting that CTL-derived exosomes might play a role in immune surveillance or antigen presentation. The exosome cargo also included key signaling molecules, indicating their potential function in cell-to-cell communication, possibly mediating responses to immune stimuli or other signals within the microenvironment. Proteins associated with cellular stress, such as HSP70, were abundant. Heat shock proteins are often implicated in the loading of antigens onto exosomes, which could be relevant for immune modulation and cytotoxicity in CTLs. Metabolic enzymes, including GAPDH, were also identified, reflecting the potential involvement of exosomes in metabolic regulation or possibly as a source of metabolic information exchange between cells. The mass spectrometry data, alongside the earlier results from western blotting and TEM, not only supports the purity of the exosome preparation but also highlights the functional diversity of exosomes secreted by CTLs.

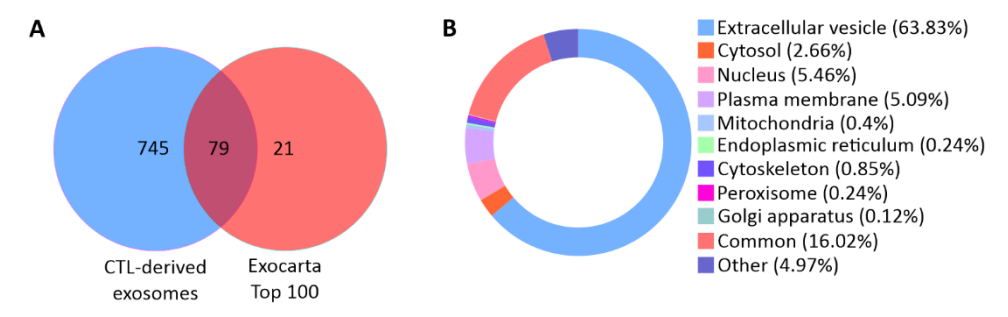


Figure 21: Proteomic analysis of exosomes isolated from WT murine CTLs.

A. Venn diagram displaying the number and overlap of proteins identified from WT murine CTLs-derived exosomes in this study with those in the Exocarta Top 100 exosome proteins. **B**. Pie chart showing the subcellular location of the total identified proteins predicted by Scaffold software.

III.8 10X expansion of exosomes derived from murine CTLs showed that the tetraspanins CD63 and CD81 locate to different exosomal subpopulations

To better understand the heterogeneity of exosomes derived from murine CTLs, exosomes isolated from sucrose fractions 1.1, 1.2, and 1.3 M were pooled together and pelleted on 2% gelatin-coated coverslips by ultracentrifugation at $20,000 \times g$ for 4 hours. After pelleting, the coverslips were immediately fixed, permeabilized, and stained with antibodies against the exosome surface markers CD81 and CD63. Samples were then imaged using SIM (Figure 22A). The resulting images were

segmented using CellPose, and object-based colocalization analysis was performed with MATLAB. Surprisingly, a minimal colocalization between CD63 and CD81 was observed. Specifically, Manders' overlap coefficients showed only 0.054 ± 0.002 for CD81 within CD63, and 0.046 ± 0.003 for CD63 within CD81, while the Pearson's correlation coefficient was similarly low at 0.041 ± 0.001 (Figure 22B). This indicated that CD81 and CD63 were localized to distinct exosome subpopulations in murine CTLs.

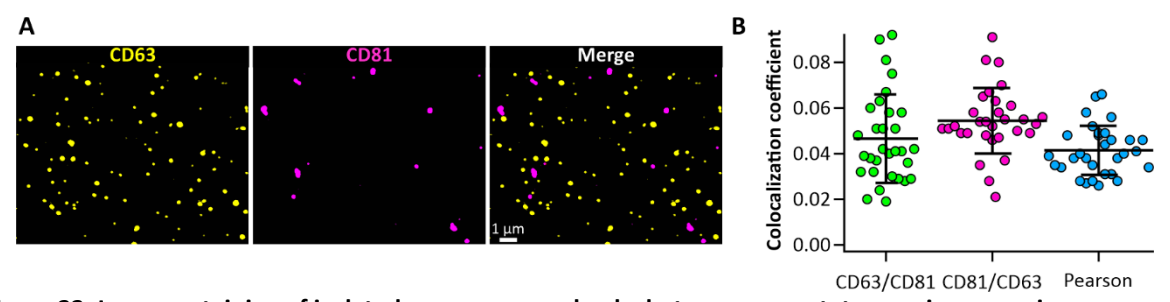


Figure 22: Immunostaining of isolated exosomes revelaed a heterogeneous tetraspanin expression. A. Representative structured illumination microscopy (SIM) images of exosomes isolated from WT CTLs, centrifuged on gelatin-coated coverslips, fixed, and stained with anti-CD63 (yellow) and anti-CD81 (magenta) antibodies. Shown are the images of the individual channels and the merge image of the two channels. **B.** Mander's and Pearson's colocalization coefficients between CD81 and CD63. Data represented as mean ± SEM, N = 3 independent experiments.

To further validate this observed heterogeneity and to characterize the two distinct exosome subpopulations, I have adapted the 10X expansion microscopy protocol (Shaib et al. 2024), typically used for protein characterization, and optimized it for expanding exosomes. Exosomes pelleted on gelatin-coated coverslips were fixed and stained with antibodies specific to CD81 and CD63. A gelcompatible anchor (Acryloyl-X) was applied to attach the lysine residues of the exosomes to a swellable gel matrix. After hydrolysis through heat treatment, which created main chain breaks and thus allowed the isotropic expansion of the sample, the samples were then stained with Nhydroxysuccinimide ester (NHS-ester) fluorescein to label the exposed amino groups generated after homogenization. A 10-fold expansion was achieved through repetitive washing with distilled water. The samples were then imaged using a four-color STED Quadscan in confocal mode, with 1100 frames acquired (Figure 11). The ONE platform plugin on ImageJ was used to correct sample drift during acquisition and reconstruct the final image (Shaib et al. 2024). The expanded exosomes confirmed the previously observed heterogeneity, revealing that CD81 and CD63 mark entirely separate populations of exosomes. Remarkably, no exosomes were found to be double-positive for both CD81 and CD63 (Figure 23), reinforcing the idea that these two tetraspanins define distinct subpopulations. Interestingly, the imaging of expanded exosomes revealed a correlation between size and tetraspanin expression. CD81 was predominantly associated with smaller exosomes, in the range of 30-80 nm (nexosomes = 8, Figure 23, top), while CD63 was more commonly found on larger exosomes, ranging from

80-150 nm (n_{exosomes}= 10, Figure 23, bottom). This suggests that the size of the exosome may relate to the specific tetraspanins it carries, potentially reflecting distinct origins, functions, or cargo types.

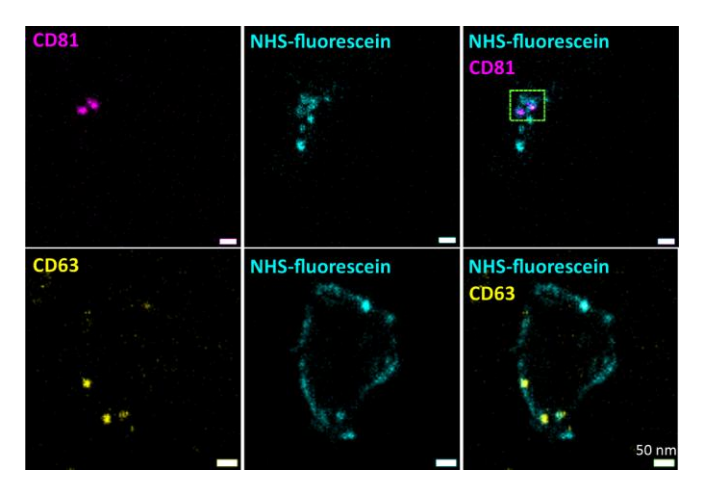


Figure 23: Exosomes derived from murine CTLs are divided based on their tetraspanins surface marker into two subpopulations, CD63-positive and CD81-positive exosomes.

Exosomes isolated from WT CTLs were pelleted on gelatin-coated coverslips, fixed, and stained against the tetraspanins CD81 (magenta) and CD63 (yellow). Stained exosomes were then subjected to the 10X expansion protocol and stained with NHS-ester fluorescein (cyan). Images were acquired with STED microscopy in confocal mode. Shown is a representative image of CD81-positive exosome (green box, *top*) and CD63-positive exosome (*bottom*). N = 3 independent experiments.

III.9 Murine CTL derived exosomes contained in MVBs are secreted in a MUNC13-4 independent manner

It has become clear that exosomes derived from murine CTLs are quite heterogeneous. These exosomes are not only located in two different organelles (MVBs and MCGs), but they can also be divided into two subpopulations based on their surface markers: CD63-positive and CD81-positive exosomes (Figures 22-23). This heterogeneity raised the question of whether the secretion of these exosomes is limited to the IS or can occur at other cellular sites. Given that MUNC13-4 is a crucial priming factor for the secretion of lytic granules at the IS (Dudenhöffer-Pfeifer et al. 2013), we sought to investigate whether the fusion of exosome-containing organelles, such as MVBs and MCGs, is also dependent on MUNC13-4. To address this, exosomes were isolated from WT and MUNC13-4 KO CTLs through ultracentrifugation and a sucrose density gradient. The isolated exosomes were then analyzed by TEM to assess their presence and purity. The TEM data showed that both WT and MUNC13-4 KO CTLs secreted exosomes, indicating that exosome release can occur independently of MUNC13-4 (Figure 24A). Analysis of exosome diameter revealed no significant differences between the two conditions, with an average diameter of 76.59 ± 1.92 nm in WT-derived exosomes and 75.89 ± 2.44 nm in MUNC13-4 KO-derived exosomes (Figure 24B), suggesting that MUNC13-4 does not influence the size or maturation of exosomes in murine CTLs. However, there was an 18.13% reduction

in exosome yield from MUNC13-4 KO CTLs compared to WT (Figure 24C). To determine whether this reduction was specific to CD81-positive or CD63-positive exosomes, the isolated exosomes from WT and MUNC13-4 KO CTLs were stained for both markers (Figure 24D). The analysis revealed a significant reduction in CD63-positive exosomes, with 63.87 \pm 1.65% of WT-derived exosomes expressing CD63, compared to only 56 \pm 1.75% in MUNC13-4 KO exosomes. Conversly, there was a slight increase in CD81-positive exosomes in the MUNC13-4 KO CTLs (32.61 \pm 0.99%), compared to WT-derived exosomes (22.38 \pm 1.53%) (Figure 24E). To further assess whether the secretion of MCGs is MUNC13-4 dependent, TIRFM analysis was performed on MUNC13-4 KO CTLs overexpressing CD63 and CD81 (data not shown, N=3 independent experiments, n_{cells} = 35). Interestingly, the results showed no secretion of exosomes at the IS from these cells, confirming that MCG secretion is MUNC13-4-dependent, while MVBs are secreted independently of MUNC13-4, and likely outside the IS. Taken together, these results suggest that exosomes secreted at the IS are enriched in CD63 and are contained within MCGs that are secreted in a MUNC13-4 dependent manner, conversly CD81-positive exosomes appear to be enriched in MVBs secreted elsewhere throughout the cell in a MUNC13-4 independent manner.

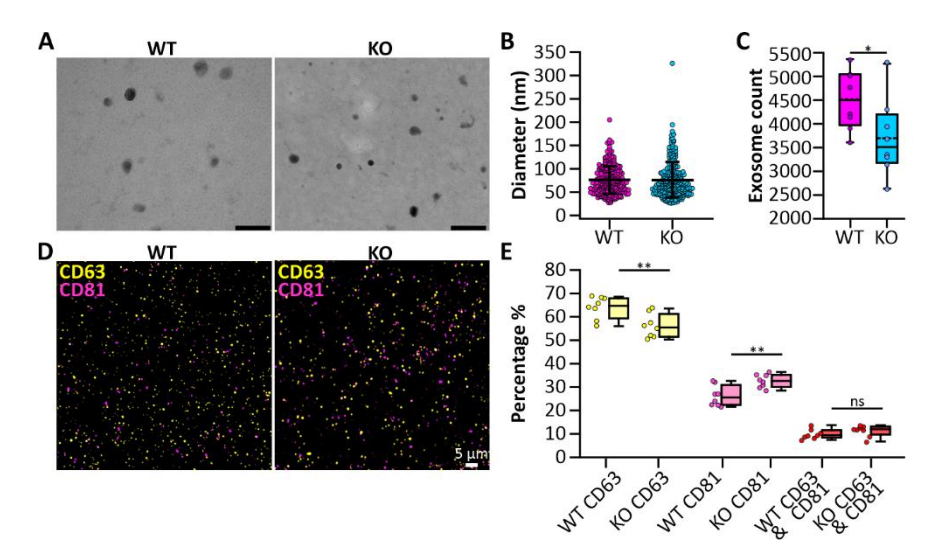


Figure 24: MUNC13-4 KO CTLs secrete exosomes with a similar morphology to the WT exosomes.

A. Representative transmission electron microscopy (TEM) images of exosomes isolated from WT CTLs (left) or MUNC13-4 KO CTLs (right), scale bar 0.5 μ m. **B.** Scatter dot plot analysis of the diameter of exosomes isolated from WT or KO CTLs. **C.** Box plot showing the number of exosomes isolated from WT or MUNC13-4 KO CTLs supernatant. **D.** Representative structured illumination microscopy (SIM) images of exosomes isolated from WT (left) or MUNC13-4 KO CTLs (right), centrifuged on gelatin-coated coverslips, fixed, and stained with anti-CD63 (yellow) and anti-CD81 (magenta) antibodies. Shown are the images of the merge of the two channels. **E.** Object-based colocalization analysis of CD63 alone (yellow), CD81 alone (magenta), and the colocalization of CD63and CD81 (red) displayed as scatter dot plot with the values superimposed with a box plot comprising the median (line). $N_{gradients} = 3$, from 3 independent experiments. Data represented as mean \pm SEM, *p < 0.05, **p < 0.01, ns: not significant.

III.10 Exosomes derived from WT and MUNC13-4 KO CTLs possess cytotoxic activity

To assess the biological properties of exosomes derived from CTLs on tumor cell lines, exosomes from both WT and MUNC13-4 KO CTLs were incubated with P815 tumor cells for 12 and 24 hours. Following incubation, the P815 cells were analyzed using flow cytometry to assess caspase 3 activation and propidium iodide (PI) staining, which are markers for apoptosis and cell membrane integrity, respectively (Figure 25A). After 12 hours of incubation, the results showed a notable difference in the apoptotic activity between exosomes derived from WT and MUNC13-4 KO CTLs. Caspase 3 activation, indicative of early apoptosis, was observed in $33.06\% \pm 1.27$ of cells treated with WT exosomes, which was significantly higher compared to the $15.53\% \pm 0.49$ observed in cells treated with KO exosomes (Figure 25B). The percentage of cells double positive for both PI and caspase 3, indicating cells in the later stages of apoptosis, was identical for both WT and KO exosome-treated groups, with $6.46\% \pm 1.22$ for WT and $6.46\% \pm 0.1$ for KO, respectively (Figure 25B). After 24 hours of incubation, the effects on the P815 cells became more pronounced. The percentage of caspase 3 activation increased over time in both groups, reaching $56.96\% \pm 3.42$ in the WT group, which was significantly higher compared to the $28.26\% \pm 3.12$ in the KO group (Figure 25C).

The percentage of cells double positive for both PI and caspase 3 rose to $9.2\% \pm 1.36$ for the WT group and $9.82\% \pm 1.43$ for the KO group, indicating that more cells in both groups were progressing towards late-stage apoptosis or necrosis over time (Figure 25C). Overall, these results suggest that exosomes from WT CTLs are more potent in inducing apoptosis in P815 tumor cells compared to exosomes from MUNC13-4 KO CTLs.

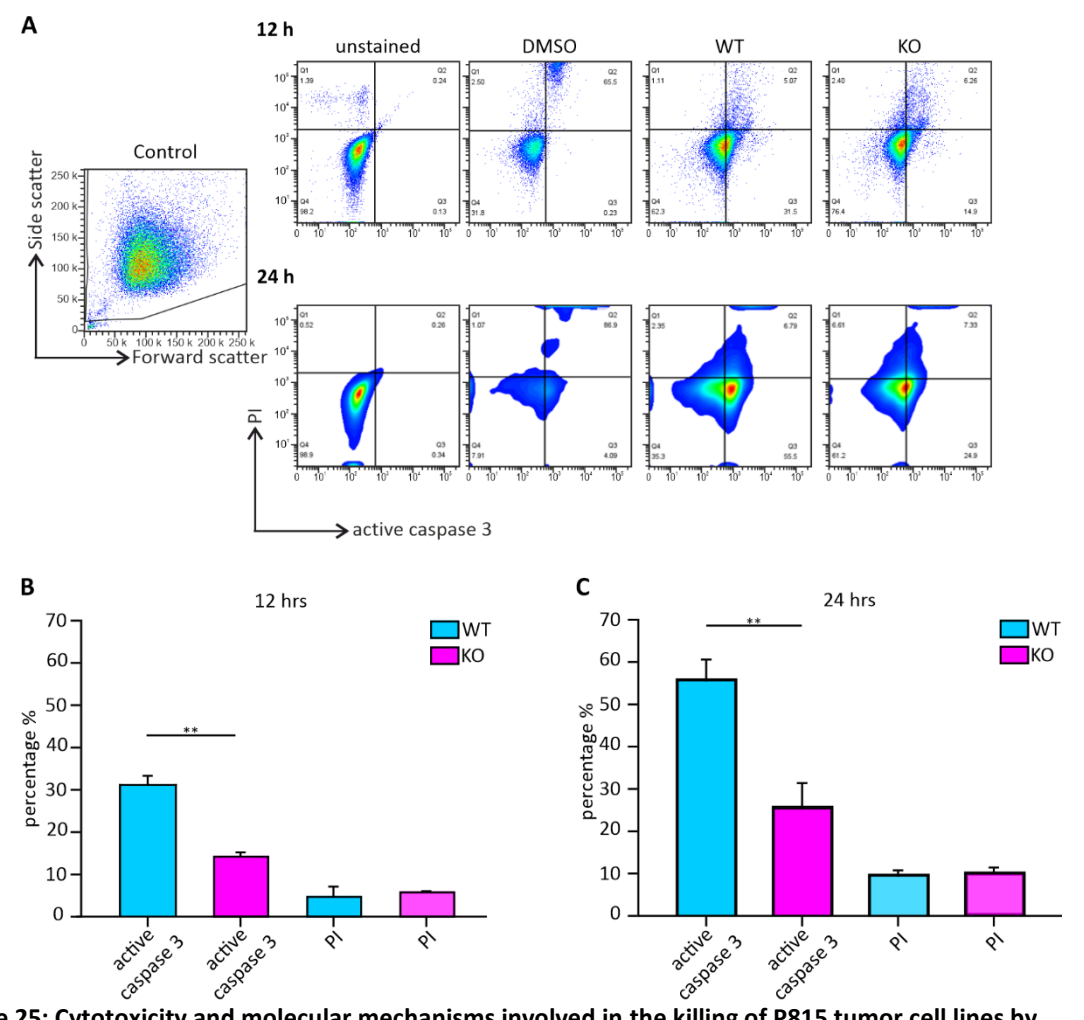


Figure 25: Cytotoxicity and molecular mechanisms involved in the killing of P815 tumor cell lines by CTL-derived exosomes.

Cytotoxic assay on P815 target cells incubated with 10 μ g/ml WT or MUNC13-4 KO-derived exosomes. **A.** Representative flow cytometry analysis of the cytotoxic activity of CTL-derived exosomes. Cells were gated based on the forward and side scatter. DMSO was used as a positive control. The percentage of active caspase 3 and PI positive cells was evaluated after 12 (**B**) and 24 h (**C**) of incubation with CTL exosomes. N = 3, from 3 independent experiments. Data represented as mean \pm SEM, **p < 0.01.

Since previous results in this study demonstrated that under KO conditions, only MVBs containing exosomes can fuse with the plasma membrane, while MCGs do not, the decreased cytotoxicity observed in the KO condition relative to WT suggests that exosomes from MCGs are more cytotoxic than those from MVBs. Thus, it appears that the exosomes contained in MCGs contribute significantly to the cytotoxic effect on target cells, highlighting a functional distinction between exosomes from different organelles within CTLs. Furthermore, the significant increase in caspase 3-positive cells from 12 to 24 hours in both WT and KO conditions suggests a progressive accumulation of apoptotic signals over time, highlighting the sustained and enhanced cytotoxic potential of exosomes over extended periods.

IV. Discussion

The main objective of the present work was to characterize exosomes derived from murine cytotoxic T lymphocytes (CTLs) and investigate their function. Using CLEM, SIM, and TIRFM, we traced the journey of CTL-derived exosomes and demonstrated that they reside within two distinct organelles, multivesicular bodies (MVBs) and multicore granules (MCGs). Notably, we report that CD81 is a specific exosome marker that selectively labels exosome-containing organelles in CTLs. Through detailed analysis with CLEM, mass spectrometry, and expansion microscopy, we further characterized exosomes into two distinct subpopulations: smaller, CD81-positive exosomes and larger, CD63-positive exosomes. My findings further reveal a functional polarization, with exosomes within MCGs directed toward the immune synapse and released in a MUNC13-4 dependent manner, while non-polarized exosomes, housed in MVBs, are released in a MUNC13-4 independent manner throughout the cell's plasma membrane. Importantly, this study shows that polarized exosomes exhibit significantly greater cytotoxic potential than their non-polarized counterparts.

IV.1 Exosomes are contained in two distinct organelles in murine CTLs

Cytotoxic T lymphocytes (CTLs) play a crucial role in the adaptive immune system by identifying and eliminating infected or malignant cells. They achieve this through the release of cytotoxic organelles, notably single core granules (SCGs), which contain perforin and Granzyme B (GzmB) (Peters et al. 1991). Recently, our lab identified MCGs as another important cytotoxic organelle within CTLs. MCGs contain dense particles called supramolecular attack particles (SMAPs) along with other less dense nanovesicles (Chang et al. 2022). This work in addition to a previous study by Bálint et al. (2020) has focused on the release of SMAPs at the immune synapse and their role in target cell killing. The presence and functional implications of the nanovesicles resembling exosomes within MCGs remained unexplored. Exosomes, which are 30-150 nm nanovesicles formed within MVBs, facilitate cell-to-cell communication and play a significant role in modulating immune responses (Welsh et al. 2024; Raposo et al. 1996). While exosomes released from immune cells like CD4⁺ T cells, NK cells, and DCs are welldocumented, those specifically derived from CD8⁺ CTLs remain underexplored (Raposo et al. 1996; Zitvogel et al. 1998; Enomoto et al. 2022). In this study, we sought to determine whether murine CD8⁺ CTLs contain exosomes in two distinct organelles: conventional MVBs and the newly identified MCGs. Traditionally, tetraspanins such as CD63, CD81, and CD9 have been known for decades to be among the proteins commonly associated with exosomes (Kowal et al. 2016). These proteins not only label the exosomes but also the membrane of the organelles containing them, making them useful for realtime visualization of exosome release from cells (Verweij et al. 2018). We first co-expressed the exosome markers CD81 and CD63 in day-5 activated CTLs and used GzmB as a marker for cytotoxic

organelles. For the first time, we demonstrate that CTLs house exosomes within two structurally distinct organelles (Figure 13). CLEM analysis revealed that both MVBs and MCGs are marked by CD63 and CD81; however, GzmB labeled MCGs and SCGs, confirming its absence in MVBs (Figure 13). Notably, GzmB was restricted to the electron-dense regions of MCGs, indicating its association with SMAPs rather than with exosomes (Figure 13B and D, lower panel). This distinction suggests that GzmB can serve as a marker to differentiate between MVBs and MCGs. It further suggests a specialized exosome packaging and targeting mechanism in CTLs, raising important questions about the potential distinctions between exosomes derived from MVBs and those from MCGs, as well as their respective roles in CTL-mediated immune functions.

IV.2 CD81 is the specific tetraspanin for exosome characterization in murine CTLs

The study of extracellular vesicles (EVs), particularly exosomes, has revealed significant heterogeneity in their structure, origin, and function. This heterogeneity depends not only on the cell type from which they originate but also on the intracellular organelles involved in their formation and release (Willms et al. 2018). Having confirmed that exosomes in murine CD8⁺ CTLs are contained within both MVBs and MCGs, we aimed to investigate the differences between exosomes in these distinct organelles. To effectively characterize exosomes in murine CD8⁺ CTLs, identifying a marker that specifically labels exosome-containing organelles was crucial. CD63 has become the gold standard to distinguish exosomes from other EVs (Kowal et al. 2016; Kowal, Tkach, and Théry 2014), however, in CD8⁺ CTLs, the tetraspanin CD63 poses a challenge, as it also labels SCGs, which do not contain exosomes (Peters et al. 1991; Metzelaar et al. 1991). This overlap in CD63 expression limits its utility to differentiate exosome-containing organelles from SCGs. Therefore, we were haunting for an exosome marker that specifically labels exosome-containing organelles. Structured Illumination Microscopy (SIM) images showed a significant colocalization of CD63 with GzmB (Figure 12B), confirming its association with SCGs. Furthermore, CLEM analysis revealed CD63 on SCG membranes with GzmB as cargo (Figure 13B, upper panel), consistent with previous reports of CD63 marking lytic granules (Peters et al. 1991). In contrast, CD81 exhibited reduced overlap with GzmB (Figure 12B), was not localized on the membrane of SCGs (Figure 13D, upper panel), and specifically labeled MVBs and MCGs (Figure 13D, middle and lower panels), suggesting specificity for exosome-containing organelles. This was corroborated by organelle staining experiments with specific labeling of the membrane of the MVBs, MCGs, and SCGs isolated from murine CTLs. This was achieved by staining the isolated organelles without permeabilizing them, allowing us to detect only the exposed epitopes of the tetraspanins on the membrane of the organelles and not on the exosomes contained within (Figure 14F). Consistent with our SIM and CLEM data on CTLs, the results from the membrane staining

of the isolated organelles further confirmed the non-specificity of CD63 due to its abundance on SCGs membranes (Figure 19B). Furthermore, we show the absence of CD81 from SCG membrane and its abundance on MVB and MCG membrane (Figure 19B). In light of this evidence, we propose CD81 as a prominent marker for characterizing exosomes in murine CD8+ CTLs, allowing us a more accurate characterization of exosome localization and release in these cells.

IV.3 Exosome-containing organelles have distinct fusion characteristics compared to SCGs

Since most, if not all, cell types release exosomes, understanding the dynamics of exosome biogenesis and release is crucial to appreciating their physiological roles in vivo. We investigated whether, in murine CD8⁺ CTLs, MVBs and MCGs both polarize to the immune synapse for fusion. To visualize MVB and MCG fusion events at the immunological synapse in real-time, we performed total internal fluorescence microscopy (TIRFM) on murine CTLs added on anti-CD3 coated coverslips. By using CD63 as a pan-marker for exosome-containing organelles as well as SCGs, we distinguished fusion of MCGs, MVBs, and SCGs, based on distinct fusion dynamics. To temporally characterize fusion events, we monitored fluorescence increases upon MVB/MCG fusion with the plasma membrane. As the exosomal membrane is permeable to protons (Gutknecht 1987; Paula et al. 1996; Raven and Beardall 1981), pHluorin and pHuji molecules facing the exosome (ILV) lumen will be quenched in the MVB/MCG, but become fluorescent upon the fusion of the organelle with the plasma membrane (Figure 14F). SCGs, containing soluble cargo such as GzmB and perforin, displayed fast fusion dynamics (under 2 seconds), marked by rapid fluorescence spikes and fast decay (Figure 15A and B), consistent with previous reports for the plasma membrane deposition of VAMP2 from SCGs (Estl et al. 2020; Verweij et al. 2018). In contrast, MCG and MVB fusion events exhibited longer signal durations of over 2 seconds (Figure 15C and D). Our findings are similar to what has been reported in the literature for the long MVB fusion dynamics in Hela cells and A549 cells (Verweij et al. 2018; Mahmood et al. 2023), confirming the identity of these organelles with long fusion events to MVBs/MCGs. The long signal duration could be likely due to the entrapment of fluorescent exosomes between the cells and the glass coverslip or their immobilization by "sticking" to the PM after MCG/MVB-PM fusion. This hypothesis is supported by the observation that the decay time of CD63 on supported lipid bilayer (SLB) was in general faster than its decay on glass coverslip (Figure 14E and 15F). This difference in signal duration enables us to discriminate between MCG/MVB-PM fusion events and the exocytosis of SCGs that only have CD63 in the limiting membrane (Figure 13B, upper panel).

Interestingly, our TIRFM data revealed that, at the IS, among the long fusion events (decay time over 2 seconds), 69.84% of the events corresponded to MCGs, whereas only 3.96% of the events

corresponded to MVBs, identified by their lack of GzmB (Figure 15H). The high degree of specificity observed in MCG release at the IS suggests the presence of a sophisticated intracellular organization, which may facilitate the direct release of distinct exosomes at the immune synapse for focused interaction with target cells.

IV.4 Role of MUNC13-4 in exosome secretion

MUNC13-4 is a well-known priming factor that facilitates the secretion of lytic granules at the immune synapse, essential for effective CTL function (Dudenhöffer-Pfeifer et al. 2013). Given its importance, we investigated whether MUNC13-4 equally promotes the fusion of both exosome-containing organelles (MVBs and MCGs). Experiments with MUNC13-4 knockout (KO) CTLs revealed that exosome secretion can occur in the absence of MUNC13-4, as exosome isolation from MUNC13-4 KO CTLs was possible (Figure 24). However, the decreased exosome yield in MUNC13-4 KO CTLs (Figure 24C) suggests that MUNC13-4 facilitates the release of a specific subpopulation of exosomes. Notably, as most exosomes secreted at the immune synapse are contained in MCGs (Figure 15H), we used MUNC13-4 KO CTLs co-expressing CD81-SEP and CD63-pHuji to assess whether MCGs fuse at the immune synapse in a MUNC13-4 independent manner. Interestingly, in MUNC13-4 KO CTLs, no secretion was detected at the immune synapse, underscoring the dependence of MCG fusion on MUNC13-4. However, we were able to isolate exosomes from the MUNC13-4 KO CTL culture medium. Therefore, these exosomes must come from MVBs that fuse in a non-polarized manner, independent of MUNC13-4. Additionally, we found that the size of exosomes (Figure 24B) and MVB/MCG (data not shown) were comparable between WT and MUNC13-4 KO CTLs. This suggests that MUNC13-4 does not influence exosome biogenesis or MVB/MCG maturation. This finding contrasts with previous studies where MUNC13-4 was implicated in MVB maturation in cancer cells (Messenger et al. 2018) and CG maturation in human CTLs (Ménager et al. 2007). In murine CTLs, however, MUNC13-4's role appears to be specialized in the priming of MCGs and SCGs and thereby in the secretion of specific exosome subpopulations at the immune synapse rather than influencing overall exosome biogenesis or maturation. Whether the formation of an immune synapse is required for the fusion of MVBs in a non-polarized manner or whether it is dependent on another stimulus is a question that remains to be investigated. Meanwhile, the non-polarized MVBs might facilitate a broader, less targeted release, allowing CD8⁺ CTLs to communicate systemically. Such an arrangement could enable CTLs to optimize exosome-mediated signaling for both local and systemic immune responses, underscoring the specialized, highly coordinated role of exosomes in immune regulation.

IV.5 Role of SNARE proteins

Since we found differences in the priming factor between MVBs and MCGs, we sought to investigate potential differences in the expression of v-SNAREs on these organelles due to the critical role of SNARE machinery in vesicle fusion processes. Numerous SNAREs have been previously implicated in exosome secretion in various tumor cells (Verweij et al. 2018; Gross et al. 2012; Fader et al. 2009a), yet the exact components forming the SNARE complex that mediate MVB-PM fusion and exosome secretion have not been explicitly defined. Using ultracentrifugation, we successfully isolated fusioncompetent SCGs, MCGs, and MVBs from murine CTLs and subsequently conducted a detailed analysis of their markers and morphology through western blotting, electron microscopy, and SIM (Figures 17 and 18). We found that VAMP7, rather than VAMP2, is detected on the membrane of MVBs. Notably, both VAMP2 and VAMP7 were present on the membranes of MCGs, while only VAMP2 was detected on the membranes of SCGs (Figure 18C). This finding aligns with previous literature emphasizing the versatility and specificity of SNARE proteins in exocytosis (Südhof 2013). This differential localization of SNARE proteins suggests distinct mechanisms governing the fusion and secretion of exosomes from these organelles. Advani et al. (1999) and Coco et al. (1999) have highlighted the crucial role of VAMP7 in vesicular trafficking, particularly its association with late endosomes and lysosomes, supporting our observation of VAMP7 on MVBs. Similarly, Fader et al. (2009b) reported that VAMP7, but not VAMP3, is essential for exosome secretion in K562 human chronic myeloid leukemia cells, which aligns with our identification of VAMP7 as the v-SNARE mediating exosome secretion in murine CD8+ CTLs. The detection of VAMP7 on MVBs and MCGs suggests a common biogenesis pathway for both organelles. In contrast, the absence of VAMP2 in MVBs, as well as its fusion in a MUNC13-4 independent manner, shows that MVBs have different SNARE proteins than MCGs and SCGs. This may correlate with the secretion of MVBs in a non-polarized manner, i.e. not at the immune synapse.

IV.6 Heterogeneity of tetraspanins expression on exosome-containing organelles

A highly interesting finding from our study was the low colocalization between the tetraspanins CD63 and CD81 in murine CTLs (Figure 12B). This observation was mirrored in the heterogeneous fusion profiles of CD81-SEP and CD63-pHuji in TIRFM (Figure 16I). Our results show that during MCG fusion events, the decay time of CD81 was consistently faster than that of CD63 (Figure 16). We explained this heterogeneity by the association of CD81 to the membrane of MCGs, while CD63 is predominantly present on the exosomes contained within these MCGs. This hypothesis was confirmed by our membrane staining results of the isolated organelles, which showed that the membranes of both MVBs and MCGs are enriched in CD81, not in CD63 (Figure 19B). Interestingly, staining of the isolated exosomes revealed a decrease in CD63-positive exosomes in MUNC13-4 KO CTLs compared to WT

CTLs (Figure 24D and E). This finding indicates that CD63 is enriched in polarized exosomes contained in MCGs and released at the immune synapse in a MUNC13-4 dependent manner, while CD81 is associated with non-polarized exosomes contained in MVBs, which are secreted in a MUNC13-4 independent manner throughout the cell.

IV.7 Exosomes derived from murine CTLs are divided into two subpopulations based on their surface marker

The low colocalization between the tetraspanins observed in murine CTLs (Figure 12B) led us to investigate potential differences in tetraspanins profiles among individual exosomes. To accurately characterize these differences, we decided to isolate exosomes from the supernatant of murine CTLs. Isolating exosomes from primary cell cultures, particularly from murine CTLs, is significantly more challenging than using immortalized cell lines due to the requirement for sustained, high-quality cell cultures with minimal cell death over several days. Initially, we used cells derived from multiple spleens (up to six mice) to reach approximately $600-800 \times 10^6$ cells by day 5, which yielded sufficient exosome numbers. After optimizing our cell culture methods, we successfully reduced animal use by achieving comparable cell expansion from a single mouse spleen, while maintaining cell viability (Figure 7) and exosome yield. To ensure purity, we used a combination of differential ultracentrifugation and sucrose density gradient ultracentrifugation (Figure 10), isolating exosomes based on size and density (Théry et al. 2006). We validated the identity of isolated exosomes with Western blotting for exosome markers ALIX and TSG101 (Figure 20E and F) and electron microscopy, confirming typical exosome morphology and size (Figure 20A-D). Exosomes were found primarily in fractions with densities of 1.12-1.19 g/ml consistent with the known density of exosomes (Théry et al. 2006), and our mass spectrometry analysis confirmed the purity of the isolated exosomes, with 79 of the detected proteins are included in the Exocarta top 100 list (Figure 21). We then examined whether CD81 and CD63 colocalized on the same exosome or marked distinct exosome subpopulations. Contrary to conventional assumptions of exosome homogeneity, we found that CD63 and CD81 rarely colocalized on individual exosomes, revealing at least two distinct exosome subpopulations in CTLs (Figure 22). But it is important to note that most of the previous research has mainly focused on comparative analysis of classic EV subtypes, i.e. apoptotic bodies, microvesicles, and exosomes (Lunavat et al. 2015; Xu et al. 2015) and of EVs being released from the apical and basolateral surfaces of organoids (Tauro et al. 2013) but not on the exosomes themselves. Here, we reveal for the first time a heterogeneity among exosomes, demonstrating that exosomes released from murine CTLs can express distinct surface markers (Figure 22). An interesting observation from our TEM analysis of isolated exosomes was the existence of two different size populations, with

approximately 53% of exosomes ranging from 30-80 nm and 39% from 80-150 nm (Figure 20A-C). We then examined whether there is a correlation between the size of exosomes and their surface markers. To achieve this, we adapted a 10X expansion method used for expanding proteins (Shaib et al. 2024) and optimized it to expand the isolated exosomes labeled with CD81 and CD63. To the best of our knowledge, we are the first research group to expand exosomes. Our results confirmed that these markers do not localize to the same exosomes and showed that CD63-positive exosomes tended to be larger than CD81-positive exosomes (Figure 23). This suggests that exosome size might correlate with tetraspanin expression, potentially indicating variations in exosome origins, functions, or cargo types. The existence of exosome subtypes in primary CTLs aligns with earlier findings showing diversity within MVBs in terms of ILV size, which is influenced by cargo type and ESCRT-dependence of their biogenesis (Colombo, Raposo, and Théry 2014; Edgar, Eden, and Futter 2014). While our findings add to the growing evidence of exosome heterogeneity, future studies will be needed to determine whether exosome size differences are strictly due to cargo variations or arise from distinct biogenetic pathways. Notably, limitations in the current preparation method, particularly due to the specificity of the anchoring agent (Acryloyl-X) for lysine residues, may have impacted the representation of exosome subtypes in our size distribution analysis (Shaib et al. 2024). Nonetheless, this work provides substantial evidence of distinct CTL exosome subpopulations, advancing our understanding of exosome diversity and suggesting specialized roles for these vesicles in immune function.

IV.8 Polarized exosomes are more cytotoxic than non-polarized exosomes

It is well-established that activated murine CTLs primarily deploy cytotoxic proteins as their main mechanism for inducing target cell death pathways. However, tumors have evolved multiple immune evasion strategies, complicating immune-based interventions. Despite advances in immunotherapy, immune escape remains a significant barrier to effective cancer treatment. Exosomes, recognized for their role in intercellular communication and ability to transfer bioactive molecules, are crucial players in both tumor progression and antitumor immunity. As a key part of the adaptive immune response, CD8+ CTLs target and eliminate tumor cells, though their effectiveness can be weakened by interactions with the tumor microenvironment (TME). Given that EVs have recently gained attention as potential drug delivery systems due to their stability, loading capacity, and targeting abilities, we explored whether exosomes derived from CTLs might serve as an additional cytotoxic mechanism. Indeed, WT CTL-derived exosomes showed substantial cytotoxic activity within 12 hours of incubation and this effect was enhanced after 24 hours (Figure 25). WT-derived exosomes displayed significantly higher cytotoxicity than those from MUNC13-4 KO CTLs, raising the possibility that polarized exosomes contained within MCGs are more potent than those housed in MVBs (Figure 25). This supports our

hypothesis that the exosome sorting process in CTLs is highly specialized. Furthermore, we observed that this killing effect in WT-derived exosomes was mediated by caspase-3 activation, suggesting a Fas/FasL-dependent pathway, as neither perforin nor GzmB was detected within these exosomes in mass spectrometry analysis (Figure 21). Since we show that we isolate highly pure exosomes from the cell culture supernatant (Figures 20 and 21) we can attribute the observed cytotoxic effects to exosomes, rather than other killing entities, such as SMAPs, which have been also reported to exhibit cytotoxic effects on target cells (Chang et al. 2022; Bálint et al. 2020). To further delineate the distinct roles of exosomes and SMAPs, we conducted an additional control experiment by isolating SMAPs directly from MCGs and applying them to P815 target cells. Our results indicate that SMAPs indeed possess cytotoxic activity; however, they exhibit this activity at later points compared to exosomes (supplementary data). Studies have proposed that CTLs employ serial killing and additive cytotoxicity through multiple sublethal hits on target cells (Weigelin et al. 2021; Prager et al. 2019). Based on our findings, CTLs may utilize both exosomes and SMAPs within MCGs to enhance their cytotoxic potential against tumor cells. The reduced cytotoxicity observed in MUNC13-4 KO-derived exosomes highlights the functional differentiation of polarized and non-polarized exosome populations (Figure 25). Future research should further examine the role of non-polarized exosomes to unravel their potential function in immune modulation.

V. Outlook

This dissertation provides a comprehensive characterization of exosomes derived from cytotoxic T lymphocytes (CTLs), elucidating their biogenesis, secretion mechanisms, and functional relevance. Our findings reveal that CTL-derived exosomes are packaged into two distinct organelles, multivesicular bodies (MVBs) and multicore granules (MCGs), highlighting a new layer of complexity in CTL exosome biology. Through advanced imaging techniques such as SIM and CLEM, CD81 was identified as a more reliable marker for CTL-derived exosomes compared to CD63, addressing a longstanding challenge in distinguishing exosome containing organelles from other secretory organelles like single-core granules (SCGs) in CTLs (Figure 26). Functional differences between these exosome-containing organelles were characterized through the polarized secretion of MCG-derived exosomes at the immune synapse, contrasting with the non-polarized release of MVB-derived exosomes. This study uncovered a dependency on MUNC13-4 for MCG fusion, whereas MVB secretion was MUNC13-4-independent. Furthermore, we showed that VAMP7 and not VAMP2 was associated with MVBs. To check whether the differences observed between MVBs and MCGs are translated to a heterogeneity within the exosomes themselves, exosomes were isolated from the supernatant of either WT or MUNC13-4 KO CTLs. Exosome subpopulations were characterized based on size and surface marker expression. Using 10X expansion method we were able to divide exosomes into two subpopulations, the smaller CD81positive exosomes and the larger CD63-positive exosomes, reflecting their molecular and functional diversity (Figure 26). Functional assays demonstrated the critical role of CTL-derived exosomes in inducing caspase-3-mediated apoptosis in target cells. Notably, exosomes from MUNC13-4 knockout CTLs, which lack MCG-mediated secretion, exhibited reduced cytotoxic efficacy, underscoring the importance of regulated exosome release for effective immune responses. This work highlights key aspects of exosome biology while opening several avenues for future research. Investigating the selective sorting mechanisms that direct specific cargo into MVBs or MCGs could provide further insight into the regulation of exosome heterogeneity. RNA sequencing of exosome subpopulations could uncover novel markers and functional roles, advancing the understanding of how CTLs adapt their exosome-mediated responses under various physiological and pathological conditions. The polarized secretion of MCG-derived exosomes at the immune synapse raises intriguing questions about their role in immune synapse formation and signaling. Further research could explore how these exosomes influence synaptic stability, T cell activation, and intercellular communication. Moreover, this study underscores the therapeutic potential of CTL-derived exosomes, particularly in cancer immunotherapy. Future research should focus on fine-tuning CTL-derived exosomes to enhance their specificity and efficacy for targeting immune-resistant tumors. By leveraging their molecular diversity and cytotoxic potential, CTL-derived exosomes could be developed as novel therapeutic agents,

providing new avenues for treating diseases where immune modulation is critical. By addressing fundamental questions in exosome biology and offering new insights into their functional relevance, this dissertation lays the groundwork for advancing both basic and translational research in the fields of immunology and extracellular vesicle bioengineering.

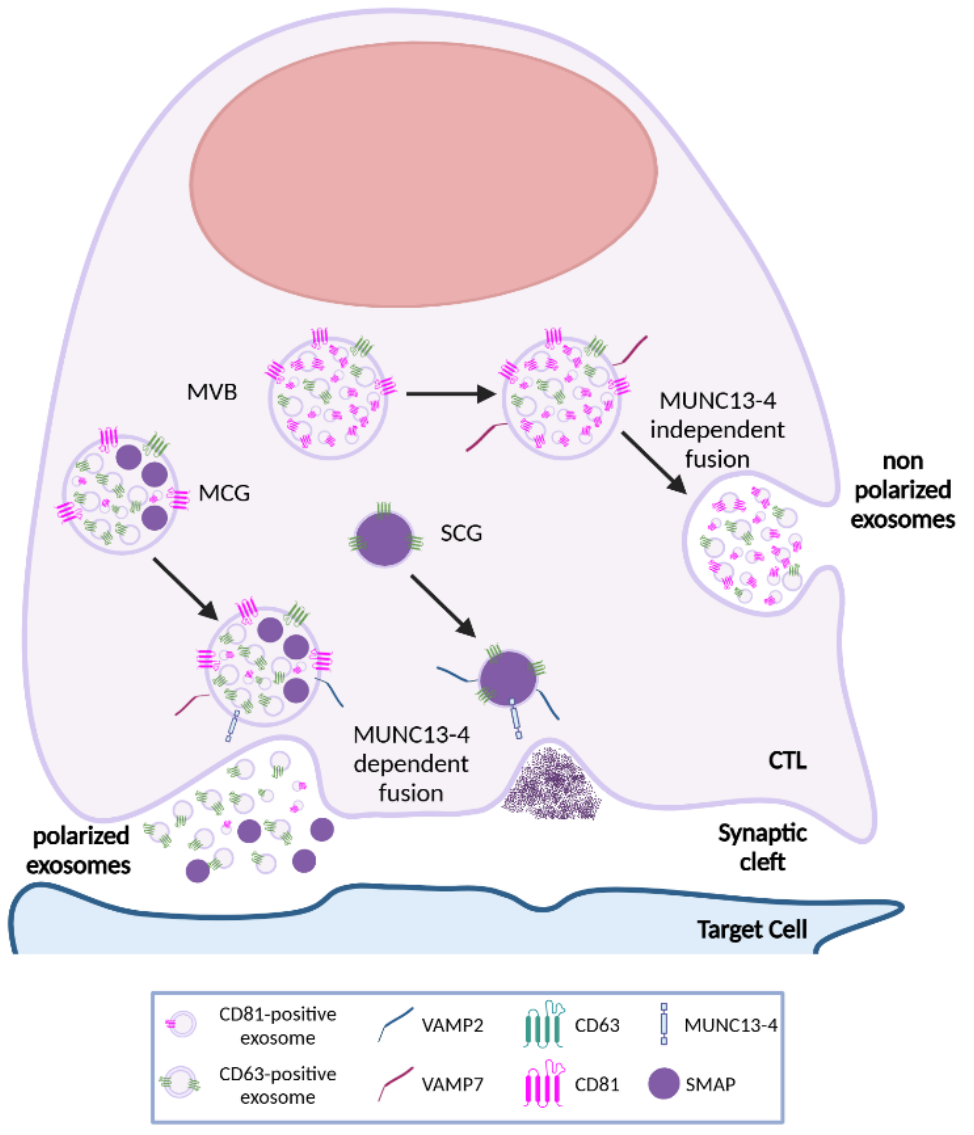
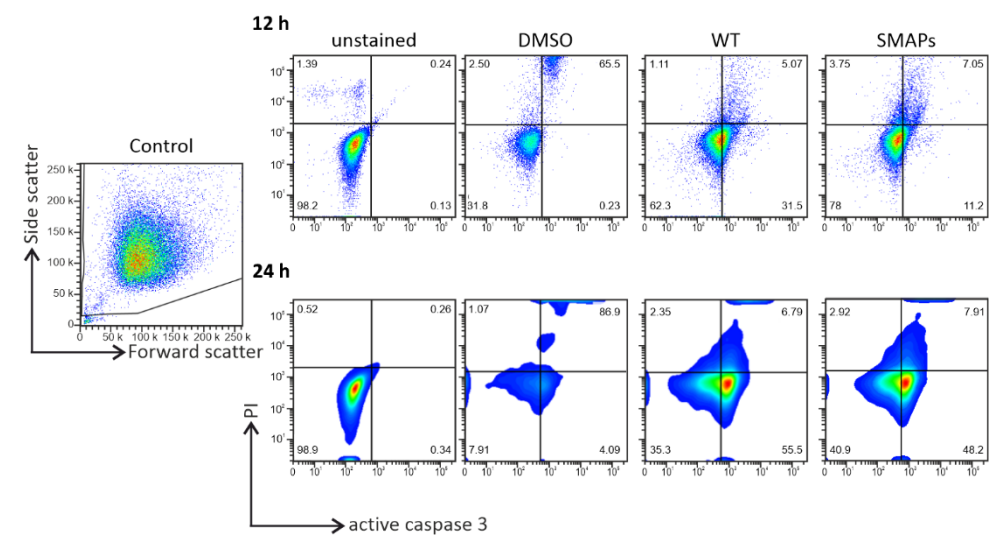


Figure 26: Characterization of exosomes derived from murine CTLs.

A suggested model summarizing our findings. In murine CTLs, exosomes are contained in two distinct organelles, multivesicular bodies (MVBs) and multicore granules (MCGs). Exosomes contained in MCGs are polarized to the immune synapse and are released in a MUNC13-4 dependent manner. However non-polarized exosomes are contained in MVBs and are secreted elsewhere throughout the cells in a MUNC13-4 independent manner. Interestingly, polarized exosomes show superior killing to their non-polarized counterparts. Furthermore, we show that CD81 is a more specific marker to exosome containing organelles, due to its abundance on the membrane of MCGs and MVBs and its absence from the membrane of SCGs. We also showed that exosomes could be further divided based on their tetraspanin surface expression into CD81-positive exosomes, and CD63-positive exosomes. Where CD63 seems to be abundant on the polarized exosomes and CD81 on the non-polarized ones.

VI. Index



Supplementary Figure 1: Comparison of exosomes and SMAPs cytotoxicity.

Representative flow cytometry analysis of the cytotoxic assay performed on P815 target cells incubated with either 10 μ g/ml exosomes or supramolecular attack particles (SMAPs) derived from WT CTLs. Cells were gated based on the forward and side scatter. DMSO was used as a positive control. The percentage of active caspase 3 and PI+ cells was evaluated after 12 (**upper panel**) and 24 h (**lower panel**) of incubation with CTL-exosomes. N = 1.

VII. References

- Admyre, C., S. M. Johansson, S. Paulie, and S. Gabrielsson. 2006. 'Direct exosome stimulation of peripheral human T cells detected by ELISPOT', *Eur J Immunol*, 36: 1772-81.
- Advani, R. J., B. Yang, R. Prekeris, K. C. Lee, J. Klumperman, and R. H. Scheller. 1999. 'VAMP-7 mediates vesicular transport from endosomes to lysosomes', *J Cell Biol*, 146: 765-76.
- Afonina, I. S., S. P. Cullen, and S. J. Martin. 2010. 'Cytotoxic and non-cytotoxic roles of the CTL/NK protease granzyme B', *Immunol Rev*, 235: 105-16.
- Alawar, N., C. Schirra, M. Hohmann, and U. Becherer. 2024. 'A solution for highly efficient electroporation of primary cytotoxic T lymphocytes', *BMC Biotechnol*, 24: 16.
- Alimonti, J. B., L. Shi, P. K. Baijal, and A. H. Greenberg. 2001. 'Granzyme B induces BID-mediated cytochrome c release and mitochondrial permeability transition', *J Biol Chem*, 276: 6974-82.
- Alonso, R., C. Mazzeo, M. C. Rodriguez, M. Marsh, A. Fraile-Ramos, V. Calvo, A. Avila-Flores, I. Merida, and M. Izquierdo. 2011. 'Diacylglycerol kinase α regulates the formation and polarisation of mature multivesicular bodies involved in the secretion of Fas ligand-containing exosomes in T lymphocytes', *Cell Death Differ*, 18: 1161-73.
- Ambrose, A. R., K. S. Hazime, J. D. Worboys, O. Niembro-Vivanco, and D. M. Davis. 2020. 'Synaptic secretion from human natural killer cells is diverse and includes supramolecular attack particles', *Proc Natl Acad Sci U S A*, 117: 23717-20.
- Andrade, Felipe, Sophie Roy, Donald Nicholson, Nancy Thornberry, Antony Rosen, and Livia Casciola-Rosen. 1998. 'Granzyme B Directly and Efficiently Cleaves Several Downstream Caspase Substrates: Implications for CTL-Induced Apoptosis', *Immunity*, 8: 451-60.
- Aubert, Alexandre, Karen Jung, Sho Hiroyasu, Julian Pardo, and David J. Granville. 2024. 'Granzyme serine proteases in inflammation and rheumatic diseases', *Nature Reviews Rheumatology*, 20: 361-76.
- Babbitt, Bruce P., Paul M. Allen, Gary Matsueda, Edgar Haber, and Emil R. Unanue. 1985. 'Binding of immunogenic peptides to la histocompatibility molecules', *Nature*, 317: 359-61.
- Bálint, Š, S. Müller, R. Fischer, B. M. Kessler, M. Harkiolaki, S. Valitutti, and M. L. Dustin. 2020. 'Supramolecular attack particles are autonomous killing entities released from cytotoxic T cells', *Science*, 368: 897-901.
- Becherer, U., and J. Rettig. 2006. 'Vesicle pools, docking, priming, and release', *Cell Tissue Res*, 326: 393-407.
- Bissinger, Rosi, Polina Petkova-Kirova, Olga Mykhailova, Per-Arne Oldenborg, Elena Novikova, David A. Donkor, Thomas Dietz, Abdulla Al Mamun Bhuyan, William P. Sheffield, Marijke Grau, Ferruh Artunc, Lars Kaestner, Jason P. Acker, and Syed M. Qadri. 2020. 'Thrombospondin-1/CD47 signaling modulates transmembrane cation conductance, survival, and deformability of human red blood cells', *Cell Communication and Signaling*, 18: 155.
- Block, M. R., B. S. Glick, C. A. Wilcox, F. T. Wieland, and J. E. Rothman. 1988. 'Purification of an Nethylmaleimide-sensitive protein catalyzing vesicular transport', *Proc Natl Acad Sci U S A*, 85: 7852-6.
- Blott, Emma J., and Gillian M. Griffiths. 2002. 'Secretory lysosomes', *Nature Reviews Molecular Cell Biology*, 3: 122-31.
- Bonilla, F. A., and H. C. Oettgen. 2010. 'Adaptive immunity', J Allergy Clin Immunol, 125: S33-40.
- Brennan, A. J., J. Chia, K. A. Browne, A. Ciccone, S. Ellis, J. A. Lopez, O. Susanto, S. Verschoor, H. Yagita, J. C. Whisstock, J. A. Trapani, and I. Voskoboinik. 2011. 'Protection from endogenous perforin: glycans and the C terminus regulate exocytic trafficking in cytotoxic lymphocytes', *Immunity*, 34: 879-92.
- Broz, P., P. Pelegrín, and F. Shao. 2020. 'The gasdermins, a protein family executing cell death and inflammation', *Nat Rev Immunol*, 20: 143-57.
- Bryceson, Y. T., E. Rudd, C. Zheng, J. Edner, D. Ma, S. M. Wood, A. G. Bechensteen, J. J. Boelens, T. Celkan, R. A. Farah, K. Hultenby, J. Winiarski, P. A. Roche, M. Nordenskjöld, J. I. Henter, E. O. Long, and H. G. Ljunggren. 2007. 'Defective cytotoxic lymphocyte degranulation in syntaxin-

- 11 deficient familial hemophagocytic lymphohistiocytosis 4 (FHL4) patients', *Blood*, 110: 1906-15
- Burkhardt, J. K., S. Hester, C. K. Lapham, and Y. Argon. 1990. 'The lytic granules of natural killer cells are dual-function organelles combining secretory and pre-lysosomal compartments', *J Cell Biol*, 111: 2327-40.
- Capitani, N., and C. T. Baldari. 2022. 'The Immunological Synapse: An Emerging Target for Immune Evasion by Bacterial Pathogens', *Front Immunol*, 13: 943344.
- Catalán, E., P. Jaime-Sánchez, N. Aguiló, M. M. Simon, C. J. Froelich, and J. Pardo. 2015. 'Mouse cytotoxic T cell-derived granzyme B activates the mitochondrial cell death pathway in a Bimdependent fashion', *J Biol Chem*, 290: 6868-77.
- Chairoungdua, A., D. L. Smith, P. Pochard, M. Hull, and M. J. Caplan. 2010. 'Exosome release of β-catenin: a novel mechanism that antagonizes Wnt signaling', *J Cell Biol*, 190: 1079-91.
- Chang, H. F., C. Schirra, M. Ninov, U. Hahn, K. Ravichandran, E. Krause, U. Becherer, Š Bálint, M. Harkiolaki, H. Urlaub, S. Valitutti, C. T. Baldari, M. L. Dustin, R. Jahn, and J. Rettig. 2022. 'Identification of distinct cytotoxic granules as the origin of supramolecular attack particles in T lymphocytes', *Nat Commun*, 13: 1029.
- Chen, F., P. W. Tillberg, and E. S. Boyden. 2015. 'Optical imaging. Expansion microscopy', *Science*, 347: 543-8.
- Chia, Clemente, and Jason McClure. 2020. 'Protective mechanisms of the body', *Anaesthesia & Intensive Care Medicine*, 21: 154-56.
- Chitirala, P., K. Ravichandran, D. Galgano, M. Sleiman, E. Krause, Y. T. Bryceson, and J. Rettig. 2019. 'Cytotoxic Granule Exocytosis From Human Cytotoxic T Lymphocytes Is Mediated by VAMP7', Front Immunol, 10: 1855.
- Chitirala, P., K. Ravichandran, C. Schirra, H. F. Chang, E. Krause, U. Kazmaier, M. A. Lauterbach, and J. Rettig. 2020. 'Role of V-ATPase a3-Subunit in Mouse CTL Function', *J Immunol*, 204: 2818-28.
- Choi, D. S., D. K. Kim, Y. K. Kim, and Y. S. Gho. 2013. 'Proteomics, transcriptomics and lipidomics of exosomes and ectosomes', *Proteomics*, 13: 1554-71.
- Chowdhury, D., and J. Lieberman. 2008. 'Death by a thousand cuts: granzyme pathways of programmed cell death', *Annu Rev Immunol*, 26: 389-420.
- Coco, S., G. Raposo, S. Martinez, J. J. Fontaine, S. Takamori, A. Zahraoui, R. Jahn, M. Matteoli, D. Louvard, and T. Galli. 1999. 'Subcellular localization of tetanus neurotoxin-insensitive vesicle-associated membrane protein (VAMP)/VAMP7 in neuronal cells: evidence for a novel membrane compartment', *J Neurosci*, 19: 9803-12.
- Colombo, M., G. Raposo, and C. Théry. 2014. 'Biogenesis, secretion, and intercellular interactions of exosomes and other extracellular vesicles', *Annu Rev Cell Dev Biol*, 30: 255-89.
- D'Angelo, M. E., P. I. Bird, C. Peters, T. Reinheckel, J. A. Trapani, and V. R. Sutton. 2010. 'Cathepsin H is an additional convertase of pro-granzyme B', *J Biol Chem*, 285: 20514-9.
- Darmon, A. J., D. W. Nicholson, and R. C. Bleackley. 1995. 'Activation of the apoptotic protease CPP32 by cytotoxic T-cell-derived granzyme B', *Nature*, 377: 446-8.
- Deng, F., and J. Miller. 2019. 'A review on protein markers of exosome from different bio-resources and the antibodies used for characterization', *J Histotechnol*, 42: 226-39.
- Dudenhöffer-Pfeifer, Monika, Claudia Schirra, Varsha Pattu, Mahantappa Halimani, Monika Maier-Peuschel, Misty R. Marshall, Ulf Matti, Ute Becherer, Jan Dirks, Martin Jung, Peter Lipp, Markus Hoth, Martina Sester, Elmar Krause, and Jens Rettig. 2013. 'Different Munc13 Isoforms Function as Priming Factors in Lytic Granule Release from Murine Cytotoxic T Lymphocytes', *Traffic*, 14: 798-809.
- Dustin, M. L. 2014. 'The immunological synapse', Cancer Immunol Res, 2: 1023-33.
- Dustin, M. L., S. K. Bromley, Z. Kan, D. A. Peterson, and E. R. Unanue. 1997. 'Antigen receptor engagement delivers a stop signal to migrating T lymphocytes', *Proc Natl Acad Sci U S A*, 94: 3909-13.

- Dustin, M. L., A. K. Chakraborty, and A. S. Shaw. 2010. 'Understanding the structure and function of the immunological synapse', *Cold Spring Harb Perspect Biol*, 2: a002311.
- Edgar, J. R., E. R. Eden, and C. E. Futter. 2014. 'Hrs- and CD63-dependent competing mechanisms make different sized endosomal intraluminal vesicles', *Traffic*, 15: 197-211.
- Enomoto, Yutaka, Peng Li, Lisa M. Jenkins, Dimitrios Anastasakis, Gaelyn C. Lyons, Markus Hafner, and Warren J. Leonard. 2022. 'Cytokine-enhanced cytolytic activity of exosomes from NK Cells', *Cancer Gene Therapy*, 29: 734-49.
- Estl, M., P. Blatt, X. Li, U. Becherer, H. F. Chang, J. Rettig, and V. Pattu. 2020. 'Various Stages of Immune Synapse Formation Are Differently Dependent on the Strength of the TCR Stimulus', Int J Mol Sci, 21.
- Fader, C. M., D. G. Sánchez, M. B. Mestre, and M. I. Colombo. 2009a. 'TI-VAMP/VAMP7 and VAMP3/cellubrevin: two v-SNARE proteins involved in specific steps of the autophagy/multivesicular body pathways', *Biochim Biophys Acta*, 1793: 1901-16.
- Fader, Claudio Marcelo, Diego Germán Sánchez, María Belén Mestre, and María Isabel Colombo. 2009b. 'TI-VAMP/VAMP7 and VAMP3/cellubrevin: two v-SNARE proteins involved in specific steps of the autophagy/multivesicular body pathways', *Biochimica et Biophysica Acta (BBA) Molecular Cell Research*, 1793: 1901-16.
- Favaro, R. R., K. Phillips, R. Delaunay-Danguy, K. Ujčič, and U. R. Markert. 2022. 'Emerging Concepts in Innate Lymphoid Cells, Memory, and Reproduction', *Front Immunol*, 13: 824263.
- Feldmann, J., I. Callebaut, G. Raposo, S. Certain, D. Bacq, C. Dumont, N. Lambert, M. Ouachée-Chardin, G. Chedeville, H. Tamary, V. Minard-Colin, E. Vilmer, S. Blanche, F. Le Deist, A. Fischer, and G. de Saint Basile. 2003. 'Munc13-4 is essential for cytolytic granules fusion and is mutated in a form of familial hemophagocytic lymphohistiocytosis (FHL3)', *Cell*, 115: 461-73.
- Fitzner, D., M. Schnaars, D. van Rossum, G. Krishnamoorthy, P. Dibaj, M. Bakhti, T. Regen, U. K. Hanisch, and M. Simons. 2011. 'Selective transfer of exosomes from oligodendrocytes to microglia by macropinocytosis', *J Cell Sci*, 124: 447-58.
- Fraser, S. A., R. Karimi, M. Michalak, and D. Hudig. 2000. 'Perforin lytic activity is controlled by calreticulin', *J Immunol*, 164: 4150-5.
- Fukuda, M. 1991. 'Lysosomal membrane glycoproteins. Structure, biosynthesis, and intracellular trafficking', *Journal of Biological Chemistry*, 266: 21327-30.
- ———. 2013. 'Rab27 effectors, pleiotropic regulators in secretory pathways', *Traffic*, 14: 949-63.
- Ghossoub, Rania, Frédérique Lembo, Aude Rubio, Carole Baron Gaillard, Jérôme Bouchet, Nicolas Vitale, Josef Slavík, Miroslav Machala, and Pascale Zimmermann. 2014. 'Syntenin-ALIX exosome biogenesis and budding into multivesicular bodies are controlled by ARF6 and PLD2', *Nature Communications*, 5: 3477.
- Griffiths, G. M., and S. Isaaz. 1993. 'Granzymes A and B are targeted to the lytic granules of lymphocytes by the mannose-6-phosphate receptor', *J Cell Biol*, 120: 885-96.
- Gross, J. C., V. Chaudhary, K. Bartscherer, and M. Boutros. 2012. 'Active Wnt proteins are secreted on exosomes', *Nat Cell Biol*, 14: 1036-45.
- Gulati, Poonam. 2009. 'Janeway's Immunobiology, 7th Edition by Kenneth Murphy, Paul Travers, and Mark Walport', *Biochemistry and Molecular Biology Education*, 37: 134-34.
- Gunzer, Matthias, Angelika Schäfer, Stefan Borgmann, Stephan Grabbe, Kurt S. Zänker, Eva-Bettina Bröcker, Eckhart Kämpgen, and Peter Friedl. 2000. 'Antigen Presentation in Extracellular Matrix: Interactions of T Cells with Dendritic Cells Are Dynamic, Short Lived, and Sequential', *Immunity*, 13: 323-32.
- Gutknecht, J. 1987. 'Proton/hydroxide conductance and permeability through phospholipid bilayer membranes', *Proc Natl Acad Sci U S A*, 84: 6443-6.
- Haddad, E. K., X. Wu, J. A. Hammer, 3rd, and P. A. Henkart. 2001. 'Defective granule exocytosis in Rab27a-deficient lymphocytes from Ashen mice', *J Cell Biol*, 152: 835-42.

- Halimani, Mahantappa, Varsha Pattu, Misty R. Marshall, Hsin Fang Chang, Ulf Matti, Martin Jung, Ute Becherer, Elmar Krause, Markus Hoth, Eva C. Schwarz, and Jens Rettig. 2014. 'Syntaxin11 serves as a t-SNARE for the fusion of lytic granules in human cytotoxic T lymphocytes', European Journal of Immunology, 44: 573-84.
- Han, J., L. A. Goldstein, B. R. Gastman, C. J. Froelich, X. M. Yin, and H. Rabinowich. 2004. 'Degradation of Mcl-1 by granzyme B: implications for Bim-mediated mitochondrial apoptotic events', *J Biol Chem*, 279: 22020-9.
- Hanson, P. I., and A. Cashikar. 2012. 'Multivesicular body morphogenesis', *Annu Rev Cell Dev Biol*, 28: 337-62.
- Harding, C., and P. Stahl. 1983. 'Transferrin recycling in reticulocytes: pH and iron are important determinants of ligand binding and processing', *Biochem Biophys Res Commun*, 113: 650-8.
- He, Jin-Shu, and Hanne L. Ostergaard. 2007. 'CTLs Contain and Use Intracellular Stores of FasL Distinct from Cytolytic Granules1', *The Journal of Immunology*, 179: 2339-48.
- Holt, O., E. Kanno, G. Bossi, S. Booth, T. Daniele, A. Santoro, M. Arico, C. Saegusa, M. Fukuda, and G. M. Griffiths. 2008. 'Slp1 and Slp2-a localize to the plasma membrane of CTL and contribute to secretion from the immunological synapse', *Traffic*, 9: 446-57.
- Hromada, Carina, Severin Mühleder, Johannes Grillari, Heinz Redl, and Wolfgang Holnthoner. 2017. 'Endothelial Extracellular Vesicles—Promises and Challenges', *Frontiers in Physiology*, 8.
- Huang, X., S. Sun, X. J. Wang, F. H. Fan, Q. Zhou, S. Lu, Y. Cao, Q. W. Wang, M. Q. Dong, J. Yao, and S. F. Sui. 2019. 'Mechanistic insights into the SNARE complex disassembly', *Science Advances*, 5.
- Hurley, J. H. 2008. 'ESCRT complexes and the biogenesis of multivesicular bodies', *Curr Opin Cell Biol*, 20: 4-11.
- Hurwitz, S. N., M. M. Conlon, M. A. Rider, N. C. Brownstein, and D. G. Meckes, Jr. 2016. 'Nanoparticle analysis sheds budding insights into genetic drivers of extracellular vesicle biogenesis', *J Extracell Vesicles*, 5: 31295.
- lezzi, G., K. Karjalainen, and A. Lanzavecchia. 1998. 'The duration of antigenic stimulation determines the fate of naive and effector T cells', *Immunity*, 8: 89-95.
- Irvine, D. J., M. A. Purbhoo, M. Krogsgaard, and M. M. Davis. 2002. 'Direct observation of ligand recognition by T cells', *Nature*, 419: 845-9.
- Jenne, D. E., and J. Tschopp. 1988. 'Granzymes, a family of serine proteases released from granules of cytolytic T lymphocytes upon T cell receptor stimulation', *Immunol Rev*, 103: 53-71.
- Kalluri, R., and V. S. LeBleu. 2020. 'The biology, function, and biomedical applications of exosomes', *Science*, 367.
- Kim, H. Y., H. K. Min, H. W. Song, A. Yoo, S. Lee, K. P. Kim, J. O. Park, Y. H. Choi, and E. Choi. 2022. 'Delivery of human natural killer cell-derived exosomes for liver cancer therapy: an in vivo study in subcutaneous and orthotopic animal models', *Drug Deliv*, 29: 2897-911.
- Koh, Choong-Hyun, Suyoung Lee, Minkyeong Kwak, Byung-Seok Kim, and Yeonseok Chung. 2023. 'CD8 T-cell subsets: heterogeneity, functions, and therapeutic potential', *Experimental & Molecular Medicine*, 55: 2287-99.
- Konjar, S., V. R. Sutton, S. Hoves, U. Repnik, H. Yagita, T. Reinheckel, C. Peters, V. Turk, B. Turk, J. A. Trapani, and N. Kopitar-Jerala. 2010. 'Human and mouse perforin are processed in part through cleavage by the lysosomal cysteine proteinase cathepsin L', *Immunology*, 131: 257-67
- Kowal, Joanna, Guillaume Arras, Marina Colombo, Mabel Jouve, Jakob Paul Morath, Bjarke Primdal-Bengtson, Florent Dingli, Damarys Loew, Mercedes Tkach, and Clotilde Théry. 2016.

 'Proteomic comparison defines novel markers to characterize heterogeneous populations of extracellular vesicle subtypes', *Proceedings of the National Academy of Sciences*, 113: E968-E77.
- Kowal, Joanna, Mercedes Tkach, and Clotilde Théry. 2014. 'Biogenesis and secretion of exosomes', *Current Opinion in Cell Biology*, 29: 116-25.

- Kuhn, J. R., and M. Poenie. 2002. 'Dynamic polarization of the microtubule cytoskeleton during CTL-mediated killing', *Immunity*, 16: 111-21.
- Kupfer, A., and S. J. Singer. 1989. 'The specific interaction of helper T cells and antigen-presenting B cells. IV. Membrane and cytoskeletal reorganizations in the bound T cell as a function of antigen dose', *Journal of Experimental Medicine*, 170: 1697-713.
- Kurowska, M., N. Goudin, N. T. Nehme, M. Court, J. Garin, A. Fischer, G. de Saint Basile, and G. Ménasché. 2012. 'Terminal transport of lytic granules to the immune synapse is mediated by the kinesin-1/Slp3/Rab27a complex', *Blood*, 119: 3879-89.
- Lieberman, Judy. 2003. 'The ABCs of granule-mediated cytotoxicity: new weapons in the arsenal', *Nature Reviews Immunology*, 3: 361-70.
- Liu, D., J. A. Martina, X. S. Wu, J. A. Hammer, 3rd, and E. O. Long. 2011. 'Two modes of lytic granule fusion during degranulation by natural killer cells', *Immunol Cell Biol*, 89: 728-38.
- Liu, Q., D. M. Rojas-Canales, S. J. Divito, W. J. Shufesky, D. B. Stolz, G. Erdos, M. L. Sullivan, G. A. Gibson, S. C. Watkins, A. T. Larregina, and A. E. Morelli. 2016. 'Donor dendritic cell-derived exosomes promote allograft-targeting immune response', *J Clin Invest*, 126: 2805-20.
- Liu, Y., Y. Fang, X. Chen, Z. Wang, X. Liang, T. Zhang, M. Liu, N. Zhou, J. Lv, K. Tang, J. Xie, Y. Gao, F. Cheng, Y. Zhou, Z. Zhang, Y. Hu, X. Zhang, Q. Gao, Y. Zhang, and B. Huang. 2020. 'Gasdermin E-mediated target cell pyroptosis by CAR T cells triggers cytokine release syndrome', *Sci Immunol*, 5.
- Lunavat, T. R., L. Cheng, D. K. Kim, J. Bhadury, S. C. Jang, C. Lässer, R. A. Sharples, M. D. López, J. Nilsson, Y. S. Gho, A. F. Hill, and J. Lötvall. 2015. 'Small RNA deep sequencing discriminates subsets of extracellular vesicles released by melanoma cells--Evidence of unique microRNA cargos', *RNA Biol*, 12: 810-23.
- Maas, S. L. N., X. O. Breakefield, and A. M. Weaver. 2017. 'Extracellular Vesicles: Unique Intercellular Delivery Vehicles', *Trends Cell Biol*, 27: 172-88.
- Mahmood, Anarkali, Zdeněk Otruba, Alan W. Weisgerber, Max D. Palay, Melodie T. Nguyen, Broderick L. Bills, and Michelle K. Knowles. 2023. 'Exosome secretion kinetics are controlled by temperature', *Biophysical Journal*, 122: 1301-14.
- Mathieu, M., N. Névo, M. Jouve, J. I. Valenzuela, M. Maurin, F. J. Verweij, R. Palmulli, D. Lankar, F. Dingli, D. Loew, E. Rubinstein, G. Boncompain, F. Perez, and C. Théry. 2021. 'Specificities of exosome versus small ectosome secretion revealed by live intracellular tracking of CD63 and CD9', *Nat Commun*, 12: 4389.
- Matti, U., V. Pattu, M. Halimani, C. Schirra, E. Krause, Y. Liu, L. Weins, H. F. Chang, R. Guzman, J. Olausson, M. Freichel, F. Schmitz, M. Pasche, U. Becherer, D. Bruns, and J. Rettig. 2013. 'Synaptobrevin2 is the v-SNARE required for cytotoxic T-lymphocyte lytic granule fusion', *Nat Commun*, 4: 1439.
- McMahon, H. T., and E. Boucrot. 2015. 'Membrane curvature at a glance', J Cell Sci, 128: 1065-70.
- Meade, J. L., E. A. de Wynter, P. Brett, S. M. Sharif, C. G. Woods, A. F. Markham, and G. P. Cook. 2006. 'A family with Papillon-Lefevre syndrome reveals a requirement for cathepsin C in granzyme B activation and NK cell cytolytic activity', *Blood*, 107: 3665-8.
- Mempel, T. R., S. E. Henrickson, and U. H. Von Andrian. 2004. 'T-cell priming by dendritic cells in lymph nodes occurs in three distinct phases', *Nature*, 427: 154-9.
- Ménager, Mickaël M., Gaël Ménasché, Maryse Romao, Perrine Knapnougel, Chen-Hsuan Ho, Mériem Garfa, Graça Raposo, Jérôme Feldmann, Alain Fischer, and Geneviève de Saint Basile. 2007. 'Secretory cytotoxic granule maturation and exocytosis require the effector protein hMunc13-4', *Nature Immunology*, 8: 257-67.
- Ménasché, G., E. Pastural, J. Feldmann, S. Certain, F. Ersoy, S. Dupuis, N. Wulffraat, D. Bianchi, A. Fischer, F. Le Deist, and G. de Saint Basile. 2000. 'Mutations in RAB27A cause Griscelli syndrome associated with haemophagocytic syndrome', *Nat Genet*, 25: 173-6.

- Messenger, Scott W., Sang Su Woo, Zhongze Sun, and Thomas F.J. Martin. 2018. 'A Ca2+-stimulated exosome release pathway in cancer cells is regulated by Munc13-4', *Journal of Cell Biology*, 217: 2877-90.
- Metkar, S. S., B. Wang, M. L. Ebbs, J. H. Kim, Y. J. Lee, S. M. Raja, and C. J. Froelich. 2003. 'Granzyme B activates procaspase-3 which signals a mitochondrial amplification loop for maximal apoptosis', *J Cell Biol*, 160: 875-85.
- Metzelaar, M. J., P. L. Wijngaard, P. J. Peters, J. J. Sixma, H. K. Nieuwenhuis, and H. C. Clevers. 1991. 'CD63 antigen. A novel lysosomal membrane glycoprotein, cloned by a screening procedure for intracellular antigens in eukaryotic cells', *J Biol Chem*, 266: 3239-45.
- Meunier, Frédéric A., and Zhitao Hu. 2023. 'Functional Roles of UNC-13/Munc13 and UNC-18/Munc18 in Neurotransmission.' in Zhao-Wen Wang (ed.), *Molecular Mechanisms of Neurotransmitter Release* (Springer International Publishing: Cham).
- Mittelbrunn, M., and F. Sánchez-Madrid. 2012. 'Intercellular communication: diverse structures for exchange of genetic information', *Nat Rev Mol Cell Biol*, 13: 328-35.
- Monks, C. R., B. A. Freiberg, H. Kupfer, N. Sciaky, and A. Kupfer. 1998. 'Three-dimensional segregation of supramolecular activation clusters in T cells', *Nature*, 395: 82-6.
- Morelli, A. E., W. Bracamonte-Baran, and W. J. Burlingham. 2017. 'Donor-derived exosomes: the trick behind the semidirect pathway of allorecognition', *Curr Opin Organ Transplant*, 22: 46-54.
- Morse, M. A., J. Garst, T. Osada, S. Khan, A. Hobeika, T. M. Clay, N. Valente, R. Shreeniwas, M. A. Sutton, A. Delcayre, D. H. Hsu, J. B. Le Pecq, and H. K. Lyerly. 2005. 'A phase I study of dexosome immunotherapy in patients with advanced non-small cell lung cancer', *J Transl Med*, 3: 9.
- Müller, M. L., S. C. Chiang, M. Meeths, B. Tesi, M. Entesarian, D. Nilsson, S. M. Wood, M. Nordenskjöld, J. I. Henter, A. Naqvi, and Y. T. Bryceson. 2014. 'An N-Terminal Missense Mutation in STX11 Causative of FHL4 Abrogates Syntaxin-11 Binding to Munc18-2', Front Immunol, 4: 515.
- Nazarenko, I., S. Rana, A. Baumann, J. McAlear, A. Hellwig, M. Trendelenburg, G. Lochnit, K. T. Preissner, and M. Zöller. 2010. 'Cell surface tetraspanin Tspan8 contributes to molecular pathways of exosome-induced endothelial cell activation', *Cancer Res*, 70: 1668-78.
- Neeft, M., M. Wieffer, A. S. de Jong, G. Negroiu, C. H. G. Metz, A. van Loon, J. Griffith, J. Krijgsveld, N. Wulffraat, H. Koch, A. J. R. Heckt, N. Brose, M. Kleijmeer, and P. van der Sluijs. 2005. 'Munc13-4 is an effector of Rab27a and controls secretion of lysosomes in hematopoietic cells', *Molecular Biology of the Cell*, 16: 731-41.
- Nesvizhskii, A. I., A. Keller, E. Kolker, and R. Aebersold. 2003. 'A statistical model for identifying proteins by tandem mass spectrometry', *Anal Chem*, 75: 4646-58.
- Neviani, P., P. M. Wise, M. Murtadha, C. W. Liu, C. H. Wu, A. Y. Jong, R. C. Seeger, and M. Fabbri. 2019. 'Natural Killer-Derived Exosomal miR-186 Inhibits Neuroblastoma Growth and Immune Escape Mechanisms', *Cancer Res*, 79: 1151-64.
- Pan, B. T., and R. M. Johnstone. 1983. 'Fate of the transferrin receptor during maturation of sheep reticulocytes in vitro: selective externalization of the receptor', *Cell*, 33: 967-78.
- Pardo, J., R. Wallich, P. Martin, C. Urban, A. Rongvaux, R. A. Flavell, A. Müllbacher, C. Borner, and M. M. Simon. 2008. 'Granzyme B-induced cell death exerted by ex vivo CTL: discriminating requirements for cell death and some of its signs', *Cell Death Differ*, 15: 567-79.
- Paula, S., A. G. Volkov, A. N. Van Hoek, T. H. Haines, and D. W. Deamer. 1996. 'Permeation of protons, potassium ions, and small polar molecules through phospholipid bilayers as a function of membrane thickness', *Biophys J*, 70: 339-48.
- Peters, P. J., J. Borst, V. Oorschot, M. Fukuda, O. Krahenbuhl, J. Tschopp, J. W. Slot, and H. J. Geuze. 1991. 'Cytotoxic Lymphocyte-T Granules Are Secretory Lysosomes, Containing Both Perforin and Granzymes', *Journal of Experimental Medicine*, 173: 1099-109.

- Peters, P. J., H. J. Geuze, H. A. Van der Donk, J. W. Slot, J. M. Griffith, N. J. Stam, H. C. Clevers, and J. Borst. 1989. 'Molecules relevant for T cell-target cell interaction are present in cytolytic granules of human T lymphocytes', *Eur J Immunol*, 19: 1469-75.
- Prager, I., C. Liesche, H. van Ooijen, D. Urlaub, Q. Verron, N. Sandström, F. Fasbender, M. Claus, R. Eils, J. Beaudouin, B. Önfelt, and C. Watzl. 2019. 'NK cells switch from granzyme B to death receptor-mediated cytotoxicity during serial killing', *Journal of Experimental Medicine*, 216: 2113-27.
- Prekeris, R., J. Klumperman, and R. H. Scheller. 2000. 'Syntaxin 11 is an atypical SNARE abundant in the immune system', *Eur J Cell Biol*, 79: 771-80.
- Prunevieille, Aurore, Mohamed H. Babiker-Mohamed, Colleen Aslami, Bruno Gonzalez-Nolasco, Nuala Mooney, and Gilles Benichou. 2021. 'T cell antigenicity and immunogenicity of allogeneic exosomes', *American Journal of Transplantation*, 21: 2583-89.
- Raposo, G., H. W. Nijman, W. Stoorvogel, R. Liejendekker, C. V. Harding, C. J. Melief, and H. J. Geuze. 1996. 'B lymphocytes secrete antigen-presenting vesicles', *Journal of Experimental Medicine*, 183: 1161-72.
- Raposo, G., and W. Stoorvogel. 2013. 'Extracellular vesicles: exosomes, microvesicles, and friends', *J Cell Biol*, 200: 373-83.
- Raskov, Hans, Adile Orhan, Jan Pravsgaard Christensen, and Ismail Gögenur. 2021. 'Cytotoxic CD8+ T cells in cancer and cancer immunotherapy', *British Journal of Cancer*, 124: 359-67.
- Raven, John A., and John Beardall. 1981. 'The intrinsic permeability of biological membranes to H+: Significance for the efficiency of low rates of energy transformation', *FEMS Microbiology Letters*, 10: 1-5.
- Ravichandran, Veerasamy, Ashish Chawla, and Paul A. Roche. 1996. 'Identification of a Novel Syntaxin- and Synaptobrevin/VAMP-binding Protein, SNAP-23, Expressed in Non-neuronal Tissues*', *Journal of Biological Chemistry*, 271: 13300-03.
- Rettig, Jens, and David R. Stevens. 2017. 'Synaptic Transmission in the Immune System', *e-Neuroforum*, 23: A167-A74.
- Riera Romo, M., D. Pérez-Martínez, and C. Castillo Ferrer. 2016. 'Innate immunity in vertebrates: an overview', *Immunology*, 148: 125-39.
- Sancho, D., M. Vicente-Manzanares, M. Mittelbrunn, M. C. Montoya, M. Gordón-Alonso, J. M. Serrador, and F. Sánchez-Madrid. 2002. 'Regulation of microtubule-organizing center orientation and actomyosin cytoskeleton rearrangement during immune interactions', *Immunol Rev*, 189: 84-97.
- Scaffidi, C., S. Fulda, A. Srinivasan, C. Friesen, F. Li, K. J. Tomaselli, K. M. Debatin, P. H. Krammer, and M. E. Peter. 1998. 'Two CD95 (APO-1/Fas) signaling pathways', *Embo j*, 17: 1675-87.
- Schirra, C., N. Alawar, U. Becherer, and H. F. Chang. 2023. 'Separation of Single Core and Multicore Lytic Granules by Subcellular Fractionation and Immunoisolation', *Methods Mol Biol*, 2654: 159-67.
- Shaib, A. H., A. A. Chouaib, R. Chowdhury, J. Altendorf, D. Mihaylov, C. Zhang, D. Krah, V. Imani, R. K. W. Spencer, S. V. Georgiev, N. Mougios, M. Monga, S. Reshetniak, T. Mimoso, H. Chen, P. Fatehbasharzad, D. Crzan, K. A. Saal, M. M. Alawieh, N. Alawar, J. Eilts, J. Kang, A. Soleimani, M. Müller, C. Pape, L. Alvarez, C. Trenkwalder, B. Mollenhauer, T. F. Outeiro, S. Köster, J. Preobraschenski, U. Becherer, T. Moser, E. S. Boyden, A. R. Aricescu, M. Sauer, F. Opazo, and S. O. Rizzoli. 2024. 'One-step nanoscale expansion microscopy reveals individual protein shapes', *Nat Biotechnol*.
- Shen, Y., M. Rosendale, R. E. Campbell, and D. Perrais. 2014. 'pHuji, a pH-sensitive red fluorescent protein for imaging of exo- and endocytosis', *J Cell Biol*, 207: 419-32.
- Smyth, L. A., K. Ratnasothy, J. Y. Tsang, D. Boardman, A. Warley, R. Lechler, and G. Lombardi. 2013. 'CD73 expression on extracellular vesicles derived from CD4+ CD25+ Foxp3+ T cells contributes to their regulatory function', *Eur J Immunol*, 43: 2430-40.

- Smyth, M. J., M. J. McGuire, and K. Y. Thia. 1995. 'Expression of recombinant human granzyme B. A processing and activation role for dipeptidyl peptidase I', *J Immunol*, 154: 6299-305.
- Söllner, T., M. K. Bennett, S. W. Whiteheart, R. H. Scheller, and J. E. Rothman. 1993. 'A protein assembly-disassembly pathway in vitro that may correspond to sequential steps of synaptic vesicle docking, activation, and fusion', *Cell*, 75: 409-18.
- Söllner, T., S. W. Whiteheart, M. Brunner, H. Erdjument-Bromage, S. Geromanos, P. Tempst, and J. E. Rothman. 1993. 'SNAP receptors implicated in vesicle targeting and fusion', *Nature*, 362: 318-24.
- Stinchcombe, Jane C., Endre Majorovits, Giovanna Bossi, Stephen Fuller, and Gillian M. Griffiths. 2006. 'Centrosome polarization delivers secretory granules to the immunological synapse', *Nature*, 443: 462-65.
- Stuffers, S., C. Sem Wegner, H. Stenmark, and A. Brech. 2009. 'Multivesicular endosome biogenesis in the absence of ESCRTs', *Traffic*, 10: 925-37.
- Südhof, T. C. 2013. 'A molecular machine for neurotransmitter release: synaptotagmin and beyond', *Nat Med*, 19: 1227-31.
- Sutton, R. B., D. Fasshauer, R. Jahn, and A. T. Brunger. 1998. 'Crystal structure of a SNARE complex involved in synaptic exocytosis at 2.4 A resolution', *Nature*, 395: 347-53.
- Takeuchi, O., and S. Akira. 2010. 'Pattern recognition receptors and inflammation', Cell, 140: 805-20.
- Tamai, K., N. Tanaka, T. Nakano, E. Kakazu, Y. Kondo, J. Inoue, M. Shiina, K. Fukushima, T. Hoshino, K. Sano, Y. Ueno, T. Shimosegawa, and K. Sugamura. 2010. 'Exosome secretion of dendritic cells is regulated by Hrs, an ESCRT-0 protein', *Biochem Biophys Res Commun*, 399: 384-90.
- Tang, Bor Luen, Delphine Y. H. Low, and Wanjin Hong. 1998. 'Syntaxin 11: A Member of the Syntaxin Family without a Carboxyl Terminal Transmembrane Domain', *Biochemical and Biophysical Research Communications*, 245: 627-32.
- Tauro, B. J., D. W. Greening, R. A. Mathias, S. Mathivanan, H. Ji, and R. J. Simpson. 2013. 'Two distinct populations of exosomes are released from LIM1863 colon carcinoma cell-derived organoids', *Mol Cell Proteomics*, 12: 587-98.
- Théry, C., S. Amigorena, G. Raposo, and A. Clayton. 2006. 'Isolation and characterization of exosomes from cell culture supernatants and biological fluids', *Curr Protoc Cell Biol*, Chapter 3: Unit 3.22.
- Théry, C., M. Boussac, P. Véron, P. Ricciardi-Castagnoli, G. Raposo, J. Garin, and S. Amigorena. 2001. 'Proteomic analysis of dendritic cell-derived exosomes: a secreted subcellular compartment distinct from apoptotic vesicles', *J Immunol*, 166: 7309-18.
- Thomas, Dori A., Luca Scorrano, Girish V. Putcha, Stanley J. Korsmeyer, and Timothy J. Ley. 2001. 'Granzyme B can cause mitochondrial depolarization and cell death in the absence of BID, BAX, and BAK', *Proceedings of the National Academy of Sciences*, 98: 14985-90.
- Torralba, Daniel, Francesc Baixauli, Carolina Villarroya-Beltri, Irene Fernández-Delgado, Ana Latorre-Pellicer, Rebeca Acín-Pérez, Noa B. Martín-Cófreces, Ángel Luis Jaso-Tamame, Salvador Iborra, Inmaculada Jorge, Gloria González-Aseguinolaza, Johan Garaude, Miguel Vicente-Manzanares, José Antonio Enríquez, María Mittelbrunn, and Francisco Sánchez-Madrid. 2018. 'Priming of dendritic cells by DNA-containing extracellular vesicles from activated T cells through antigen-driven contacts', *Nature Communications*, 9: 2658.
- Trajkovic, K., C. Hsu, S. Chiantia, L. Rajendran, D. Wenzel, F. Wieland, P. Schwille, B. Brügger, and M. Simons. 2008. 'Ceramide triggers budding of exosome vesicles into multivesicular endosomes', *Science*, 319: 1244-7.
- Trams, E. G., C. J. Lauter, N. Salem, Jr., and U. Heine. 1981. 'Exfoliation of membrane ecto-enzymes in the form of micro-vesicles', *Biochim Biophys Acta*, 645: 63-70.
- Tricarico, C., J. Clancy, and C. D'Souza-Schorey. 2017. 'Biology and biogenesis of shed microvesicles', *Small GTPases*, 8: 220-32.
- Turvey, Stuart E., and David H. Broide. 2010. 'Innate immunity', *Journal of Allergy and Clinical Immunology*, 125: S24-S32.

- Uellner, Ruth, Marketa J. Zvelebil, Jean Hopkins, Jane Jones, Lindsay K. MacDougall, B. Paul Morgan, Eckhard Podack, Michael D. Waterfield, and Gillian M. Griffiths. 1997. 'Perforin is activated by a proteolytic cleavage during biosynthesis which reveals a phospholipid-binding C2 domain', *The EMBO Journal*, 16: 7287-96-96.
- Valadi, H., K. Ekström, A. Bossios, M. Sjöstrand, J. J. Lee, and J. O. Lötvall. 2007. 'Exosome-mediated transfer of mRNAs and microRNAs is a novel mechanism of genetic exchange between cells', *Nat Cell Biol*, 9: 654-9.
- van Niel, Guillaume, Gisela D'Angelo, and Graça Raposo. 2018. 'Shedding light on the cell biology of extracellular vesicles', *Nature Reviews Molecular Cell Biology*, 19: 213-28.
- Verweij, F. J., M. P. Bebelman, C. R. Jimenez, J. J. Garcia-Vallejo, H. Janssen, J. Neefjes, J. C. Knol, R. de Goeij-de Haas, S. R. Piersma, S. R. Baglio, M. Verhage, J. M. Middeldorp, A. Zomer, J. van Rheenen, M. G. Coppolino, I. Hurbain, G. Raposo, M. J. Smit, R. F. G. Toonen, G. van Niel, and D. M. Pegtel. 2018. 'Quantifying exosome secretion from single cells reveals a modulatory role for GPCR signaling', *J Cell Biol*, 217: 1129-42.
- Voskoboinik, I., M. J. Smyth, and J. A. Trapani. 2006. 'Perforin-mediated target-cell death and immune homeostasis', *Nat Rev Immunol*, 6: 940-52.
- Voskoboinik, Ilia, James C. Whisstock, and Joseph A. Trapani. 2015. 'Perforin and granzymes: function, dysfunction and human pathology', *Nature Reviews Immunology*, 15: 388-400.
- Walczak, H., and M. R. Sprick. 2001. 'Biochemistry and function of the DISC', *Trends Biochem Sci*, 26: 452-3.
- Wang, S., Y. Li, J. H. Gong, S. Ye, X. F. Yang, R. G. Zhang, and C. Ma. 2019. 'Munc18 and Munc13 serve as a functional template to orchestrate neuronal SNARE complex assembly', *Nature Communications*, 10.
- Wang, Xianping, Jihong Gong, Le Zhu, Shen Wang, Xiaoyu Yang, Yuanyuan Xu, Xiaofei Yang, and Cong Ma. 2020. 'Munc13 activates the Munc18-1/syntaxin-1 complex and enables Munc18-1 to prime SNARE assembly', *The EMBO Journal*, 39: e103631.
- Weidman, P. J., P. Melançon, M. R. Block, and J. E. Rothman. 1989. 'Binding of an N-ethylmaleimide-sensitive fusion protein to Golgi membranes requires both a soluble protein(s) and an integral membrane receptor', *J Cell Biol*, 108: 1589-96.
- Weigelin, B., A. T. den Boer, E. Wagena, K. Broen, H. Dolstra, R. J. de Boer, C. G. Figdor, J. Textor, and P. Friedl. 2021. 'Cytotoxic T cells are able to efficiently eliminate cancer cells by additive cytotoxicity', *Nat Commun*, 12: 5217.
- Welsh, J. A., D. C. I. Goberdhan, L. O'Driscoll, E. I. Buzas, C. Blenkiron, B. Bussolati, H. Cai, D. Di Vizio, T. A. P. Driedonks, U. Erdbrügger, J. M. Falcon-Perez, Q. L. Fu, A. F. Hill, M. Lenassi, S. K. Lim, M. G. Mahoney, S. Mohanty, A. Möller, R. Nieuwland, T. Ochiya, S. Sahoo, A. C. Torrecilhas, L. Zheng, A. Zijlstra, S. Abuelreich, R. Bagabas, P. Bergese, E. M. Bridges, M. Brucale, D. Burger, R. P. Carney, E. Cocucci, R. Crescitelli, E. Hanser, A. L. Harris, N. J. Haughey, A. Hendrix, A. R. Ivanov, T. Jovanovic-Talisman, N. A. Kruh-Garcia, V. Ku'ulei-Lyn Faustino, D. Kyburz, C. Lässer, K. M. Lennon, J. Lötvall, A. L. Maddox, E. S. Martens-Uzunova, R. R. Mizenko, L. A. Newman, A. Ridolfi, E. Rohde, T. Rojalin, A. Rowland, A. Saftics, U. S. Sandau, J. A. Saugstad, F. Shekari, S. Swift, D. Ter-Ovanesyan, J. P. Tosar, Z. Useckaite, F. Valle, Z. Varga, E. van der Pol, M. J. C. van Herwijnen, M. H. M. Wauben, A. M. Wehman, S. Williams, A. Zendrini, A. J. Zimmerman, C. Théry, and K. W. Witwer. 2024. 'Minimal information for studies of extracellular vesicles (MISEV2023): From basic to advanced approaches', J Extracell Vesicles, 13: e12404.
- Willms, Eduard, Carlos Cabañas, Imre Mäger, Matthew J. A. Wood, and Pieter Vader. 2018. 'Extracellular Vesicle Heterogeneity: Subpopulations, Isolation Techniques, and Diverse Functions in Cancer Progression', *Frontiers in Immunology*, 9.
- Xu, Rong, David W. Greening, Alin Rai, Hong Ji, and Richard J. Simpson. 2015. 'Highly-purified exosomes and shed microvesicles isolated from the human colon cancer cell line LIM1863 by

- sequential centrifugal ultrafiltration are biochemically and functionally distinct', *Methods*, 87: 11-25.
- Yang, Chao-Yu, Chia- I. Lien, Yi-Chun Tseng, Yi-Fan Tu, Arkadiusz W. Kulczyk, Yen-Chen Lu, Yin-Ting Wang, Tsung-Wei Su, Li-Chung Hsu, Yu-Chih Lo, and Su-Chang Lin. 2024. 'Deciphering DED assembly mechanisms in FADD-procaspase-8-cFLIP complexes regulating apoptosis', *Nature Communications*, 15: 3791.
- Yannelli, J R, J A Sullivan, G L Mandell, and V H Engelhard. 1986. 'Reorientation and fusion of cytotoxic T lymphocyte granules after interaction with target cells as determined by high resolution cinemicrography', *The Journal of Immunology*, 136: 377-82.
- Zhang, Zhibin, Ying Zhang, Shiyu Xia, Qing Kong, Shunying Li, Xing Liu, Caroline Junqueira, Karla F. Meza-Sosa, Temy Mo Yin Mok, James Ansara, Satyaki Sengupta, Yandan Yao, Hao Wu, and Judy Lieberman. 2020. 'Gasdermin E suppresses tumour growth by activating anti-tumour immunity', *Nature*, 579: 415-20.
- Zhu, H., S. Guariglia, R. Y. Yu, W. Li, D. Brancho, H. Peinado, D. Lyden, J. Salzer, C. Bennett, and C. W. Chow. 2013. 'Mutation of SIMPLE in Charcot-Marie-Tooth 1C alters production of exosomes', *Molecular Biology of the Cell*, 24: 1619-37, s1-3.
- Zitvogel, L., A. Regnault, A. Lozier, J. Wolfers, C. Flament, D. Tenza, P. Ricciardi-Castagnoli, G. Raposo, and S. Amigorena. 1998. 'Eradication of established murine tumors using a novel cell-free vaccine: dendritic cell-derived exosomes', *Nat Med*, 4: 594-600.

VIII. Publications and Conferences

- Alawar N, Schirra C, Hohmann M, Becherer U. A solution for highly efficient electroporation of primary cytotoxic T lymphocytes. BMC Biotechnology 2024 Mar 26;24(1):16. doi: 10.1186/s12896-024-00839-4.
- Shaib AH, Chouaib AA, Chowdhury R, Altendorf J, Mihaylov D, Zhang C, Krah D, Imani V, Spencer RKW, Georgiev SV, Mougios N, Monga M, Reshetniak S, Mimoso T, Chen H, Fatehbasharzad P, Crzan D, Saal KA, Alawieh MM, <u>Alawar N</u>, Eilts J, Kang J, Soleimani A, Müller M, Pape C, Alvarez L, Trenkwalder C, Mollenhauer B, Outeiro TF, Köster S, Preobraschenski J, Becherer U, Moser T, Boyden ES, Aricescu AR, Sauer M, Opazo F, Rizzoli SO. One-step nanoscale expansion microscopy reveals individual protein shapes. Nat Biotechnol. 2024 Oct 9:10.1038/s41587-024-02431-9. doi: 10.1038/s41587-024-02431-9.
- Schirra C, <u>Alawar N</u>, Becherer U, Chang HF. Separation of Single Core and Multicore Lytic Granules by Subcellular Fractionation and Immunoisolation. Methods Mol Biol. 2023;2654:159-167. doi: 10.1007/978-1-0716-3135-5 11.PMID: 37106182
- 4. Ravichandran K, Schirra C, Urbansky K, Tu SM, <u>Alawar N</u>, Mannebach S, Krause E, Stevens D, Lancaster RD, Flockerzi V, Rettig J, Chang HF, Becherer U. Required minimal protein domain of flower for synaptobrevin 2 endocytosis in cytotoxic T lymphocytes. Accepted in Cellular and Molecular Life Sciences.
- 5. Cassioli C, Capitani N, Staton C, Schirra C, Finetti F, Onnis A, <u>Alawar N</u>, Tu SM, Lopresti L, Tatangelo V, Tangredi C, Valvo S, Chang HF, Miccoli A, Compeer EB, Nicholls J, Blazar B, Marotta G, Wood MJA, Trentin L, Patrussi L, Dustin ML, Becherer U, Baldari CT. Thrombospondins 1 and 4 undergo coordinated transport to multicore cytotoxic granules to regulate SMAP biogenesis and function in CTL-mediated cytotoxicity. (Under revision in PNAS).
- 6. Chouaib A, Chang HF, Khamis OM, <u>Alawar N</u>, Echeverry S, Demeersseman L, Elizarova S, Daniel JA, Valitutti S, Barg S, Pape C, Shaib AH, Becherer U. Highly adaptable deep-learning platform for automated detection and analysis of vesicle exocytosis. (Under revision in Nature Communication).
- 7. <u>Alawar N</u>, Schirra C, Fecher-Trost C, Flockerzi V, Becherer U. The journey of murine CTL-derived exosomes from the cells via the organelles to the target. (Manuscript under preparation).
- 8. <u>Alawar N</u>, Schirra C, Becherer U. The role of VAMP2 and VAMP7 in the fusion of exosome-containing organelles in murine CTLs. (Manuscript under preparation).

9. Li X, <u>Alawar N</u>, Tu SM, Lin HC, Wirkner ML, Hohmann M, Schirra C, Becherer U, Krause E, Chang HF. Interferon-gamma secretion in cytotoxic T lymphocytes (Manuscript under preparation).

Poster: <u>Alawar N</u>, Schirra C, Becherer U, Rettig J. (2024) The journey of murine CTL-derived exosomes from the cells via the organelles to the cells. ATTACK consortium, Siena, Italy.

Poster: <u>Alawar N</u>, Schirra C, Bechere U, Rettig J. (2023) Isolation and characterization of exosomes derived from murine CTLs. Cell physics, Saarbrucken, Germany.

Talk: <u>Alawar N</u>. A magical solution for a highly efficient electroporation for primary immune cells. (2023) ATTACK consortium, Freinsheim, Germany.

Poster: <u>Alawar N</u>, Schirra C, Becherer U, Rettig J. (2022) Exosomes derived from murine CTLs can be divided into different subpopulations based on their surface markers. ATTACK consortium, Oxford, UK.

Mini proposal: <u>Alawar N</u>. Isolation and characterization of exosomes derived from murine CTLs. (2021) SFB894 mini proposal winner.

IX. Acknowledgment

Writing this acknowledgment is an emotional moment, as many incredible people have supported me throughout this journey, making my story come to life. As my thesis title reflects a journey, so does my gratitude, which starts with **Prof. Dr. Jens Rettig**. Thank you, Jens, for giving me the opportunity to pursue my PhD in your lab. Sadly, you left our lab too soon, and I was only able to work under your supervision for a year. I often wished you could return to see what I've accomplished with these exosomes.

The next stop on this journey is **Dr. Ute Becherer**. Thank you, Ute, for stepping in after Jens. You have been a mentor on so many levels, and I'm grateful for our discussions and small talks. Your trust and encouragement gave me the freedom to pursue my ideas and shaped my scientific personality.

A special thanks goes to **Dr. Claudia Schirra**. You made my journey nicer with all the motivation you provided. Your door was always open to hear my ideas, and you helped me translate my thoughts into concrete plans and protocols within minutes. I deeply appreciate the tips and tricks you taught me and your efforts to show me how things work in both the lab and life. I might not always find a Claudia, but I will always have 'The Claudia'.

This journey wouldn't have been possible without the help of our amazing technicians—Margarete Klose, Nicole Rothgerber, Anja Bergsträßer, Katrin Sandmeier, and Silke Bruns-Engers. I came to this lab as a 21-year-old girl, far from her family and country, embarking on a completely new experience. You all welcomed me as family, and you made my lab experience so much better.

I extend my heartfelt thanks to **Dr. Elmar Krause**. I thoroughly enjoyed our debates about exosomes and appreciated our insightful discussions. Of course, I must thank our senior postdoc, **Dr. David Stevens**. Dave, thank you for always making time to discuss, even after your retirement. I am also grateful to **Dr. Hsin-Fang Chang** for our nice talks and shared desserts, and to **Dr. Meltem Hohmann** for sharing the good and bad days with me. Thank you for being so friendly and supportive.

This experience wouldn't have been amazing without the friendships I formed with my former colleagues **Dr. Praneeth Chitirala**, **Dr. Angelina Staudt**, **Dr. Keerthana Ravichandran**, and **Dr. Marwa Sleiman**, as well as my current colleagues **Ching-Hsin (Neko) Lin**, **Marie-Louise Wirkner**, **Aicha Bouzouina**, **Lucie Simonin**, **Ruth Rasuli**, and **Jacqueline Wolf**. I was fortunate to overlap with two generations of colleagues and to get to know all of you.

Special thanks go to **Abed Chouaib** for his invaluable help with writing macros, scripts, and plugins and for the 5 o'clock snack breaks.

A huge thank you goes to **Prof. Dr. Dieter Bruns**. In Jens's absence, you were always available for discussions, and your advice and support meant so much to me. I would also like to thank **Dr. Mazen Makke** for being an incredible friend and advisor. Even though you moved 500 km away, you were always just a call away whenever I needed to talk.

Thank you, Jun.- Prof. Dr. Marcel Lauterbach, for our engaging discussions and for always including me in your lab activities. I am equally grateful to the Lauterbach gang—Yasser Medlej, Ahmad Lotfinia, and Tobias Danker—for all the wonderful memories. You made me feel like a part of two groups instead of just one.

I would also like to thank **Bernadette Schwarz** for her help and support, especially with the paperwork.

To my friends at CIPMM from various groups, thank you for the good times we shared. To my friends outside the lab—**Nour Jaber**, **Rayan Dakroub**, **Ali Atieh**, and **Hadi Sraieddine**—thank you for your love and unwavering support.

A special thank you goes to **Samer Alasmi**. Samer, you made my days brighter and motivated me to work harder to achieve my dreams. Your support means the world to me.

This journey has not been easy. During these years, I lost several beloved family members and could not say my goodbyes. I hope I've made you proud. To my brother **Alaa**, losing you has been the hardest thing in my life. I promised you I would keep going, and I hope I've honoured that promise.

To my parents, **Nadeem** and **Maha**, thank you for your patience and sacrifices. I hope I've made you proud, and I hope one day you'll see the importance of this research. To my younger siblings, **Nye** and **Alaa**, I wish I've set a good example for you. I hope that when you see this work, you feel proud and understand why I had to travel far away.

Finally, to my eldest brother **Khaled**, none of this would have been possible without you. Thank you for believing in me, for supporting my education, and for being my rock. I am truly the luckiest sister in the world to have you.

Curriculum Vitae

Aus datenschutzrechtlichen Gründen wird der Lebenslauf in der elektronischen Fassung der Dissertation nicht veröffentlicht.